



# LUND UNIVERSITY

## **MRI-Only Radiotherapy of Prostate Cancer. Development and Evaluation of Methods to Assess Fiducial Marker Detection, Geometric Accuracy and Dosimetric Integrity.**

Jamtheim Gustafsson, Christian

2019

*Document Version:*

Publisher's PDF, also known as Version of record

[Link to publication](#)

*Citation for published version (APA):*

Jamtheim Gustafsson, C. (2019). *MRI-Only Radiotherapy of Prostate Cancer. Development and Evaluation of Methods to Assess Fiducial Marker Detection, Geometric Accuracy and Dosimetric Integrity*. [Doctoral Thesis (compilation), Department of Translational Medicine]. Lund University: Faculty of Medicine.

*Total number of authors:*

1

### **General rights**

Unless other specific re-use rights are stated the following general rights apply:

Copyright and moral rights for the publications made accessible in the public portal are retained by the authors and/or other copyright owners and it is a condition of accessing publications that users recognise and abide by the legal requirements associated with these rights.

- Users may download and print one copy of any publication from the public portal for the purpose of private study or research.
- You may not further distribute the material or use it for any profit-making activity or commercial gain
- You may freely distribute the URL identifying the publication in the public portal

Read more about Creative commons licenses: <https://creativecommons.org/licenses/>

### **Take down policy**

If you believe that this document breaches copyright please contact us providing details, and we will remove access to the work immediately and investigate your claim.

LUND UNIVERSITY

PO Box 117  
221 00 Lund  
+46 46-222 00 00

# MRI-Only Radiotherapy of Prostate Cancer

Development and Evaluation of Methods to Assess Fiducial Marker Detection, Geometric Accuracy and Dosimetric Integrity

CHRISTIAN JAMTHEIM GUSTAFSSON

MEDICAL RADIATION PHYSICS | FACULTY OF MEDICINE | LUND UNIVERSITY



# MRI-Only Radiotherapy of Prostate Cancer

Development and Evaluation of Methods to Assess  
Fiducial Marker Detection, Geometric Accuracy and  
Dosimetric Integrity

Christian Jamtheim Gustafsson



**LUND**  
UNIVERSITY

DOCTORAL DISSERTATION


by due permission of the Faculty of Medicine, Lund University, Sweden.  
To be defended in the Lecture Hall, 3<sup>rd</sup> floor of the Radiotherapy Building at Skåne  
University Hospital, Klinikgatan 5, Lund, on Friday, May 31<sup>st</sup>, 2019 at 09.00.

*Faculty opponent*

Associate Professor Cornelis van den Berg, Department of Radiotherapy, University  
Medical Center Utrecht, Utrecht, the Netherlands

|   |  |                           |
|---|--|---------------------------|
| Organization<br>LUND UNIVERSITY<br>Medical Radiation Physics<br>Department of Translational Medicine<br>Faculty of Medicine, Lund University<br>Author(s)<br>Christian Jamtheim Gustafsson  | Document name<br>DOCTORAL DISSERTATION |                           |
|   | Date of issue<br>2019-05-31            |                           |
|   | Sponsoring organization                |                           |
| Title and subtitle<br>MRI-Only Radiotherapy of Prostate Cancer: Development and Evaluation of Methods to Assess Fiducial Marker Detection, Geometric Accuracy and Dosimetric Integrity  |  |                           |
| Abstract<br><p>A workflow based solely on MRI images for prostate radiotherapy planning eliminates the need for CT imaging and CT/MRI image registration. The density map required for the calculation of absorbed dose is generated from MRI data providing a synthetic CT image. This is referred to as an MRI-only workflow.</p> <p>Geometric distortion can occur in MRI images, and will thus be propagated in the synthetic CT images. This can lead to errors in target delineation and an undesirable dosimetric impact. Gold fiducial markers are implanted in the prostate for treatment target positioning. These markers have excellent visibility in CT images, but are difficult to detect using MRI. These issues must be investigated and resolved before an MRI-only workflow can be clinically implemented.</p> <p>A method has been developed to investigate the dosimetric implications and impact on structure delineation from MRI-system-related geometric distortion. The method was applied to an MRI acquisition sequence, designed specifically for synthetic CT generation. No clinically relevant dose difference (<math>\leq 0.02\%</math>) or structural deformation (<math>&lt; 0.5</math> mm) was found when a 3D distortion correction was applied and a high acquisition bandwidth was used.</p> <p>Synthetic CT images of the male pelvis were generated using dedicated MRI acquisition sequences and commercially available software. The dosimetric accuracy and clinical robustness of the software were evaluated in a multicenter/multivendor setting. Synthetic CT generation was found to be possible with a variety of MRI systems, and radiotherapy treatment techniques, with minimal overall mean dose differences (<math>&lt; 0.3\%</math>) compared to CT.</p> <p>To resolve the problem of poor visibility and detection of gold fiducial markers in MRI images, a multi-echo gradient echo acquisition sequence was developed, optimized and validated. Gold fiducial markers could then be reliably identified, with 99% detection accuracy. An MRI-independent method was developed and evaluated to confirm the location of the identified gold fiducial markers. All the fiducial markers were confirmed to have been correctly identified. The method takes advantage of an X-ray image acquired during insertion of the gold fiducial markers, prior to radiotherapy. No additional imaging was therefore required for this independent quality control step.</p> <p>The methods developed and presented in this thesis can facilitate a clinically feasible and safe implementation of an MRI-only prostate radiotherapy workflow.</p> |  |                           |
| Key words   |  |                           |
| Classification system and/or index terms (if any)   |  |                           |
| Supplementary bibliographical information   |  | Language<br>English       |
| ISSN and key title<br>1652-8220, Lund University, Faculty of Medicine Doctoral Dissertation<br>Series 2019:46   |  | ISBN<br>978-91-7619-775-2 |
| Recipient's notes   | Number of pages<br>88                  | Price                     |
|   | Security classification                |                           |

I, the undersigned, being the copyright owner of the abstract of the above-mentioned dissertation, hereby grant to all reference sources permission to publish and disseminate the abstract of the above-mentioned dissertation.

Signature  Date 2019-04-09

# MRI-Only Radiotherapy of Prostate Cancer

Development and Evaluation of Methods to Assess  
Fiducial Marker Detection, Geometric Accuracy and  
Dosimetric Integrity

Christian Jamtheim Gustafsson



**LUND**  
UNIVERSITY

Front cover by Christian Jamtheim Gustafsson: Large field of view T2-weighted MRI image of the male pelvis, intended for synthetic CT generation. Image style transfer has been applied to the image from Pablo Picasso's painting "Spanish Love", using an artificial system based on deep neural network architecture. <https://gist.github.com/standarderror>, LA Gatys et al. "A Neural Algorithm of Artistic Style" arXiv (2015).

Back cover by Marina Jamtheim: Photo of the author in the early spring of 2019.

Copyright pp 1-88 Christian Jamtheim Gustafsson

Paper I © IOP Publishing

Paper II © The authors (open access)

Paper III © The authors (open access)

Paper IV © The authors (open access)

Medical Radiation Physics  
Department of Translational Medicine  
Faculty of Medicine, Lund University

ISBN 978-91-7619-775-2

ISSN 1652-8220

Lund University, Faculty of Medicine Doctoral Dissertation Series 2019:46

Printed in Sweden by Media-Tryck, Lund University  
Lund 2019



MADE IN SWEDEN 

Media-Tryck is an environmentally certified and ISO 14001 certified provider of printed material. Read more about our environmental work at [www.mediatryck.lu.se](http://www.mediatryck.lu.se)

*To Theo and Marina – My fixed stars*

*”... en partner är mer än så, det är en livslång vän.”*

*Mamma (2009)*

*”... när det är så här stökigt, gör en LTG – Låt Tiden Gå.”*

*Pappa (2005)*

*”... jag KAN gå på månen, det gäller bara att hålla balansen.”*

*Christian, cirka 4 år (1988)*

# Contents

|   |           |
|---|-----------|
| Abstract .....  | 9         |
| Populärvetenskaplig sammanfattning.....                           | 11        |
| Original papers .....   | 13        |
| The author's contributions .....                                  | 14        |
| Related publications .....  | 15        |
| Preliminary reports .....   | 16        |
| Abbreviations .....   | 17        |
| <b>1. Introduction.....</b>                                       | <b>19</b> |
| 1.1. Image registration .....                                     | 20        |
| 1.2. MRI-only .....   | 21        |
| 1.3. Patient positioning .....                                    | 21        |
| 1.4. Opportunities in MRI-only workflows .....                    | 23        |
| 1.5. Challenges in MRI-only workflows.....                        | 23        |
| <b>2. Aims.....</b>   | <b>27</b> |
| <b>3. MRI in Radiotherapy.....</b>                                | <b>29</b> |
| 3.1. MRI simulation in radiotherapy .....                         | 29        |
| 3.1.1. Patient positioning.....                                   | 30        |
| 3.1.2. Imaging .....  | 30        |
| 3.2. MRI image distortion .....                                   | 31        |
| 3.3. System-induced geometric distortion .....                    | 32        |
| 3.3.1. Non-linear MRI gradients.....                              | 33        |
| 3.3.2. Magnetic field inhomogeneities .....                       | 34        |
| 3.3.3. Reduction of system-induced distortion.....                | 34        |
| 3.3.4. Measurement of system-induced distortion.....              | 35        |
| 3.4. Patient- and object-induced geometric distortion.....        | 37        |
| 3.4.1. Magnetic susceptibility .....                              | 38        |
| 3.4.2. Reduction of patient- and object-induced distortion .....  | 38        |
| 3.4.3. Measurement of patient- and object-induced distortion..... | 38        |



|  |           |
|--|-----------|
| <b>4. Synthetic CT in MRI-Only Workflows</b> .....                   | <b>41</b> |
| 4.1. Synthetic CT generation.....                                    | 43        |
| 4.2. MRI acquisition sequence development.....                       | 45        |
| 4.2.1. Patient setup and acquisition parameters.....                 | 45        |
| 4.3. Dosimetric impact from geometric distortions.....               | 48        |
| 4.4. Clinical synthetic CT validation .....                          | 50        |
| <b>5. Fiducial Marker Identification in MRI-Only Workflows</b> ..... | <b>55</b> |
| 5.1. Gold fiducial marker implantation.....                          | 55        |
| 5.2. Prostatic calcifications.....                                   | 57        |
| 5.3. MRI methods for fiducial marker identification.....             | 58        |
| 5.3.1. MEGRE image characteristics.....                              | 58        |
| 5.3.2. Manual detection performance .....                            | 60        |
| 5.4. Automatic fiducial marker identification.....                   | 62        |
| 5.4.1. Development of an automatic detection method.....             | 62        |
| 5.4.2. Automatic detection performance .....                         | 64        |
| 5.5. Quality control of fiducial marker identification.....          | 64        |
| 5.5.1. Development of a quality control method.....                  | 65        |
| 5.5.2. Quality control performance.....                              | 66        |
| <b>6. Conclusions and Future Outlook</b> .....                       | <b>69</b> |
| 6.1. Synthetic CT quality .....                                      | 69        |
| 6.2. Fiducial marker identification.....                             | 69        |
| 6.3. Clinical implementation .....                                   | 70        |
| 6.4. Future outlook .....  | 70        |
| <b>Acknowledgements</b> .....  | <b>73</b> |
| Funding.....   | 76        |
| <b>References</b> .....  | <b>77</b> |



# Abstract

A workflow based solely on MRI images for prostate radiotherapy planning eliminates the need for CT imaging and CT/MRI image registration. The density map required for the calculation of absorbed dose is generated from MRI data providing a synthetic CT image. This is referred to as an MRI-only workflow.

Geometric distortion can occur in MRI images, and will thus be propagated in the synthetic CT images. This can lead to errors in target delineation and an undesirable dosimetric impact. Gold fiducial markers are implanted in the prostate for treatment target positioning. These markers have excellent visibility in CT images, but are difficult to detect using MRI. These issues must be investigated and resolved before an MRI-only workflow can be clinically implemented.

A method has been developed to investigate the dosimetric implications and impact on structure delineation from MRI-system-related geometric distortion. The method was applied to an MRI acquisition sequence, designed specifically for synthetic CT generation. No clinically relevant dose difference ( $\leq 0.02\%$ ) or structural deformation ( $< 0.5$  mm) was found when a 3D distortion correction was applied and a high acquisition bandwidth was used.

Synthetic CT images of the male pelvis were generated using dedicated MRI acquisition sequences and commercially available software. The dosimetric accuracy and clinical robustness of the software were evaluated in a multicenter/multivendor setting. Synthetic CT generation was found to be possible with a variety of MRI systems, and radiotherapy treatment techniques, with minimal overall mean dose differences ( $< 0.3\%$ ) compared to CT.

To resolve the problem of poor visibility and detection of gold fiducial markers in MRI images, a multi-echo gradient echo acquisition sequence was developed, optimized and validated. Gold fiducial markers could then be reliably identified, with 99% detection accuracy. An MRI-independent method was developed and evaluated to confirm the location of the identified gold fiducial markers. All the fiducial markers were confirmed to have been correctly identified. The method takes advantage of an X-ray image acquired during insertion of the gold fiducial markers, prior to radiotherapy. No additional imaging was therefore required for this independent quality control step.

The methods developed and presented in this thesis can facilitate a clinically feasible and safe implementation of an MRI-only prostate radiotherapy workflow.



## Populärvetenskaplig sammanfattning

Prostatacancer är den vanligaste cancerformen i Sverige och kan behandlas med kirurgi, strålning, hormoner och cytostatika. Strålbehandling kan ges för att uppnå både bot och lindring. För att lättare kunna rikta in strålningen sätts det in guldmarkörer i prostatan. Datortomografi (CT)- och magnetresonans (MRI)-bilder används idag för att beräkna stråldos samt rita in behandlingsområde till prostatan. Patientens inre anatomi kan skilja sig åt något mellan tillfällena för CT och MRI bildtagning, vilket kan skapa osäkerheter i planeringen av strålbehandlingen. Genom att utesluta CT och endast använda MRI-bilder för behandlingsplanering kan dessa osäkerheter undvikas. Sjukhuset skulle då kunna spara pengar och patienten kan undvika en undersökning. Beräkning av stråldos i MRI-bilder är möjlig genom att omvandla dessa till konstgjorda CT bilder, kallat syntetisk CT. MRI-bilder kan tyvärr innehålla geometriska fel som därmed kan påverka strålbehandlingen. Det är heller inte lätt att med endast MRI-bilder hitta de insatta guldmarkörerna i prostatan.

I denna avhandling utvecklades metoder för att mäta och minimera betydelsen av geometriska fel i MRI-bilder. Väl anpassade MRI-bilder användes sedan för att utvärdera en kommersiell produkt som möjliggjorde strålplanering med endast MRI- och syntetiska CT-bilder. Denna utvärdering gjordes för flertalet olika typer av magnetkameror och kliniska behandlingssystem. Resultaten visar att de geometriska felen kan minskas till en nivå där de inte har en negativ påverkan på strålbehandlingen. Detta betyder att produkten är robust för olika strålbehandlingssystem och MRI-bilder från olika typer av magnetkameror och tillverkare.

Metoder utvecklades också för att utesluta CT och med endast MRI-bilder kunna hitta guldmarkörerna i prostatan. Guld ger lokala störningar i MRI-bilderna men detta visade sig kunna vändas till en fördel för att lättare hitta guldmarkörerna och skilja dessa mot andra objekt i prostatan. För att med säkerhet kunna säga att positionen för de hittade markörerna stämde med verkligheten utvecklades en MRI-oberoende metod för att bekräfta detta. Denna metod använde sig av en röntgenbild som redan hade tagits vid tillfället då guldmarkörerna sattes in i prostatan. Därför behövde ingen extra bildtagning för patienten göras.

Avhandlingen i sin helhet visar att det är möjligt att utesluta CT samt införa en säker MRI-baserad planering av strålbehandling till prostata. Förhoppningen är att kunna förbättra framtida behandlingar så att bättre bot uppnås samtidigt som patienten får mindre biverkningar, då detta är en mer noggrann metod.



## Original papers

This thesis is based on four publications, referred to in the text by their Roman numerals:

Paper I      **Assessment of dosimetric impact of system specific geometric distortion in an MRI only based radiotherapy workflow for prostate**  
Christian Gustafsson, Fredrik Nordström, Emilia Persson, Johan Brynolfsson, and Lars E. Olsson. *Physics in Medicine & Biology*, 62(8):2976-89 (2017)

Paper II     **MR-OPERA: A Multicenter/Multivendor Validation of Magnetic Resonance Imaging-Only Prostate Treatment Planning Using Synthetic Computed Tomography Images**  
Emilia Persson, Christian Gustafsson, Fredrik Nordström, Maja Sohlín, Adalsteinn Gunnlaugsson, Karin Petruson, Nina Rintelä, Kristoffer Hed, Lennart Blomqvist, Björn Zackrisson, Tufve Nyholm, Lars E. Olsson, Carl Siversson, and Joakim Jonsson. *International Journal of Radiation Oncology Biology Physics*, 99(3):692-700 (2017)

Paper III    **Registration free automatic identification of gold fiducial markers in MRI target delineation images for prostate radiotherapy**  
Christian Gustafsson, Juha Korhonen, Emilia Persson, Adalsteinn Gunnlaugsson, Tufve Nyholm, and Lars E. Olsson. *Medical Physics*, 44(11):5563-5574 (2017)

Paper IV    **Using C-Arm X-ray images from marker insertion to confirm the gold fiducial marker identification in an MRI-only prostate radiotherapy workflow**  
Christian Gustafsson, Emilia Persson, Adalsteinn Gunnlaugsson, and Lars E. Olsson. *Journal of Applied Clinical Medical Physics*, 19(6):185-192 (2018)

**Paper I** is reproduced with permission from IOP Publishing. **Papers II, III and IV** are published under Open Access license.

## The author's contributions

This is a summary of the author's contributions to each paper:

- Paper I        The author participated in the design and execution of the study, took part in the development of the phantom, and performed all phantom MRI measurements. The author wrote the code for the image processing and analysis pipeline, performed the dose calculations, and carried out the analysis of the data. The author was the main author of the paper.
- Paper II        The author participated in the design of the study and designed and validated the MRI acquisition protocol used. The author was involved in the choice of evaluation methods, the analysis of the results, and contributed to writing the paper.
- Paper III       The author developed the idea, designed the study, and optimized and validated the MRI acquisition sequence on phantoms and *in vivo*. The author anonymized the data and wrote the code for the graphical user interface and image processing pipeline. The author analyzed the data, and was the main author of the paper.
- Paper IV        The author developed the idea and designed the study. The author collected and anonymized the data and wrote the code for the graphical user interface and image processing pipeline. The author analyzed the data and was the main author of the paper.



## Related publications

- **Intensity-based dual model method for generation of synthetic CT images from standard T2-weighted MR images – Generalized technique for four different MR scanners**  
Lauri Koivula, Mika Kapanen, Tiina Seppälä, Juhani Collan, Jason A. Dowling, Peter B. Greer, Christian Gustafsson, Adalsteinn Gunnlaugsson, Lars E. Olsson, Leonard Wee, and Juha Korhonen. *Radiotherapy and Oncology*, 125(3):411-419 (2017)
- **Dose integration and dose rate characteristics of a NiPAM polymer gel MRI dosimeter system**  
Christian Waldenberg, Anna Karlsson Hauer, Christian Gustafsson, and Sofie Ceberg. *Journal of Physics: Conference Series*, 847:012063 (2017)
- **MR and CT data with multiobserver delineations of organs in the pelvic area – Part of the Gold Atlas project**  
Tufve Nyholm, Stina Svensson, Sebastian Andersson, Joakim Jonsson, Maja Sohlin, Christian Gustafsson, Elisabeth Kjellén, Karin Söderstrom, Per Albertsson, Lennart Blomqvist, Björn Zackrisson, Lars E. Olsson, and Adalsteinn Gunnlaugsson. *Medical Physics*, 45(3):1295-1300 (2018)
- **Cone beam CT for QA of synthetic CT in MRI only for prostate patients**  
Emilia Palmér, Emilia Persson, Petra Ambolt, Christian Gustafsson, Adalsteinn Gunnlaugsson, and Lars E. Olsson. *Journal of Applied Clinical Medical Physics*, 19(6):44-52 (2018)
- **Target definition in radiotherapy of prostate cancer using magnetic resonance imaging only workflow**  
Adalsteinn Gunnlaugsson, Emilia Persson, Christian Gustafsson, Elisabeth Kjellén, Petra Ambolt, Silke Engelholm, Per Nilsson, and Lars E. Olsson. *Physics and Imaging in Radiation Oncology*, 9:89-91 (2019)

## Preliminary reports

The following preliminary reports have been given at international meetings:

- **A novel method to assess dosimetric impact of system specific geometric distortions in an MRI-only workflow**  
Christian Gustafsson, Fredrik Nordström, Emilia Persson, and Lars E. Olsson. *4th MR in RT Symposium (poster)*, Ann Arbor, MI, USA, 2016
- **Multi-center/multi-vendor validation of MRI only prostate treatment planning**  
Emilia Persson, Christian Gustafsson, Fredrik Nordström, Maja Sohlin, Adalsteinn Gunnlaugsson, Karin Petruson, Nina Rintelä, Kristoffer Hed, Lennart Blomqvist, Björn Zackrisson, Tufve Nyholm, Lars E. Olsson, Carl Siversson, and Joakim Jonsson. *4th MR in RT Symposium (poster)*, Ann Arbor, MI, USA, 2016
- **Automatic identification of gold fiducial markers in MRI target delineation images intended for prostate radiotherapy without the need for image registration**  
Christian Gustafsson, Juha Korhonen, Emilia Persson, Tufve Nyholm, and Lars E. Olsson. *5th MR in RT Symposium (talk)*, Sydney, Australia, 2017
- **Clinical validation of MR-only prostate treatment planning in a multi-center/multi-vendor environment and patient positioning feasibility using synthetic CT images**  
Emilia Persson, Christian Gustafsson, Fredrik Nordström, Maja Sohlin, Adalsteinn Gunnlaugsson, Karina Petruson, Nina Rintelä, Kristoffer Hed, Lennart Blomqvist, Björn Zackrisson, Tufve Nyholm, Lars E. Olsson, Carl Siversson, and Joakim Jonsson. *5th MR in RT Symposium (talk)*, Sydney, Australia, 2017
- **C-Arm X-ray images can indicate accurate gold fiducial marker identification in a prostate MRI-only radiotherapy workflow.**  
Christian Gustafsson, Emilia Persson, Adalsteinn Gunnlaugsson, and Lars E. Olsson. *60th AAPM Annual Meeting & Exhibition (poster)*, Nashville, TN, USA, 2018
- **Multimodality assessment of gold fiducial marker inter-distance measurements for prostate patients in an MRI-only based radiotherapy workflow**  
Christian Gustafsson, Emilia Persson, Emilia Palmér, and Lars E. Olsson. *60th AAPM Annual Meeting & Exhibition (poster)*, Nashville, TN, USA, 2018
- **Indication of accurate gold fiducial marker identification in a prostate MRI only radiotherapy workflow using C-Arm X-ray imaging**  
Christian Gustafsson, Emilia Persson, Adalsteinn Gunnlaugsson, and Lars E. Olsson. *6th MR in RT Symposium (talk)*, Utrecht, the Netherlands, 2018

# Abbreviations

|       |                                    |
|-------|------------------------------------|
| 2D    | 2-Dimensional                      |
| 3D    | 3-Dimensional                      |
| $B_0$ | Main static magnetic field         |
| CBCT  | Cone Beam Computed Tomography      |
| CkV   | C-Arm X-ray                        |
| CT    | Computed Tomography                |
| CTV   | Clinical Target Volume             |
| DRR   | Digitally Reconstructed Radiograph |
| DVH   | Dose Volume Histogram              |
| EBRT  | External Beam Radiation Therapy    |
| FOV   | Field Of View                      |
| FSE   | Fast Spin-Echo                     |
| GRE   | Gradient Echo                      |
| GTV   | Gross Tumor Volume                 |
| GUI   | Graphical User Interface           |
| HU    | Hounsfield Units                   |
| kV    | Kilo Voltage                       |
| MEGRE | Multi-Echo Gradient Echo           |
| MRI   | Magnetic Resonance Imaging         |
| OAR   | Organ(s) At Risk                   |
| PTV   | Planning Target Volume             |
| RTP   | Radiotherapy Treatment Planning    |
| sCT   | Synthetic CT                       |
| T2w   | T2-weighted                        |
| TPR   | True Positive Rate                 |
| VMAT  | Volumetric Modulated Arc Therapy   |
| QA    | Quality Assurance                  |
| QC    | Quality Control                    |



# 1. Introduction

Prostate cancer is the second most common diagnosed malignancy among men worldwide, and is the fifth leading cause of cancer mortality in men with cancer (Ferlay et al., 2015). External beam radiation therapy (EBRT) offers treatment by delivery of high radiation doses to the prostate cancer cells. The prescribed total radiation dose is divided into treatment fractions, given over a period of time, typically 3-8 weeks (Benedek et al., 2018).

Due to its excellent geometric accuracy, computed tomography (CT) has been the primary imaging modality used for external beam radiotherapy treatment planning (RTP) and delineation of the target and organs at risk (OAR). CT is crucial in providing tissue Hounsfield units (HU), which can be converted into electron density, to enable the calculation of absorbed dose. CT images are also used for patient positioning for treatment delivery (IAEA, 2016). However, the limited soft tissue contrast in CT images constitutes a major drawback in the delineation of the target and the OAR (Villeirs et al., 2005). The weakest link in the radiotherapy treatment process is associated with definition and delineation of the target volume (Segedin and Petric, 2016). Due to the superior image contrast of magnetic resonance imaging (MRI), the use of MRI systems in radiotherapy clinics has become widespread in recent years (Karlsson et al., 2009, Blomqvist et al., 2013, Metcalfe et al., 2013) (Figure 1). The role of prostate MRI in radiation oncology was recently reviewed, and an increased need for MRI imaging in the radiotherapy workflow was identified (Menard et al., 2018).



**Figure 1. Image contrast in CT and MRI images**

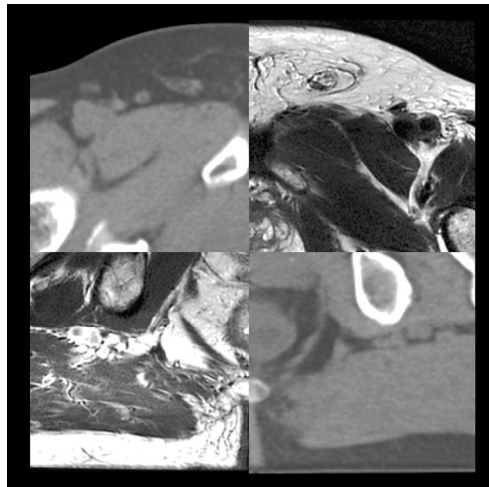
A cropped transverse pelvic CT image is shown on the left. Corresponding anatomy in a small field of view T2-weighted (T2w) MRI image is shown on the right. MRI images have superior soft tissue contrast compared to CT images, as can be clearly seen in the prostate area. The bright object located in the prostate in the CT image, and surrounded by streak artefacts, is an implanted gold fiducial marker. In the MRI image, the fiducial marker appears as a small signal void.

## 1.1. Image registration

In order to take full advantage of the superior soft tissue contrast in MRI images for prostate RTP, CT and MRI images must have a common geometric frame of reference. This is achieved by image registration. Registration algorithms based on mutual information are the most common when images originate from different imaging modalities (Brunt, 2010, Oliveira and Tavares, 2014) (Figure 2).

CT/MRI image registration for the prostate can lead to systematic spatial uncertainties in the RTP (Nyholm et al., 2009). A spatial uncertainty of 1.7-2 mm for CT/MRI image registration for patients with and without fiducial markers has been reported in studies investigating the magnitude of registration errors (Roberson et al., 2005, Nyholm et al., 2009, Korsager et al., 2016, Wegener et al., 2019).

It is important to note that systematic errors in RTP require 3 to 4 times greater safety margin than random errors. (Margin is defined in Section 1.3). A systematic registration error could result in a systematic treatment error that persists throughout all the treatment fractions. This could lead to displacement of the dose distribution away from the target, and compromise tumor control (van Herk et al., 2000, van Herk, 2004).



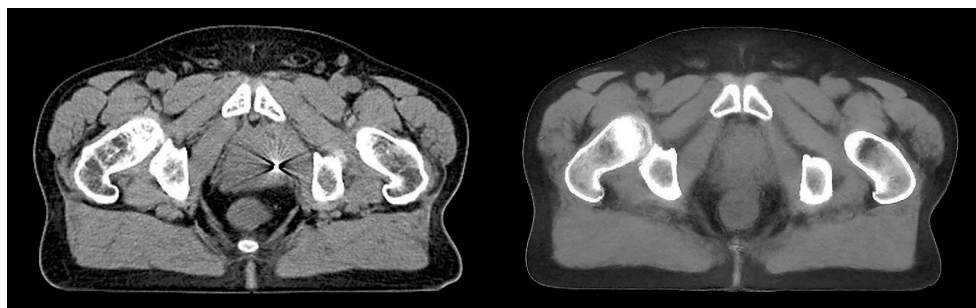
**Figure 2. Image registration in a CT/MRI workflow**

Image registration based on mutual information in a small field of view MRI image and a CT image (cropped). Image registration is required when MRI images are used for target delineation in a combined CT/MRI workflow. This can introduce additional systematic spatial uncertainties in radiotherapy planning.

## 1.2. MRI-only

The spatial uncertainty resulting from CT/MRI image registration can be avoided by excluding the CT imaging from the RTP workflow, and performing target and OAR delineation using only information from the MRI image (Fransson et al., 2001, Nyholm and Jonsson, 2014). Such a workflow is referred to as an MRI-only workflow, or an MRI-based workflow. In a conventional workflow, CT provides information on electron density (from HU), which is used to calculate the absorbed dose. In an MRI-only workflow, this information must be retrieved by other means.

HU information can be obtained from MRI images using a conversion process in which the new images are referred to as “synthetic CT” (Siversson et al., 2015, Persson et al., 2017, Tyagi et al., 2017a), “pseudo CT” (Korhonen et al., 2014b, Christiansen et al., 2017, Maspero et al., 2017a) or “substitute CT” (Johansson et al., 2012, Edmund and Nyholm, 2017). The term synthetic CT images will be used throughout this thesis. Synthetic CT images (denoted sCT images) are very similar to conventional CT images but they have a “smoother” appearance. This is due to the nature of the method used in sCT generation (Figure 3).



**Figure 3. Conventional CT image and a synthetic CT image**

A transverse pelvic CT image is shown on the left. Corresponding anatomy in a sCT image is shown on the right. The sCT image was generated from a large field of view T2w MRI image using MriPlanner software (Spectronic Medical AB). The sCT image provides HU information, required for the calculation of the absorbed dose in an MRI-only workflow.

## 1.3. Patient positioning

Regardless of whether RTP is based on CT or sCT images, a reproducible patient and target setup is essential for each radiotherapy treatment fraction, to ensure accurate dose delivery and to minimize the damage to normal tissue. In prostate RTP, the radiation target is defined as the clinical target volume (CTV), which includes the gross tumor volume (GTV) together with an estimate of the microscopic spread of the disease around the GTV.

A margin is then added to the CTV to take into account uncertainties in treatment planning or delivery, leading to the definition of the planning target volume (PTV) (Landberg et al., 1993, van Herk, 2004).

The pelvic bone structure can be used as a landmark for patient positioning, but the position of the prostate relative to the bone structure will vary due to motion (Schallenkamp et al., 2005). Small cylindrically shaped gold fiducial markers are therefore usually implanted in the prostate prior to the start of the EBRT, which are used for target localization during each fraction of the treatment. Gold fiducial markers improve the localization of the prostate target during radiotherapy (Kupelian et al., 2005, Scarbrough and Fuller, 2006, van der Heide et al., 2007). They can thereby reduce the margin between the CTV and PTV, which is added to ensure adequate dose coverage of the prostate (Beard et al., 1996, Greer et al., 2008).

When the patient has been positioned on the treatment table, built-in image guidance techniques, such as orthogonal kilo-voltage (kV) X-ray imaging or cone beam computed tomography (CBCT), can be used to visualize the gold fiducial markers. The location of the fiducial markers acts as a surrogate for the location of the prostate (Scarbrough and Fuller, 2006, O'Neill et al., 2016). CT and sCT images can be used to create digitally reconstructed radiograph (DRR) images, which are reconstructed 2D image projections of the patient (Pallotta and Bucciolini, 2010, Korhonen et al., 2015). These images can also show the positions of the gold fiducial markers (Figure 4).

DRR images are used in combination with orthogonal kV X-ray images for patient position verification by adjusting the prostate target position for each treatment fraction to the designated position in the treatment plan. When using an MRI-only workflow, which relies solely on bone imaging for patient setup, DRR images from the sCT must be generated with accurate bone positions. The feasibility of this has been demonstrated with both non-commercial (Korhonen et al., 2015) and commercial sCT generation methods (Kempainen et al., 2018).

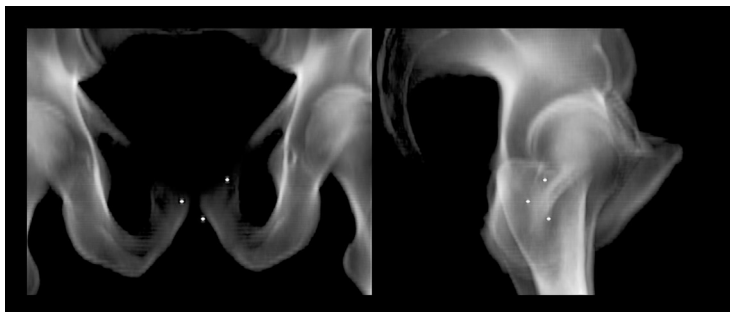


**Figure 4. Frontal and lateral DRR images**

DRR images, showing frontal and lateral projections, reconstructed from sCT images. The bone structures are clearly visible. The three round high-intensity structures in each image represent the gold fiducial markers. The positions of the fiducial markers were determined using only MRI images, and the round structures were added in the sCT generation process. Both bone structures and the fiducial markers can be used for patient positioning.



## 1.4. Opportunities in MRI-only workflows

MRI-only workflows offer other advantages, apart from the elimination of the spatial uncertainty due to CT/MRI image registration. Patient setup and anatomical changes, such as bladder and rectum filling between CT and MRI examinations, can affect delineation of the target and the OAR (Kerkhof et al., 2008, Schmidt and Payne, 2015). The difficulties regarding prostate target delineation due to such problems could be avoided by exclusion of the CT images (Tyagi et al., 2017a, Pathmanathan et al., 2018).

The exclusion of CT imaging could save time and potentially enable radiotherapy clinics to cut cost per patient, and reduce the complexity of the workflow (Tyagi et al., 2017a, Henderson et al., 2018, Kerkmeijer et al., 2018, Owrangi et al., 2018, Tenhunen et al., 2018). A time saving of about 15 minutes was recently reported in a clinical MRI-only treatment study, compared to a combined CT/MRI workflow (Tyagi et al., 2017a).

The spatial uncertainties introduced by image registration could be detrimental, especially when sharp dose gradients are required together with small margins, such as in stereotactic radiotherapy approaches, where the requirement on geometric accuracy is higher (Thwaites, 2013). An MRI-only workflow could help to improve the precision of such radiotherapy treatment (Henderson et al., 2018).

Excluding CT imaging also reduces the exposure of the patient to ionizing radiation. However, the contribution from CT imaging is on the order of mGy, and is probably negligible compared to the dose administered during radiotherapy (Tenhunen et al., 2018, Wood et al., 2018). The dose reduction when using an MRI-only workflow could be of interest when repeated imaging is necessary, for example, for treatment adaptation involving weekly scans.

## 1.5. Challenges in MRI-only workflows

The development of MRI-only workflows is strongly influenced by compatibility requirements between new solutions and established clinical routines for RTP and patient positioning. This pose a number of challenges that must be addressed.

MRI images can suffer from both patient- and MRI-system-specific geometric distortion, which can affect both target and OAR delineation, and propagate into the generated sCT image. Concerns have therefore been raised regarding the geometric accuracy in MRI images, and their use in RTP (Chen et al., 2004, Chen et al., 2006, Walker et al., 2016, Weygand et al., 2016).

Quality control (QC) tools and the validation of MRI acquisition sequences designed specifically for MRI-only RTP, are therefore of great importance. Furthermore, it is important to validate the robustness of the sCT generation method and its dosimetric integrity for a variety of magnetic field strengths, vendors, and treatment techniques.

Gold fiducial markers for treatment target positioning can be easily identified in CT images as they appear as hyper-intense objects with streak artefacts (as can be seen in Figure 5) (Kassim et al., 2011, Chan et al., 2015). An MRI-only workflow requires the identification of fiducial markers to be performed using only the MRI images. This is challenging due to difficulties in differentiating gold fiducial markers from intraprostatic bleeding and calcifications (Kapanen et al., 2013, Ghose et al., 2016, Dinis Fernandes et al., 2017, Maspero et al., 2017c, Maspero et al., 2018b) (Figure 5).

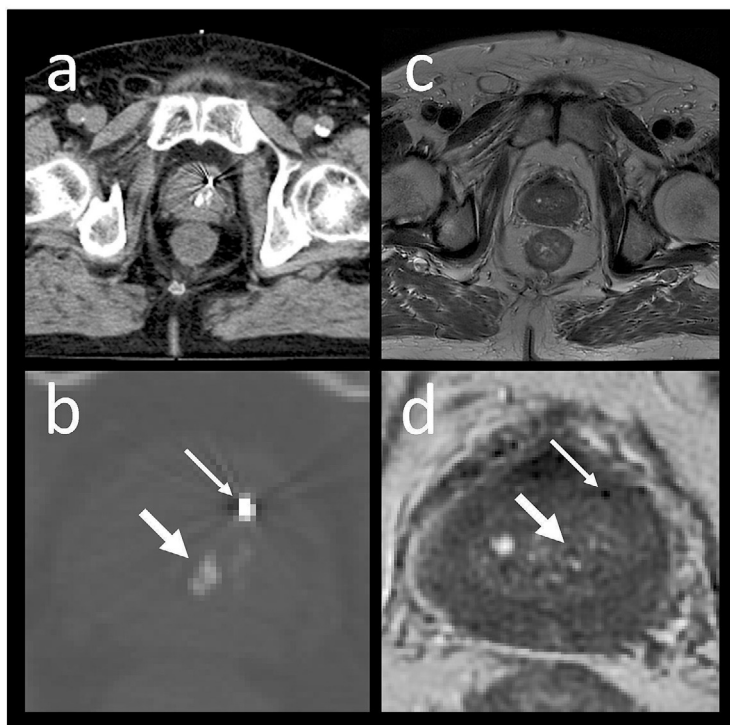


**Figure 5. Gold fiducial marker and calcification in CT and MRI images**

A cropped transverse pelvic CT image is shown in (a) and an enlarged image of the prostate in (b). Corresponding anatomy in a transverse small field of view T2w MRI image is shown in (c) and in (d). This MRI image is used to delineate the target volume in prostate RTP. The thin arrow indicates the location of a gold fiducial marker, while the thick arrow indicates a prostatic calcification. As can be seen in the CT image, the gold fiducial marker appears as a hyper-intense object, surrounded by streak artefacts, while the calcification is not. This makes differentiation between these objects easy in CT images, whereas in the MRI images, both objects are hypo-intense, and are visualized as signal voids, which makes differentiation difficult.

Uncertainties or problems in identifying gold fiducial markers have been reported to be the greatest obstacles to the successful implementation of MRI-only prostate radiotherapy (Tyagi et al., 2017a, Tenhunen et al., 2018). To make fiducial marker identification as cost-effective as possible, and to minimize observer bias, the fiducial detection process would also benefit from automation. It is therefore of interest to develop, investigate and validate MRI acquisition sequences, automatic gold fiducial marker detection frameworks and QC methods for these purposes. Together with a robust and accurate multi-vendor sCT generation method, this could facilitate the widespread implementation of an MRI-only prostate radiotherapy workflow.



## 2. Aims

The primary focus of the work presented in this thesis was MRI-related quality control (QC) aspects in the implementation of an MRI-only prostate radiotherapy workflow using gold fiducial markers for prostate target positioning.

The specific aims were:

- To develop and apply a QC method to assess the impact of MRI-system-specific geometric distortion in MRI images intended for sCT generation of the male pelvis (**Paper I**).
- To evaluate the dosimetric accuracy and clinical robustness of a commercially available sCT generation method for prostate radiotherapy in a variety of different MRI systems and radiotherapy clinics (**Paper II**).
- To develop and evaluate methods for MRI-based manual and automatic prostate gold fiducial marker detection with appropriate independent QC (**Papers III and IV**).



# 3. MRI in Radiotherapy

Computed tomography (CT) provides excellent images of high-density tissues such as bone for RTP. It has high geometric accuracy, and provides information on electron density from HU, required to calculate the absorbed dose. CT also provides image data suitable for patient posing during radiotherapy. Unfortunately, CT images have limited soft tissue contrast, while MRI offers outstanding soft tissue contrast, and can therefore contribute to improved target and OAR delineation for RTP in several ways (Chandarana et al., 2018). MRI has been available as a complementary image modality for target and OAR definition since the beginning of the 1990s, and is being increasingly used for RTP (Dirix et al., 2014). Image acquisition using MRI enables oblique slice directions with a multitude of different image contrasts without using any ionizing radiation. MRI is unfortunately not without limitations, and in this chapter potential obstacles to the implementation of MRI images in RTP will be addressed.

Firstly, MRI images can be associated with geometric distortion, which could introduce systematic errors in radiotherapy planning and treatment. Knowledge of the origin of geometric distortion and strategies to reduce it are essential if MRI images are to be used in RTP. Secondly, the combination of CT- and MRI images for RTP often requires image registration into a common geometric frame of reference (Paulson et al., 2015, Schmidt and Payne, 2015), which could introduce additional spatial uncertainties (Roberson et al., 2005, Nyholm et al., 2009, Ulin et al., 2010, Dean et al., 2012). It is therefore of the utmost importance to select MRI sequences and acquisition parameters carefully, so as to ensure that they are appropriate for the anatomical site of interest for MRI imaging intended for RTP.

## 3.1. MRI simulation in radiotherapy

MRI images are acquired for the purpose of target- and OAR delineation, and it is desirable to ensure the same patient position at MRI and dose delivery during radiotherapy (Schmidt and Payne, 2015).

### 3.1.1. Patient positioning

Flat tables are used in radiotherapy clinics to improve the reproducibility of patient positioning. Most standard MRI systems intended for diagnostic purposes have curved table tops for increased patient comfort, and one of the adaptations required is therefore a flat table top (McJury et al., 2011, Schmidt and Payne, 2015, Sun et al., 2015b). A flat table top also enables the use of knee and ankle positioning devices.

Compression or deformation of the patient anatomy should be avoided. If the MRI receiver coil is of substantial weight, it should therefore not rest on the patient (Figure 13). This can be achieved using supports on which the coil is placed (Kapanen et al., 2013, Sun et al., 2014, Paulson et al., 2015). The need for a larger space within the MRI system, due to patient fixation devices such as whole-body vacuum cushions, also makes wide-bore MRI systems with a 70 cm diameter preferable for radiotherapy planning. Laser systems are also commonly installed in the MRI room to be compatible with radiotherapy patient positioning routines.

### 3.1.2. Imaging

MRI images can improve target definition for radiotherapy of prostate cancer, enabling better target visualization, and reduced variability in target delineation (Debois et al., 1999, Parker, 2003, Hricak, 2005, Villeirs et al., 2005, Jackson et al., 2007, Hentschel et al., 2011, Usmani et al., 2011) (Figure 6). Fast spin-echo (FSE) T2-weighted (T2w) imaging of the prostate is recommended as it enables visualization of the internal structure of the prostate, and is sensitive to pathology (Villeirs and De Meerleer, 2007, Barentsz et al., 2012).

Specifically, T2w MRI imaging enables more precise visualization and location of the prostate base (cranial direction) and apex (caudal direction) than CT imaging (Roach et al., 1996, Rasch et al., 1999, Parker, 2003, Usmani et al., 2011) (Figure 6). The improvement in target delineation may also reduce the absorbed dose to the OAR such as the rectum and penile erectile tissue (Steenbakkers et al., 2003, Villeirs et al., 2005, Jackson et al., 2007, Sander et al., 2014). MRI can also be beneficial when patients have bilateral hip prostheses, which show large streak artefacts on CT images (Rosewall et al., 2009).

Within the framework of a national Swedish project called Gentle Radiotherapy, sponsored by the Swedish Innovation Agency, VINNOVA, the author of this thesis co-authored a guide on the use of MRI in radiotherapy planning (Gustafsson et al., 2016). The purpose of this guide was primarily to serve as a handbook describing how MRI imaging intended for RTP could be performed on several anatomies, using different MRI systems from different vendors, and a number of patient immobilization devices.



As a result of the superior image contrast in MRI images compared to CT images, overestimation of the delineated prostate volume has been observed in CT images (Seppala et al., 2015). A 2%-40% reduction in prostate volume has been reported using MRI images (together with CT images) for prostate target delineation (Jackson et al., 2007). A mean volume reduction of 18% has been reported upon changing from prostate target delineation dependent on the combination of CT and MRI images, to MRI images only (Gunnlaugsson et al., 2019). Other studies have shown only a moderate decrease in the prostate volume when using MRI images, which was explained by long radiologist experience, or an increase in awareness regarding target overestimation when using CT images only (Parker, 2003, Villeirs and De Meerleer, 2007, Usmani et al., 2011).

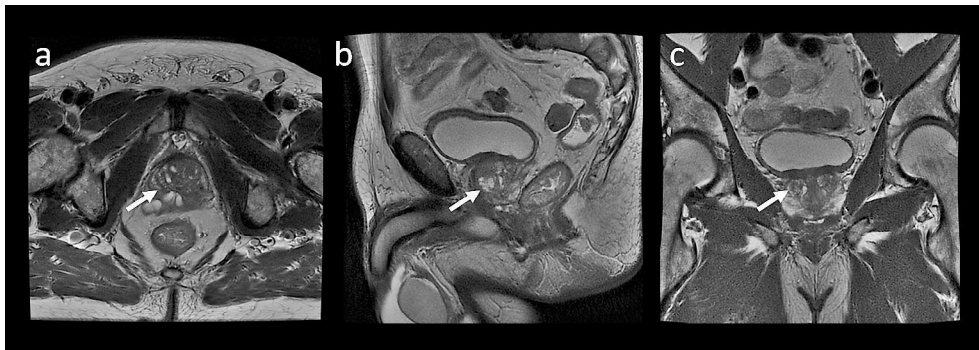


**Figure 6. Prostate target visualization using MRI**  
The white arrow indicates the location of the prostate in acquired T2w transverse (a), sagittal (b) and coronal (c) MRI images. This enables the visualization of the prostate base (cranial direction) and apex (caudal direction).

### 3.2. MRI image distortion

Spatial accuracy is of the utmost importance in RTP, and concerns have therefore been raised regarding the impact of spatial distortion in MRI images, when used in radiotherapy planning (Chen et al., 2004, Chen et al., 2006, Walker et al., 2016, Weygand et al., 2016). Image distortion exceeding 2 mm in the image field of view (FOV) has been suggested as the level requiring consideration (Walker et al., 2015, IAEA, 2016, Weygand et al., 2016). This is also the geometric accuracy specified for CT (IAEA, 2004, IAEA, 2016).

MRI image distortion can be both MRI-system-induced and patient-induced (Fransson et al., 2001), and can be measured using a variety of techniques, some of which are addressed in this thesis.

Patient-induced geometric distortion is roughly an order of magnitude smaller than (uncorrected) MRI-system-induced distortion (Stanescu et al., 2012), but could be the dominating source after correction for MRI-system-induced distortion (Adjeiwaah et al., 2018, Kerkmeijer et al., 2018).

An uncertainty in the target volume, in combination with modern radiotherapy techniques utilizing sharp dose gradients will directly propagate into a dosimetric deviation in the target coverage. The spatial distortion for target regions should therefore be  $< 1$  mm (Baldwin et al., 2007, Thwaites, 2013, Weygand et al., 2016).

In modern MRI systems the system-induced distortion is deterministic, and can be corrected with software provided by the vendor. However, some geometric distortion will remain. Patient-/object-induced geometric distortion depends on the geometry of the individual patient/object, and can only be corrected for by post-processing (Lundman et al., 2017). Deviations in image intensity may also be caused by both system-induced and patient-/object-induced geometric distortion (Michiels et al., 1994, Tanner et al., 2000, Doran et al., 2005, Baldwin et al., 2009), however, this will not be addressed in this thesis.

### 3.3. System-induced geometric distortion

The signal in MRI is created by the external static magnetic field. The most common field strength in clinical MRI systems intended for imaging in RTP is 0.35 T-3 T. MRI-system-specific distortion can originate from non-linear spatial encoding gradients and from inhomogeneities in the main static magnetic field ( $B_0$ ) (Bakker et al., 1992, Doran et al., 2005, Reinsberg et al., 2005). Signal localization and image generation in MRI systems are dependent on linearly varying magnetic fields, which also vary in time with a field strength variation on the order of mT. These non-static magnetic fields are created by magnetic field gradient coils embedded in the MRI system, referred to as spatial encoding gradient coils, and are superimposed on the static field. The spatial directions in which these non-static gradient fields are applied are denoted the slice-encoding direction, the frequency-encoding direction, and the phase-encoding direction. Geometric distortion due to non-linear gradients is independent of the MRI acquisition sequence used, while geometric distortion from inhomogeneities in  $B_0$  is dependent on the acquisition sequence used (Baldwin et al., 2009).

Eddy currents can also be induced in the MRI system due to strong spatial encoding gradients, resulting in additional time varying magnetic field gradients. The induced field gradients could lead to undesirable image artefacts, but is most pronounced in localized magnetic resonance spectroscopy and diffusion-weighted MRI experiments (Baldwin et al., 2007, Spees et al., 2011). Hence, eddy currents are not further considered in this thesis.

### 3.3.1. Non-linear MRI gradients

In image reconstruction, it is assumed that the magnetic field gradient created produces magnetic field variations that vary linearly with distance from the isocenter of the MRI system. If the magnetic resonance precession frequency deviates from its expected value, for example, due to a non-linear magnetic field gradient, the spatial position of an object will be affected in the reconstructed image (Bakker et al., 1992, Reinsberg et al., 2005, Baldwin et al., 2007).

A loss of gradient linearity is typically observed at large distances from the MRI system isocenter (Weygand et al., 2016) (Figure 7). The non-perfect gradient linearity thus creates spatial distortion and blurring in the outer parts of the MRI image as the geometric distortion increases with increasing distance from the MRI system isocenter (Chen et al., 2004, Wang et al., 2004, Doran et al., 2005, Walker et al., 2015). If not corrected for, this source of distortion has been shown to be the greatest, with reported values  $> 1$  cm (Walker et al., 2015, Weygand et al., 2016).

Such geometric distortion might be acceptable in diagnostic MRI, but in RTP, this degree of image distortion is often unacceptable (Weygand et al., 2016). This is especially important for a large FOV in MRI images, which is needed for sCT image generation in the male pelvis (Torfeh et al., 2016, Edmund and Nyholm, 2017, Johnstone et al., 2018) (Figure 7).

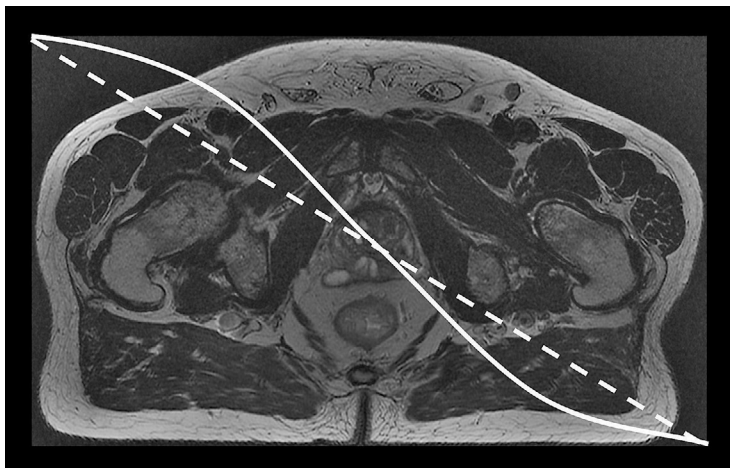


**Figure 7. Non-linear MRI spatial encoding gradient**

A linear in-plane spatial encoding gradient (dashed line) and a non-linear spatial encoding gradient (solid line) are shown for large radial distances. If not corrected for, the non-linear deviation in the spatial encoding gradient can result in image distortion.

### 3.3.2. Magnetic field inhomogeneities

Generation of a homogeneous static magnetic field within the entire measurement volume of an MRI system is in general not possible, and a deviation of a few parts per million in the field strength can be expected (GE-Healthcare, 2011). The homogeneity is greatest at the isocenter of the MRI system and decreases with increasing radius. Any deviation in the static magnetic field will alter the magnetic resonance frequency locally, introducing a perturbation into the linearly changing magnetic resonance frequencies (McRobbie, 2007).

As in the case of non-linear spatial encoding gradients, a deviation in  $B_0$  will result in geometric distortion. However, there are differences in the nature of these two sources of distortion. Deviations in  $B_0$  from magnetic field inhomogeneities will only give rise to geometric distortion in the direction of the applied spatial frequency-encoding gradient. The geometric distortion resulting from non-linear gradients is, however, not limited to any specific spatial direction (Tanner et al., 2000, Baldwin et al., 2007). It should be noted that the directional dependence on deviations in  $B_0$  discussed here is limited to linear Cartesian signal encoding, which is not based on echo-planar imaging. This covers the acquisition sequences most commonly used for morphological imaging.

### 3.3.3. Reduction of system-induced distortion

The geometric distortion resulting from non-linear gradients does not scale with gradient strength, it is constant between scans, and is not limited to the frequency-encoding axis (Bakker et al., 1992, Baldwin et al., 2007). It can be corrected in 2D (in-plane) or 3D (in-plane and through-plane) using vendor-specific software (Wang et al., 2004). 2D and 3D distortion corrections for non-linear gradients can be based on approximations of the distortion field using analytical expressions such as those for spherical harmonics (Janke et al., 2004). This mathematical concept is used in the vendor-based gradient non-linearity correction algorithm GradWarp, designed by GE Healthcare (Milwaukee, WI, USA). If not corrected for, the effects of geometric distortion, can be substantial (Figure 8).

Geometric distortion arising from inhomogeneities in  $B_0$  can be reduced by magnetic field shimming (Michiels et al., 1994, Fransson et al., 2001, Weygand et al., 2016). The effect of residual magnetic field inhomogeneities after shimming can be reduced by using a higher acquisition bandwidth (Bakker et al., 1992, Baldwin et al., 2007). In the present work, these effects were reduced by 3D distortion correction and shimming, and high acquisition bandwidth was enabled, where applicable.

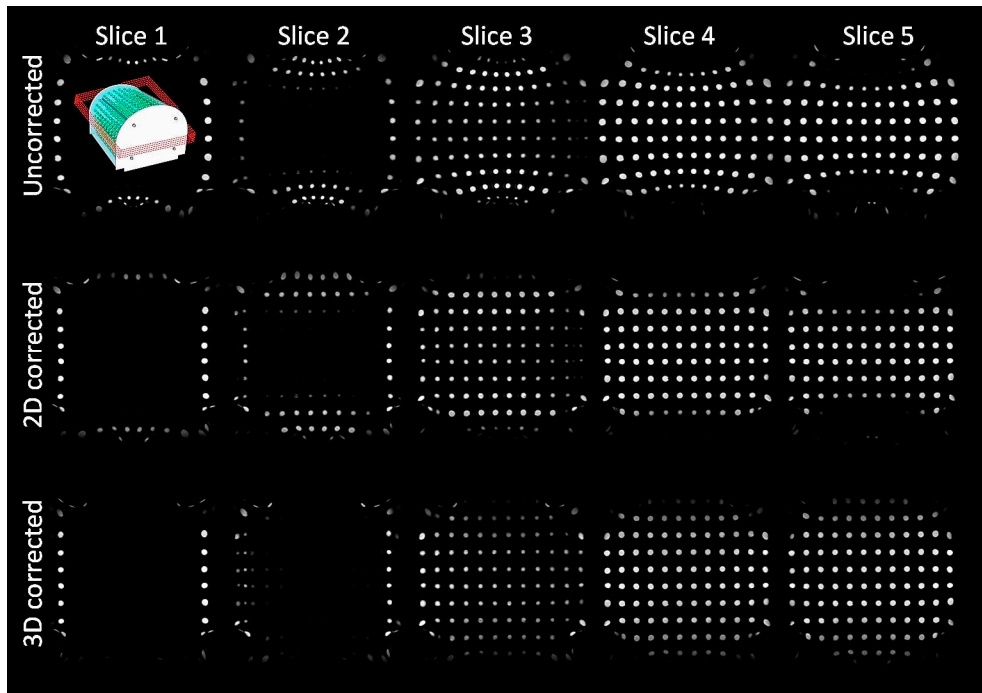


**Figure 8. Effects of geometric distortion and distortion correction**

Five consecutive coronal image slices are shown acquired from the Spectronic Medical GRADE phantom. In the upper row, no geometry distortion correction has been applied, while in the middle row 2D in-plane correction has been applied. In the lower row, 3D in-plane + through-plane geometry distortion corrections have been applied. Slice orientation is shown in the upper left corner (phantom details are given elsewhere in Figure 9). Geometric distortion is clearly visible in the peripheral part of the FOV for the uncorrected image data (upper row), where the straight lines of phantom markers are seen to be curved. The geometry distortion is greatly reduced in the 2D-distortion-corrected data. A difference in the number of signal markers for the same slice can be observed for 2D- and 3D-corrected data due to non-linearities in the slice-encoding spatial gradient, placing the signal markers in an incorrect slice position. This is compensated for by the 3D distortion correction. Image data were acquired using a 2D multi-slice T1-weighted FSE sequence on a 3T GE Discovery 750w MRI system. FOV=50 cm (square), in-plane resolution=2 mm (square), slice thickness=5 mm, slice spacing=0 mm, repetition time=1000 ms and echo time=8.4 ms. It should be noted that 2D distortion correction is enabled by default on GE MRI systems, while 3D distortion correction is optional.

### 3.3.4. Measurement of system-induced distortion

Numerous methods have been presented for the measurement and mapping of MRI-system-specific geometric distortion using large-volume geometric phantoms (Chen et al., 2006, Walker et al., 2015, Huang et al., 2016, Torfeh et al., 2016, Price et al., 2017, Stanescu and Jaffray, 2018). These phantoms often rely on signal markers located at known spatial positions. To assess the geometric distortion and calculate displacement maps, the marker positions are measured in the MRI images and compared to their physical location.

In the study presented in **Paper I**, the MRI-system-dependent geometry distortion was assessed using a lightweight (< 10 kg) commercial large-volume phantom and cloud-based analysis software (GRADE) (Spectronic Medical AB, Helsingborg, Sweden). 3D distortion correction was enabled in all measurements. The GRADE phantom consisted of 1177 spherical markers embedded in extruded polystyrene foam at known locations (Figure 9). The GRADE software automatically calculates the phantom marker locations in the MRI images and compares them with a digital reference phantom model, allowing a 3D distortion field to be produced. The GRADE phantom has also been subjected to investigation of its sensitivity to setup errors. Repeatability of the geometric distortion measurements was demonstrated, although with some sensitivity to phantom setup errors (Wyatt et al., 2018).

The results presented in **Paper I** showed a mean MRI-system-specific geometric distortion of 1.97 mm (maximum 7.86 mm) for the radial distance interval 200-250 mm from the isocenter. The mean value was thus in line with the recommendation of 2 mm (Walker et al., 2015, Weygand et al., 2016). The mean value for the radial distance interval 150-200 mm was 0.57 mm, and the maximum 1.85 mm. These values are similar to those found in other studies using an identical pulse sequence (Torfeh et al., 2015). The rapid change in geometric accuracy with increasing radial distance was expected due to the non-linearity of the MRI system's spatial-encoding gradients (Torfeh et al., 2015, Weygand et al., 2016).

As described in **Paper I**, the geometry distortion map was applied to a number of delineated radiotherapy structures to assess the geometric impact, using CT as reference. The estimated mean geometric volume deviation ratio for each of the structures CTV, PTV, femoral heads, bladder and rectum, compared to undistorted CT images, was  $1.00 \pm 0.00$  (1 SD). The corresponding value for the body structure was  $1.01 \pm 0.00$  (1 SD).

The mean magnitude of the geometric distortion of each of the structures CTV, PTV, femoral heads, bladder and rectum, measured in **Paper I**, was estimated to be  $0.00 \pm 0.00$  (1 SD) mm in the left-right direction and  $0.01 \pm 0.00$  (1 SD) mm in the anterior-posterior direction. The geometric distortion for the body structure was greater, as expected:  $0.13 \pm 0.04$  (1 SD) mm,  $0.09 \pm 0.05$  (1 SD) mm and  $0.44 \pm 0.09$  (1 SD) mm in the left-right, anterior-posterior and inferior-superior directions.

In the absence of volume deviation and geometric distortion of delineated radiotherapy structures, it could be concluded that the spatial integrity was intact. The methods used to reduce the effects of system-specific geometric distortion therefore seemed to be adequate for the purpose in question.

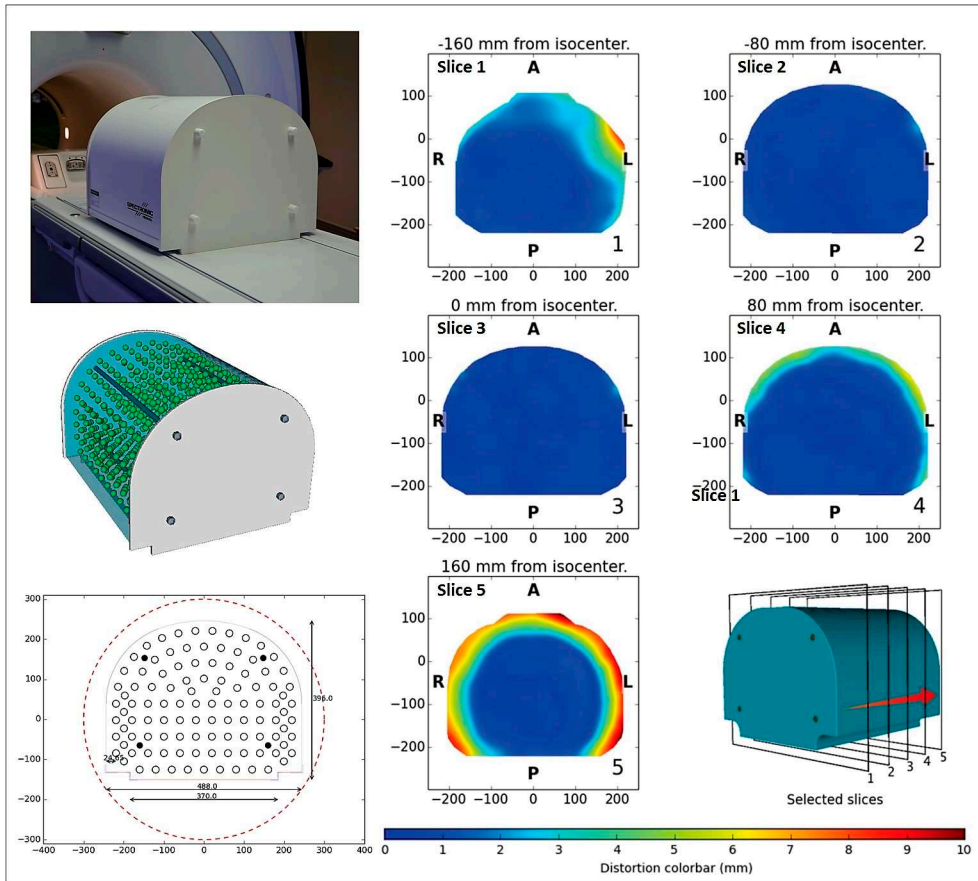


**Figure 9. Large-volume phantom and geometric distortion field**

The GRADE phantom (Spectronic Medical AB) was used to assess geometric distortion in a large scan volume. The phantom is shown on the left, together with the corresponding digital reference model and schematics of the spherical marker locations in the phantom. Dimensions in the reference model are given in mm. A 3D distortion field map over the phantom volume can be calculated from the measured positions of the markers and the positions of the markers in the digital reference model. (Copyright (2018) Spectronic Medical AB and Christian Jamtheim Gustafsson.)

### 3.4. Patient- and object-induced geometric distortion

Patient-/object-specific distortion can have two origins: variations in magnetic susceptibility and chemical shifts (Bellon et al., 1986, Bakker et al., 1992, Weygang et al., 2016). The magnitude of these geometric distortions is dependent on the MRI acquisition sequence used (Hood et al., 1999, Baldwin et al., 2009).

### 3.4.1. Magnetic susceptibility

When a patient or an object is placed in the MRI system it will interact with the main static magnetic field, creating magnetic field inhomogeneities inside and outside the patient. This leads to patient-/object-specific geometric distortion (Fransson et al., 2001). The change in  $B_0$  is dependent on magnetic susceptibility, which is a quantitative measure of the tendency of a material to interact with and distort an applied magnetic field (Schenck, 1996).

The induced geometric distortion is proportional to the field strength of  $B_0$  and the echo time, and is linearly dependent on the difference in magnetic susceptibility between adjacent materials or tissues (Bakker et al., 1992, Schenck, 1996, Baldwin et al., 2007). For the phantom experiment described in **Paper I**, the interface of interest, with a potential difference in magnetic susceptibility, is that between the spherical signal markers and the surrounding extruded polystyrene foam grid.

It should be noted that magnetic susceptibility effects are not always undesirable. The large difference in magnetic susceptibility between gold and prostatic tissue can be exploited to an advantage, by measurements with multiple echo times, for gold fiducial marker detection (**Papers III and IV**).

### 3.4.2. Reduction of patient- and object-induced distortion

The inhomogeneities induced in the static magnetic field and the patient-/object-specific geometric distortion can be reduced by magnetic field shimming (Adjeiwaah et al., 2019), decreasing echo time (Schenck, 1996), and using a high acquisition bandwidth (Bakker et al., 1992, Baldwin et al., 2007, Glide-Hurst et al., 2018).

### 3.4.3. Measurement of patient- and object-induced distortion

To investigate whether the phantom described in **Paper I** could have affected the assessment of the MRI-system-induced distortion, the combined impact of geometric distortion arising from the phantom and inhomogeneities in  $B_0$  was measured. This was done by acquiring a magnetic field map from an acquisition sequence called IDEAL IQ, provided by GE Healthcare (Yu et al., 2007).

IDEAL IQ is primarily used for *in vivo* fat quantification, and automatically corrects for deviations in the magnetic field by acquiring a magnetic field map, defined in frequency offset (Hz). This field map was exported and used to estimate the maximum magnitude of geometric distortion by assuming the distortion to be proportional to the magnitude of the deviations in the magnetic field, and inversely proportional to the read-out gradient strength (Bakker et al., 1992, Schenck, 1996, Baldwin et al., 2007).



The mean magnitude was calculated and found to be  $< 0.5$  mm for radial distances of  $< 250$  mm in the phantom, which was considered negligible. It should be noted that this included the effects of inhomogeneities in  $B_0$ . The geometric distortion originating solely from the phantom was therefore overestimated.

Patient-specific geometric distortion in MRI images of the male pelvis was recently investigated using a computer simulation method (Lundman et al., 2017) (Figure 10) for a 3 T MRI system by Adjeiwaah et al. (2018). A mean geometric distortion of the target and OAR of  $< 0.5$  mm was found using an acquisition bandwidth of 488 Hz/pixel, but greater geometric distortion was observed at lower acquisition bandwidths (Adjeiwaah et al., 2018).

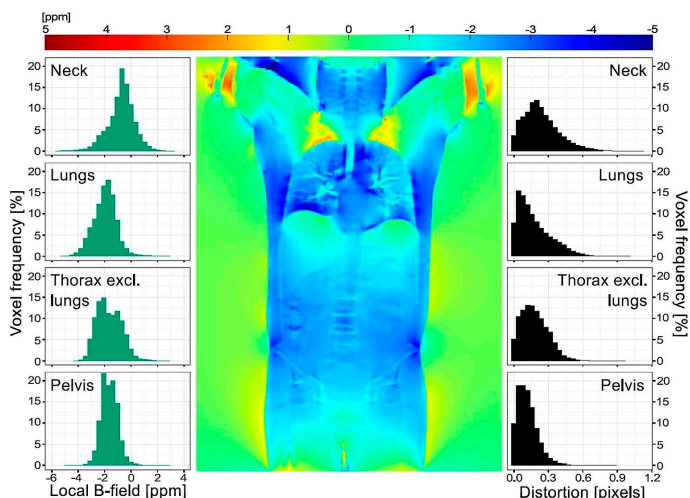


**Figure 10. Patient-induced geometric distortion**

The expected geometric distortion due to differences in magnetic susceptibility in the various tissues of a patient, calculated with computer simulations. As expected, patient-induced distortion is small in the pelvic area. Information from such simulations can be used to identify a sufficiently high acquisition bandwidth to reduce patient-induced susceptibility distortion to an acceptable level. (Image reprinted with permission from J.A. Lundman et al., *Physics and Imaging in Radiation Oncology* (2017), 1, 41-45. Copyright (2017) J.A. Lundman.)

In another study in which a high acquisition bandwidth was used, susceptibility distortion in the prostate was found to be  $< 0.1$  mm for 99% of all the voxels (Emmerich et al., 2018). The combined effect of  $B_0$  inhomogeneity and patient-induced susceptibility distortion has also recently been quantified in the male pelvis, specifically for the purpose of MRI-only RTP (Glide-Hurst et al., 2018). The result of that study showed geometric distortion to be very small and subject-dependent.

In the present work (**Papers I and II**) a high acquisition bandwidth of 390 Hz/pixel was used, and patient-induced susceptibility effects were therefore expected to be negligible. From the studies described above, it was concluded that geometric distortion arising from patient-induced susceptibility does not seem to constitute a problem when a high acquisition bandwidth is used in an MRI-only workflow for prostate radiotherapy. Patient-specific geometric distortion was not assessed in the present work.



## 4. Synthetic CT in MRI-Only Workflows

In a conventional CT-based radiotherapy workflow, CT images are used to calculate the absorbed dose (IAEA, 2016). For absorbed dose calculations in an MRI-only workflow, the corresponding information on tissue properties must be extracted from MRI data (Figure 11). The signal generated in MRI images is mainly dependent on the proton density and magnetic relaxation times of the tissue (McRobbie, 2007). The image contrast and image intensity in MRI images are thus not directly related to HU or electron density (Lambert et al., 2011, Korhonen et al., 2014a, Siversson et al., 2015). Therefore, synthetic CT images must be generated to provide maps with HU tissue information, i.e., sCT images.

Due to the possibility of geometric distortion in MRI images, concern has been expressed over the geometric accuracy, and thus the dosimetric accuracy in sCT images. For example, Korhonen et al. (2014a) noted that a “1 cm error in patient body contour can introduce approximately a 3% dosimetric discrepancy for a single 6 MV beam”. They also stated that the estimated difference in dose using an sCT image compared to a CT image would be < 1% with body contour shifts of a few millimeters when using multifield volumetric modulated arc therapy (VMAT) treatment plans (Korhonen et al., 2014a). The effects of different types of geometric distortion in sCT images with VMAT planning have been investigated by Palmer et al. (2018), who found that modifying the patient body contour by  $\pm 10$  mm led to a 3-4% difference in mean dose to the PTV, compared to that obtained using CT images, for one patient.

The dosimetric accuracy when using sCT images for prostate RTP has attracted considerable interest during recent years, and several sCT generation techniques have been investigated and evaluated. For more detailed information the reader is referred to recent reviews on synthetic CT generation by Edmund and Nyholm (2017) and Johnstone et al. (2018). It can be concluded that the dosimetric accuracy of several sCT generation methods for prostate RTP are reported to be below 1% for the mean target dose (compared to conventional CT-based RTP). This is regarded as adequate, as the dosimetric uncertainty, assessed in the complete radiotherapy process in a modern setting, is recommended to be within 3% (Thwaites, 2013).

The corresponding figure for the geometric uncertainty is 2-4 mm (Thwaites, 2013). To achieve this, the uncertainty in any individual component in the radiotherapy chain must be of the order of 1% or 1 mm (Thwaites, 2013).

Korsholm et al. (2014) stated that the PTV dose calculated with MRI-only RTP should be within 2% of that calculated based on CT. In this estimate, the dose calculation based on CT was estimated to have an uncertainty of 1% (Korsholm et al., 2014). A deviation between sCT- and CT-based dose calculations of 1% or less is small compared to the total estimated overall dosimetric uncertainty of 5%-10% for EBRT (IAEA, 2016).

Several confounding factors are responsible for dosimetric accuracy regarding sCT generation and some of them may be of systematic nature (Maspero et al., 2017a). The need for improved QC tools to investigate the individual components contributing to dosimetric deviations is evident, as these components otherwise could lead to systematic dose planning and treatment delivery errors (van Herk et al., 2000, van Herk, 2004).

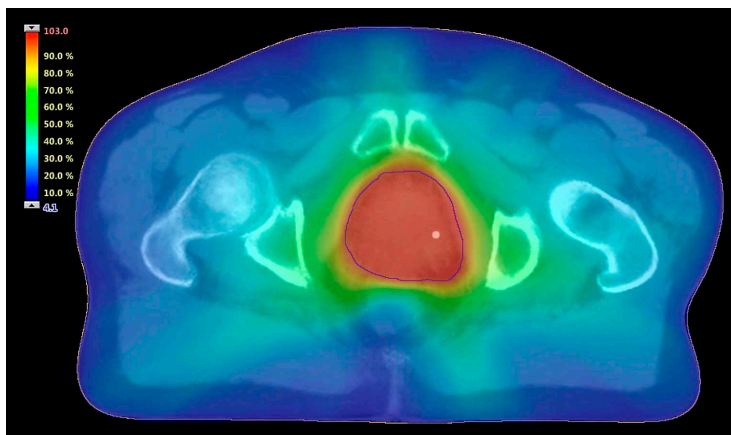


**Figure 11. A synthetic CT image showing the dose distribution**

Dose distribution for a prostate cancer patient, calculated using synthetic CT images (MriPlanner, Spectronic Medical AB) and VMAT treatment planning. The delineation around the prostate defines the PTV, receiving a total prescribed dose of 78 Gy, represented by 100% on the color scale. The round high-intensity object in the prostate is a representation of a fiducial marker.

## 4.1. Synthetic CT generation

Techniques for synthetic CT generation have been divided into different categories. In the review by Edmund and Nyholm (2017), three major categories are identified: main voxel, atlas, and hybrid methods. In a review by Johnstone et al. (2018), the methods are categorized as: bulk density override, atlas-based and voxel-based, with an additional hybrid category consisting of the combination of atlas- and voxel-based techniques. The categorization suggested by Johnstone et al. (2018) will be used in this thesis.

In bulk density methods, specific densities are assigned to segments of the patient volume. The simplest approach is to assign a homogeneous density (water equivalent electron density) to the whole volume. This has been reported to lead to dose discrepancies to the prostate target  $> 2\%$  compared to the CT-based dose distribution (Johnstone et al., 2018). This is seldom used in clinical applications as there is no bony anatomy, making it difficult to obtain DDR images for patient positioning. Bulk density methods with a heterogeneous density distribution have been investigated where, for example, soft tissue, bone, and air are assigned different densities. The discrepancies in dose to the prostate target have been reported to be  $< 2\%$ . This is an improvement compared to the assumption of homogeneous bulk density, likely due to the segmentation of the bony anatomy (Eilertsen et al., 2008). The need for manual bone segmentation in bulk density methods limits their clinical implementation (Lambert et al., 2011, Tyagi et al., 2017b).

Atlas-based methods rely on a reference material consisting of CT images and MRI images. The input MRI image can be matched to the reference image material where deformable registration can be applied to the reference material to create the best fitting CT-representation of the input MRI image (Dowling et al., 2012, Edmund and Nyholm, 2017). Due to limitations of deformable image registration, atypical patients may not be optimally represented in the atlas reference material which could lead to poorer accuracy (Tyagi et al., 2017b).

In voxel-based methods, voxel values for different tissues in single, or several types of MRI images are analyzed and used to create models for sCT generation (Korhonen et al., 2014a). sCT generation for patients with atypical anatomy is in general not regarded as problematic using voxel-based methods (Johnstone et al., 2018).

Several studies on atlas-based and voxel-based methods have reported dose discrepancies of  $< 1\%$  to the prostate target, and these methods have thus been identified as the most clinically useful (Tyagi et al., 2017b, Arabi et al., 2018, Johnstone et al., 2018). These methods allow for accurate dose calculations and patient positioning, without the requirement for manual bone segmentation.

Atlas-based and voxel-based methods are therefore used in commercial sCT generation solutions, such as Philips MRCAT (Helle et al., 2014, Schadewaldt et al., 2014, Köhler et al., 2015) and MriPlanner (Spectronic Medical AB, Helsingborg, Sweden). Advanced machine learning methods based on deep learning convolutional neural networks have also been introduced. Using such methods, sCT images can be generated for prostate RTP within a few seconds, with a mean dosimetric accuracy of about 1% to the prostate target (Arabi et al., 2018, Chen et al., 2018, Maspero et al., 2018a).

The method of sCT generation proposed by Siversson et al. (2015), was used in the present work, and was evaluated in the study presented in **Paper II**. The method relies on an algorithm called the statistical decomposition algorithm, which enables the generation of sCT images from a single large FOV T2w MRI image volume (Figure 12). It performs automatic tissue classification of the prostate, bladder, colon, bone, and fat for the T2w image input. Tissue classification is then combined with information from a model, trained using registered template material from both CT and MRI. The template material, which consisted of image data from 15 patients, allows the algorithm to estimate the most probable CT image representation of the MRI T2w input image, assuming the MRI image contrast is similar in the template material and the patient MRI image.

Ten patients were included in the study by Siversson et al. (2015), and the difference in mean absorbed dose to the prostate target between sCT and deformably registered CT was reported to be  $0.0 \pm 0.2\%$  (1 SD). As the observed dosimetric uncertainties were negligible, they concluded that the proposed method could provide an accurate MRI-only prostate radiotherapy workflow.

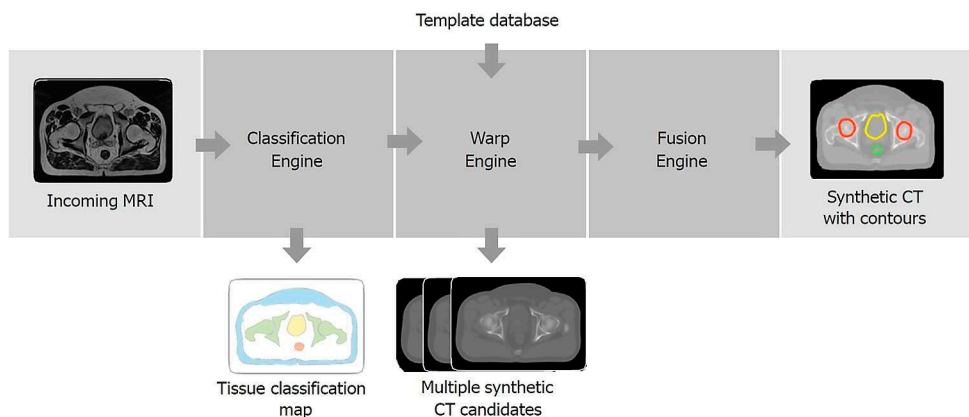


**Figure 12. Synthetic CT generation method**

Overview of synthetic CT generation using the statistical decomposition algorithm. The method was evaluated in the study presented in **Paper II**, and is explained by Siversson et al. (2015). (Copyright (2018) Spectronic Medical AB)

## 4.2. MRI acquisition sequence development

In parallel with the development of the method to assess the MRI-system-related geometric distortion, described in **Paper I**, an MRI acquisition sequence intended for sCT generation (**Paper II**) was investigated and adapted (the sequence parameters are given in Table 1). The acquisition sequence used in **Paper I** was the same as in Table 1, except that a FOV of 403 mm was used in the phase-encoding direction (rather than 314 mm), and the coverage in the slice direction was 200 slices rather than 88 slices to ensure that the whole phantom volume was covered. For the phantom measurements described in **Paper I**, the MRI system's built-in receiver body coil was used. The parameters given in Table 1 were chosen with different objectives in mind regarding sCT generation and the use of sCT images for prostate radiotherapy. Some of the more important acquisition parameters are described in the section below.

### 4.2.1. Patient setup and acquisition parameters

To enable the largest possible coverage of the patient, and to avoid deformation of the patient's body surface, a large receiver coil (16 channel GEM Anterior Array) was placed on coil bridges (Figure 13). MRI imaging with T2w image contrast was chosen, as this was preferred for the sCT generation technique of interest (Siversson et al., 2015), and is recommended for prostate target visualization (Barentsz et al., 2012).



**Figure 13. Patient setup for MRI scanning**

Typical patient setup for prostate radiotherapy imaging at Skåne University Hospital in Lund, Sweden. The patient (thesis author) lies on a flat surface and is held in place by ankle- (a) and knee positioning devices (b), both placed on a flat table top (c). To avoid deformation of the patient surface anatomy, the MRI receiver coil (h) is placed on coil bridges (d), whose height can be adjusted by turning an adjustment screw (e). A smaller distance between the patient and the receiver coil results in a higher MRI signal and thus an increase in the image signal-to-noise ratio. The patient's arms rest on the chest with the hands loosely holding a non-conducting rubber ring (f), and the head is resting on a support (i). To prevent excessive patient heating and the risk of skin burns, soft thin padding material is inserted between exposed areas of the patient and the receiver coil (g).

The MRI acquisition sequence was based on FSE with multiple refocusing radio frequency pulses for faster k-space sampling. FSE is one of the most commonly used MRI acquisition sequences in diagnostic radiology. Compared to gradient echo (GRE) acquisition sequences, spin-echo-based acquisition sequences are less sensitive to induced adverse susceptibility artifacts, due to the use of refocusing radio frequency pulses (Schenck, 1996).

Axial slice orientation was the preferred image orientation for prostate target delineation. The phase-encoding direction was defined as the anterior-posterior direction, i.e., the shortest anatomical direction, to minimize scan time as the acquisition sequence was 2D based (McRobbie, 2007). The inferior-superior coverage of 88 slices generated a coverage of 220 mm, which was regarded sufficient for anatomical coverage and dose calculations.

The FOV was defined to cover the patient's pelvic body contour. The left-right coverage was restricted to 448 mm to avoid the volume where the geometric distortion from the spatial encoding gradients was expected to be large (see Section 3.3). The acquisition matrix of 640 pixels in the frequency-encoding direction and 512 pixels in the phase-encoding direction afforded high spatial resolution, allowing for target delineation directly in the image, and thereby directly in the sCT image geometry. The high spatial resolution also enabled visualization of small signal voids from gold fiducial markers (Figure 5). Gold fiducial marker identification can thus be performed directly in the sCT image geometry, with the aid of a supporting MRI acquisition sequence, further explained in **Paper III** and Section 5.3.

To reduce geometric distortion from non-linear encoding gradients, vendor-based 3D distortion correction was applied using GradWarp (GE Healthcare) (Glover GH, 1986). The acquisition bandwidth was set to 390 Hz/pixel to minimize geometric distortion from patient magnetic susceptibility, gold fiducial marker susceptibility, and chemical shift, while maintaining a sufficient image signal-to-noise ratio. For a detailed discussion on the effects of acquisition bandwidth in MRI-only RTP for prostate, the reader is referred to Adjeiwaah et al. (2018).



**Table 1. MRI acquisition sequence parameters for sCT generation**

Large field of view MRI acquisition sequence parameters used for the patients included in the MR-Only Prostate External Radiotherapy (MR-OPERA) study at Skåne University Hospital, described in **Paper II**.

| Parameter  | Description / value                     |
|--|---|
| MRI system   | GE Discovery 750w 3.0T                  |
| Coil   | GE 3.0T GEM Anterior Array              |
| Acquisition sequence   | 2D fast recovery fast spin-echo         |
| Image contrast   | T2-weighted                             |
| Scan plane   | Axial                                   |
| Frequency-encoding direction                                 | Right-Left                              |
| Phase-encoding direction                                     | Anterior-Posterior                      |
| Field of view (frequency-encoding direction) (mm)            | 448                                     |
| Field of view (phase-encoding direction) (mm)                | 314                                     |
| Matrix size (frequency-encoding direction)                   | 640                                     |
| Matrix size (phase-encoding direction)                       | 512                                     |
| Scan pixel size (frequency-encoding direction) (mm)          | 0.7                                     |
| Scan pixel size (phase-encoding direction) (mm)              | 0.61                                    |
| Reconstructed pixel size (frequency-encoding direction) (mm) | 0.44                                    |
| Reconstructed pixel size (phase-encoding direction) (mm)     | 0.44                                    |
| Acquisition bandwidth per pixel (Hz)                         | 390                                     |
| Acquisition time (min)                                       | 07:00                                   |
| Slice thickness (mm)   | 2.5                                     |
| Interslice gap (mm)  | 0                                       |
| Repetition time (ms)   | 15000                                   |
| Number of slices   | 88                                      |
| Effective echo time (ms)                                     | 96                                      |
| Refocusing flip angle (°)                                    | 130                                     |
| Echo train length  | 15                                      |
| Number of acquisitions                                       | 1                                       |
| Number of averages   | 1                                       |
| Number of echoes   | 1                                       |
| Intensity correction   | Yes (surface coil intensity correction) |
| Intensity filter   | None                                    |
| 3D geometry correction                                       | Yes                                     |
| Shimming   | Yes (Auto, first order)                 |
| Flow compensation direction                                  | Slice direction                         |
| Radio frequency transmit mode                                | Multi-transmit                          |

### 4.3. Dosimetric impact from geometric distortions

To simulate the dosimetric effect of induced geometric distortion in MRI images for sCT generation, a 3D geometric distortion field was applied to conventional CT images for 10 patients (**Paper I**). As described in Section 3.3.4, the distortion field was measured using an MRI acquisition sequence intended for sCT generation, see Section 4.2 for MRI acquisition details.

The method described in **Paper I** enabled the separation of dosimetric errors resulting only from MRI-system-specific geometric distortion. Dosimetric errors originating from sCT generation could thus be avoided. The planned dose distributions based on original CT images and on geometrically distorted CT images for the same patients, in the same geometry, were compared (Figure 14 and Figure 16C).

The effect of potential geometric distortion on OAR and target delineation was also assessed by applying the geometric distortion field to the delineated structures in patient CT images. The results regarding geometric distortion have been presented and discussed in Section 3.3.4. It can be seen from Figure 14 that the mean percentage difference in dose for all isodose level bins was  $\leq 0.02\%$ , which is clinically negligible.

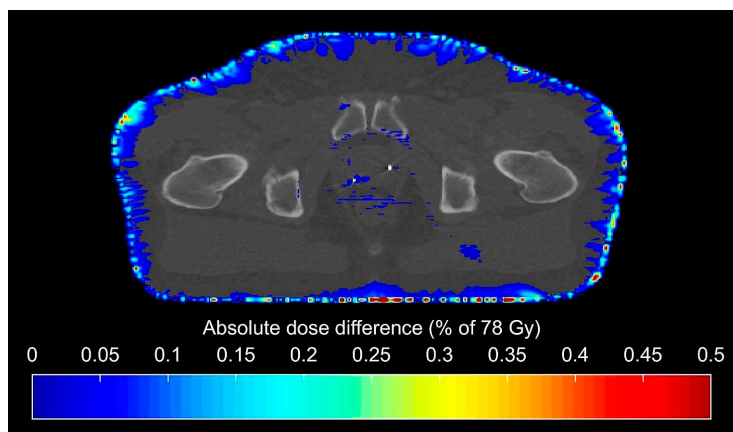


**Figure 14. Difference in absorbed dose resulting from geometric distortion**

The estimated absolute difference in absorbed dose resulting from geometric distortion in the MRI system (expressed as a % of the total prescribed dose of 78 Gy), in an MRI-only workflow. The difference in dose distribution is overlaid on a patient CT image, acquired in the study described in **Paper I**, where the CT images were geometrically distorted to simulate the effects of geometric distortion from an MRI system. The CT image was defined as the reference geometry in **Paper I**, and is therefore also used in this figure. The two high-intensity objects in the prostate are implanted gold fiducial markers. Absolute dose differences  $< 0.02\%$  have been omitted in the dose difference overlay for improved anatomical orientation. As MRI system geometric distortion is more pronounced at greater radial distances, the largest dosimetric differences are seen in the peripheral parts of the patient. These dose differences are, however, considered clinically negligible.

In conclusion, the method described in **Paper I** was able to quantify the dosimetric effect in an MRI-only prostate radiotherapy workflow, originating solely from MRI-system-specific geometric distortion.

In a study by Maspero et al. (2017a), regarding confounding factors for dose difference between CT and sCT for prostate RTP, the largest confounding factor was found to be the difference in CT and sCT calibration curves (0.7%). The dosimetric impact of differences in patient positioning between CT and MRI examinations, together with geometric distortion, was also investigated, by assigning a homogeneous bulk density (water) to both CT images and sCT images. The only difference between the CT images and the sCT images, was thus the extent of the body contour. The mean dosimetric difference for the CTV was reported to be  $0.01 \pm 0.35\%$  (1 SD) (Maspero et al., 2017a). These results are similar to the results presented in **Paper I**, where the largest absolute mean percentage dose difference in the prostate PTV was found to be  $0.02 \pm 0.25\%$  (1 SD). Dose deviations in photon treatments, resulting from geometric uncertainties in the peripheral parts of the patient, therefore seem to be of little importance, as demonstrated in **Paper I**.

A study has recently been published in which very similar techniques to those described in **Paper I** were used to assess the MRI-system-specific distortion and to geometrically distort CT images for a variety of treatment locations (Yan et al., 2018). It was concluded that distortion in the MRI images did not reach clinically important levels in most of the cases investigated.

Sun et al. (2015a) performed an end-to-end test on geometric and dosimetric aspects of MRI-only prostate RTP using a geometric phantom. They found a mean geometric distortion for all structures (excluding the body) to be  $< 1$  mm. A dose difference of 0.1% was reported for the prostate PTV, while no difference was observed in the prostate CTV. These results are consistent with the results given in **Paper I**.

The dosimetric impact in the prostate of patient-induced magnetic susceptibility distortion has also been assessed using simulations, and the mean percentage dose difference using a high acquisition bandwidth was reported to be  $0.16 \pm 0.13\%$  (1 SD) at the isocenter, which can be regarded as small (Adjeiwaah et al., 2018).

To conclude, the dosimetric impact of different sources of geometric distortion can be separated and assessed in MRI-only prostate RTP. MRI-system- and patient-related geometric distortion can be reduced using appropriate MRI acquisition protocols such that differences in dose are negligible.

## 4.4. Clinical synthetic CT validation

**Paper II** describes a multicenter/multivendor study in which sCT images were created to validate the dosimetric accuracy and clinical robustness of a commercially available sCT generation technique for prostate RTP. Four different radiotherapy clinics in Sweden participated in this study, with a total of four different MRI systems. The study is referred to as the MR-Only Prostate External Radiotherapy (MR-OPERA) study.

T2w MRI images with a large FOV were acquired using dedicated MRI acquisition sequences for sCT generation. A total of 170 prostate cancer patients were included in the study, and all clinics used a flat table top and patient immobilization with ankle and knee positioning devices. The patients included at Skåne University Hospital, Lund, Sweden, were scanned with the MRI acquisition sequence described in Section 4.2 and Table 1. The geometric accuracy of this MRI acquisition sequence had already been validated (**Paper I**, see Section 3.3). Table 2 in **Paper II** gives the MRI acquisition sequence parameters used at all the centers participating in the MR-OPERA study, which were similar to the parameters given in **Paper I**.

A CT treatment plan was created according to the local practice at each clinic. Two different vendors of treatment planning systems and multiple treatment techniques were used together with two different algorithms for dose calculation. After creation of the treatment plan, the sCT image was rigidly registered to the CT image, and the treatment plan was copied to the sCT image. The dose was recalculated with an identical beam setup and equal number of monitor units. The two dose distributions, originating from CT and sCT, were analyzed using gamma evaluation (Low et al., 1998) and dose volume histogram (DVH) parameters. The DVH parameters used were adopted from the conventional arm of the Swedish multicenter phase 3 study HYPOfractionated RadioTherapy of intermediate risk localised Prostate Cancer (Widmark, 2008).

The overall mean difference in dose between dose distributions originating from sCT and CT were below 0.3% for all organs and the target. The maximum mean difference in dose for all patients ranged between -1.15% and 1.42%, and similar results were obtained at the four clinics (Figure 15). The results for all centers were within a 1% mean dose deviation for all organs and the target. This was expected as several studies on atlas-based and voxel-based sCT generation methods have reported dose discrepancies of < 1% (Johnstone et al., 2018).

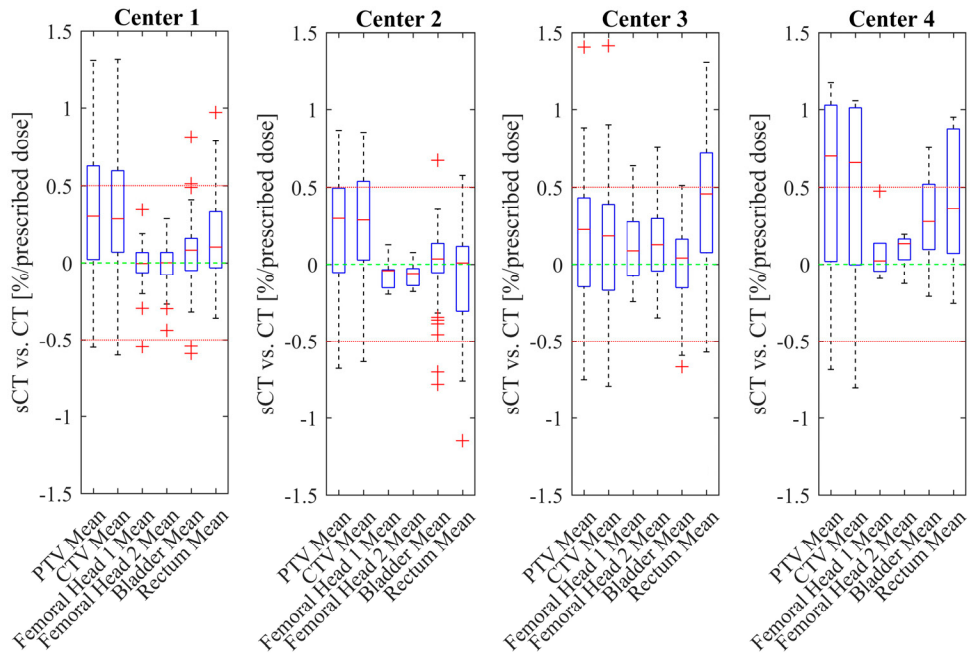


**Figure 15. Dose differences in the MR-OPERA study**

Differences in mean doses between sCT and CT in PTV, CTV, femoral head, bladder and rectum, given in boxplots for the four centers (sCT-CT, expresses as % of the total prescribed dose). The horizontal line in each box indicates the median value. The lower and upper box edges indicate the 25th ( $q_1$ ) and 75th percentiles ( $q_3$ ) of the sample data, respectively. The whiskers extend to the most extreme data points not considered outliers. A point was considered an outlier if it was greater than  $q_3 + W \times (q_3 - q_1)$  or less than  $q_1 - W \times (q_3 - q_1)$ , where  $W$  was set to 1.5. The number of patients examined at centers 1, 2, 3 and 4 was 68, 54, 42 and 6, respectively. All centers showed similar results, with a positive systematic dose difference.

A systematic positive dose deviation was found at all centers (Figure 15). Outliers with a dose difference of about 1.5% were identified in patients with a large difference in outer body contour between sCT and CT. The systematic difference in dose was hypothesized to be an effect of the longer examination time for MRI scanning than for CT scanning, leading to patient relaxation. The MRI image, and thus the sCT image, was found to be smaller in the anterior-posterior direction and larger in the left-right direction, than in the CT image. As the dose difference was calculated as sCT-CT dose distribution this could explain the systematic positive dose deviation.

The sCT body contour was adjusted to match the body contour of the corresponding CT image in a subset of 28 patients from center 1 (Skåne University Hospital in Lund). The dose differences decreased, approaching zero, with decreasing standard deviations and maximum differences (Figure 16, A and B).

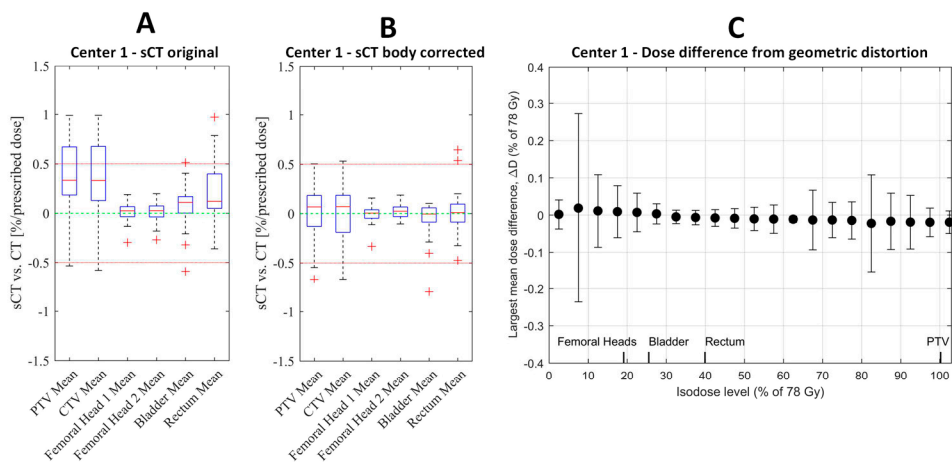


**Figure 16. Dosimetric impact of differences in patient positioning**

Dosimetric differences between sCT and CT for a subset of 28 patients from center 1 (Skåne University Hospital in Lund) in the MR-OPERA study, without (A) and with (B) correction for difference in body contour. (The boxplots are explained in Figure 15). The dosimetric difference is shown in A for multiple OAR and target structures. The difference in body contour between sCT and CT was corrected, and the results are given in B. The very small median dosimetric difference in B was similar to the largest estimated mean ( $\pm 1$  SD) dosimetric difference due to MRI-system-related geometric distortion in C (**Paper I**) ( $n=10$ ). This suggests that differences in patient positioning between CT and MRI examinations have a considerable impact on dosimetric sCT evaluations. All patients here were prescribed a total of 78 Gy to the prostate. (Figures adapted from **Papers I** and **II**.)

Comparison of the dosimetric results in **Papers I** and **II** is of interest (Figure 16). First, it is important to note the different factors that could have affected the dose deviations reported in **Paper II**. The results for the subset of 28 patients before body contour correction include the effects arising from different body contours between CT and MRI examinations (Figure 16A). These results also include potential effects originating from the sCT generation method, CT/sCT image registration, and remaining geometric distortion (after 3D distortion correction). After body contour correction, potential effects from the sCT generation method, CT/sCT image registration and non-peripheral geometric distortion remains (Figure 16B). The results given in **Paper I** contain only the estimated dosimetric difference resulting from geometric distortion after 3D distortion correction (Figure 16C).

As can be seen from Figure 16, the dose deviation after body contour correction is similar to that given in **Paper I**. This suggests that effects originating from the sCT generation method, CT/sCT image registration, and remaining geometric distortion are very small compared to the effects originating from differences in patient positioning between CT and MRI examinations. The considerable impact of patient positioning on the difference between sCT- and CT-calculated dose distributions should therefore always be taken into consideration.

The results obtained after body contour correction (**Paper II**) are in line with those given by Siversson et al. (2015), where the mean dose difference to the prostate PTV was reported to be  $0.0 \pm 0.2\%$  (1 SD) after non-rigid registration between the CT- and sCT images (body contour corrected). Furthermore, Dowling et al. (2012) and Lambert et al. (2011) reported that the dose differences between CT- and sCT images in their studies were mainly due to differences in body contours resulting from patient positioning differences.

Using 2%/2-mm global gamma criteria the gamma evaluation gave a mean pass rate of  $99.12 \pm 0.63\%$  (1 SD) in the complete body volume, and a mean pass rate of  $99.97 \pm 0.13\%$  (1 SD) in the PTV (**Paper II**). After body contour correction, the mean pass rate in the complete body was  $100.00 \pm 0.01\%$  (1 SD) and  $99.98 \pm 0.09\%$  (1 SD) in the PTV.

From the study presented in **Paper II**, it could be concluded that the sCT generation software MriPlanner, provided by Spectronic Medical, could be used in several clinics, using MRI systems from different vendors, with very small dosimetric differences compared to conventional CT dose calculation. The software showed robustness to differences in magnetic field strength, MRI equipment, and treatment techniques, and can therefore enable an MRI-only prostate radiotherapy workflow. CT- and sCT images were shown to be equivalent with respect to the DVH criteria used. The dosimetric differences reported in **Paper II** seem to be mainly the result of differences in patient body contour between CT and MRI examinations.





# 5. Fiducial Marker Identification in MRI-Only Workflows

Intraprostatic gold fiducial markers allow for high precision in treatment target positioning. These markers are easily identified in CT images due to their hyper-intense signal and the characteristic streak artefacts, surrounding the fiducial marker (Kassim et al., 2011, Chan et al., 2015). As there is no CT imaging in an MRI-only workflow, the fiducials must be identified using MRI images. No useful nuclear magnetic resonance signal is expected from gold (Zangger and Armitage, 1999), and gold fiducial markers will therefore appear as signal voids in MRI images. Other objects in the prostate, such as intraprostatic calcifications, vessels, post-biopsy fibrosis and hemorrhages, will be seen as hypo-intense objects in MRI images (Kapanen et al., 2013, Murphy et al., 2013, Ghose et al., 2016, Dinis Fernandes et al., 2017). Differentiation between gold fiducial markers and intraprostatic calcifications is therefore challenging, and identified as a serious limitation to successful MRI-only prostate radiotherapy (Maspero et al., 2017c, Tyagi et al., 2017a, Maspero et al., 2018b, Tenhunen et al., 2018). It is therefore important to develop, investigate, and validate manual and automatic methods of gold fiducial marker identification together with suitable QC measures.

## 5.1. Gold fiducial marker implantation

Gold fiducial markers are implanted in the prostate prior to radiotherapy treatment to indicate the position of the prostate (Scarborough and Fuller, 2006, O'Neill et al., 2016), see Section 1.3. This results in an improvement in the localization of the prostate target (Kupelian et al., 2005, Scarborough and Fuller, 2006, van der Heide et al., 2007). Gold fiducials can be visualized with a variety of imaging methodologies, such as mega voltage electronic portal imaging, kV X-ray imaging, and CBCT imaging, which all provide the position of the target (O'Neill et al., 2016). These imaging modalities rely on the attenuation of X-rays, and the high mass density of gold therefore enables good visualization. Gold is also considered biologically inert and biocompatible (Umair et al., 2016). The fiducials used for prostate radiotherapy are therefore made of gold, and are commercially available in different shapes and sizes (Ng et al., 2014, O'Neill et al., 2016).

The implantation of gold fiducial markers in the prostate is guided by transrectal ultrasound, and can be performed with transrectal or transperineal procedures (Moman et al., 2010). At Skåne University Hospital in Lund, three in-house-produced gold fiducial markers, with a length of 5 mm and diameter of 1 mm, are implanted by an oncologist in a 3D triangular arrangement. The procedure is performed transperineally, guided by a transrectal ultrasound, during which the patient is placed in a lithotomy position (Figure 17). The 3D arrangement of the markers enables assessment of the prostate location in all three spatial dimensions as it avoids marker overlap on orthogonal kV X-ray images (Schmidt and Payne, 2015). Depending on the size of the prostate, the 3D arrangement leads to internal fiducial distances of about 2-3 cm. Implantation of fiducials at Skåne University Hospital is performed two weeks prior to MRI imaging. An X-ray image is acquired at the end of the implantation procedure, using a mobile C-Arm X-ray system (Ziehm Vision FD Vario 3D, Ziehm Imaging, Germany) to verify successful implantation (Figure 17).

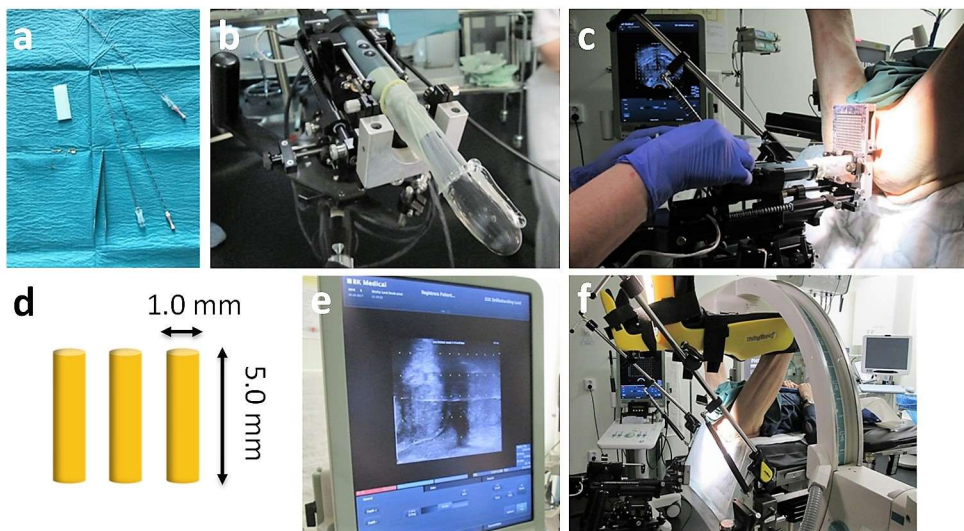


**Figure 17. Gold fiducial marker implantation**

Gold fiducial markers are implanted two weeks prior to MRI imaging. a) Three cylindrically shaped gold fiducial markers seen in d), are preloaded into long needles. b) A lubricated ultrasound probe on an adjustable mounting is used to provide visual guidance for the implantation procedure. c) The patient is placed in a lithotomy position, and the ultrasound probe is inserted through the rectum. A needle guide template is placed above the probe on the adjustable mounting. e) Ultrasound image information is used continuously to guide the operator while the needles are placed in the guide template and inserted into the prostate. When the needle tip has reached the desired location in the prostate, the gold fiducial marker is released from the long needle. Fiducials are placed in a 3D triangular arrangement. f) An X-ray image is acquired using a mobile C-Arm X-ray system for verification of successful implantation.

## 5.2. Prostatic calcifications

Prostatic calcifications can develop anywhere in the prostate, and have been reported to be more common in middle-aged and older patients with benign prostate hyperplasia, prostate cancer, or prostatitis (Cao et al., 2018). These calcifications are referred to medically as prostatic calculi or prostatic calculus, but the term prostatic stone(s) has also been used (Cao et al., 2018). The terms prostatic and intraprostatic calcifications are used in this thesis.

The mechanism behind the development of prostatic calcifications, and their relevance to benign or malignant findings in the prostate, have not yet been determined (Sfanos et al., 2009, O'Neill et al., 2016, Hyun, 2018). The prevalence of prostatic calcifications varies widely, from 7% to 89% (in patients aged 38-70 years), and it has been suggested that this could be explained by the lack of a standardized classification method (Cao et al., 2018, Hyun, 2018). The prevalence of intraprostatic calcifications  $\geq 2$  mm (FWHM) in all the patients included in the study described in **Paper III** (both training and validation data) was 65% (39/60). This is higher than the value of 35% (46/131) reported previously for intraprostatic calcifications  $> 2$  mm in diameter by Zeng et al. (2008).

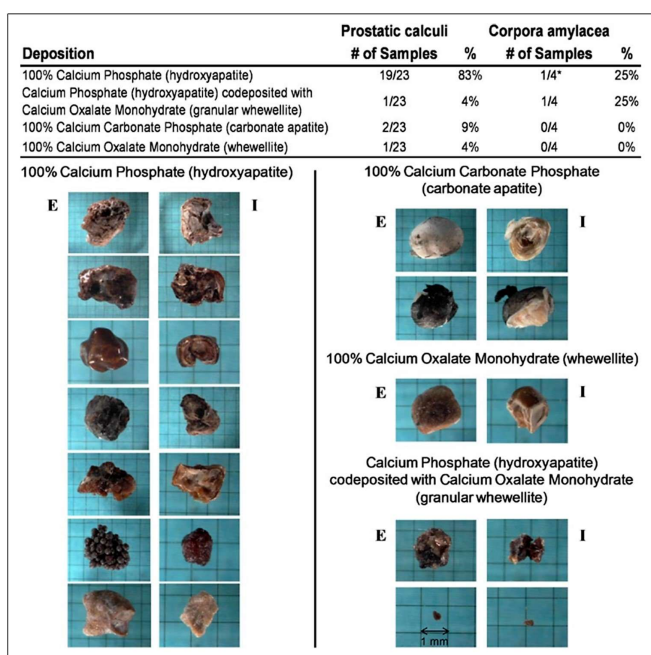


**Figure 18. Calcifications removed from prostate glands**

Intraprostatic calcifications (called prostatic calculi in this figure) can vary in size and shape, and consist mainly of calcium phosphate (see table at the top). Column E shows the exterior view and column I the interior of the calcifications. Note: the scale is 1 mm per square, as shown in the bottom right. (Image reprinted with permission from "Acute inflammatory proteins constitute the organic matrix of prostatic corpora amylacea and calculi in men with prostate cancer", K.S. Sfanos et al., Proc Natl Acad Sci U S A (2009), 106, 3443-8. Copyright (2009) PNAS.)

Prostatic calcifications consist mainly of calcium phosphate (> 80%), more specifically calcium hydroxyapatite (Sfanos et al., 2009) (Figure 18). The signal void originating from calcifications in MRI images has also been validated in phantom studies, using a pure form of calcium hydroxyapatite (Mustafi et al., 2015). The absence of signal explains why it is difficult to differentiate calcifications from gold fiducial markers, as gold also creates signal voids.

### 5.3. MRI methods for fiducial marker identification

The magnetic resonance signal around the gold fiducial marker will be degraded due to differences in the magnetic susceptibility between gold and the surrounding prostatic tissue (Schenck, 1996, Port and Pomper, 2000). The size and shape of the signal void are dependent on the shape and orientation of the gold fiducial marker, and the nature of the MRI acquisition sequence, together with chosen acquisition parameters (Schenck, 1996, Jonsson et al., 2012). For example, a transverse image slice (relative to the direction of  $B_0$ ) will depict the fiducial marker as a round signal void if the main axis of the cylindrically shaped fiducial is oriented parallel to  $B_0$  (Jonsson et al., 2012). This was the desired geometry for acquiring MRI images of the implanted fiducials in the study described in **Paper III**.

#### 5.3.1. MEGRE image characteristics

GRE acquisition sequences can be used to increase the image sensitivity to susceptibility effects, and improve visualization of the gold fiducial markers (Port and Pomper, 2000). The difference in magnetic susceptibility between the gold and the surrounding prostatic tissue can then be exploited for fiducial identification (Kapanen et al., 2013, Ghose et al., 2016, Dinis Fernandes et al., 2017, Maspero et al., 2018b).

A GRE MRI acquisition sequence that could be used to acquire data at multiple echo times (eight echoes, 2.38-23.6 ms, echo time difference of 3.03 ms) was developed and optimized (**Paper III**). This sequence is referred to as the multi-echo gradient echo (MEGRE) sequence, the main aim of which was gold fiducial marker identification.

The reconstructed MEGRE images consisted of acquired 2D slices of the prostate volume, where each slice was reconstructed with multiple echo times (Figure 19). The scan parameters can be found in Table 1 in **Paper III**. As a longer echo time allows for increased intravoxel spin dephasing, the size of the signal voids resulting from the gold fiducial markers increases with increasing echo time. The acquisition sequence was optimized to maximize the signal from the prostatic tissue, and to minimize the signal in the vicinity of the gold fiducial marker, at different echo times.

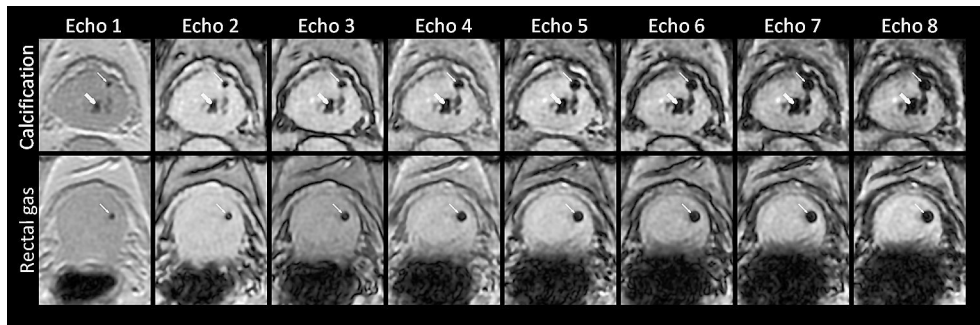


**Figure 19. MEGRE image characteristics**

MEGRE images were obtained using eight echo times, from 2.38 to 23.6 ms, for two different patients. The upper row shows an example of the difficult differentiation between a gold fiducial marker (thin arrow) and an intraprostatic calcification (thick arrow) in a patient with a calcification. The fiducial marker creates a round signal void that expands more rapidly with increasing echo time than the signal void from the calcification. The lower row shows the signal void from a fiducial marker and the presence of rectal gas below the prostate (the dark area). The area of the signal void resulting from rectal gas also expands with increasing echo time due to differences in magnetic susceptibility and perturbs the boundary of the prostate. The short echo times provide a means of avoiding or mitigating adverse susceptibility effects of rectal gas.

Information from MEGRE images using multiple echo times facilitates differentiation between objects such as intraprostatic calcifications and gold fiducial markers. This is possible as the signal void resulting from a gold fiducial marker in a transverse slice is round in shape. Furthermore, expansion of the signal void area with respect to echo time takes place more rapidly for the gold fiducial marker than for the calcifications, due to the higher magnetic susceptibility of the gold fiducial. Previous studies support these findings (Schenck, 1996, Port and Pomper, 2000, Olsrud et al., 2005). The visual effect can easily be recognized by the human eye, and is useful in the clinical setting where multiple echo times can be visualized by scrolling through the image data. Differentiation is further facilitated by the fact that the fiducial is visible in several slices as the length of the fiducial marker (5 mm) is about two times the image slice thickness (2.8 mm).

The use of multiple echo times can also help reduce problems in gold fiducial marker identification, which arise due to gas pockets in the rectum. This problem has been reported by Dinis Fernandes et al. (2017) when using a single echo balanced steady-state free precession acquisition sequence. A similar acquisition sequence has been used for fiducial identification by Tenhunen et al. (2018), Tyagi et al. (2017b), and Maspero et al. (2018b). In cases where air pockets, such as rectal gas exist, a single echo image can suffer from large image artefacts, perturbing the boundary of the prostate (Figure 19), making gold fiducial marker visualization more difficult or impossible. The problem associated with gas can be reduced or completely eliminated by using the shortest echo time in the MEGRE data (Figure 19).

### 5.3.2. Manual detection performance

In order to investigate the detection performance and clinical value of MEGRE images for gold fiducial marker identification, a manual observer study was performed involving three medical physicists and two MRI technologists. One of the medical physicists had seen the patient material six months prior to the study. One MRI technologist misunderstood the instructions given and was excluded from the study. Forty-four patients were included in the study, with a total of 129 gold fiducial markers. Prior to the study, the observers were instructed on how to use the MEGRE data for gold fiducial marker identification. (In **Paper III** it is erroneously stated that four patients were excluded from the manual observer study, due to image artifacts arising from large amounts of rectal gas, whereas in fact these four patients were only excluded from the dataset used in the automatic detection method, see Section 5.4.)

The observers were presented with small FOV transverse T2w images and transverse MEGRE images at the same time, side by side, using in-house developed MATLAB software with a graphical user interface (Figure 20). The MEGRE images were used to help the observers discriminate and identify the gold fiducial markers in the small FOV T2w images. The observers were asked to locate the center of mass of the gold fiducial markers in both image sets (small FOV T2w and MEGRE), at the same time, for each patient.

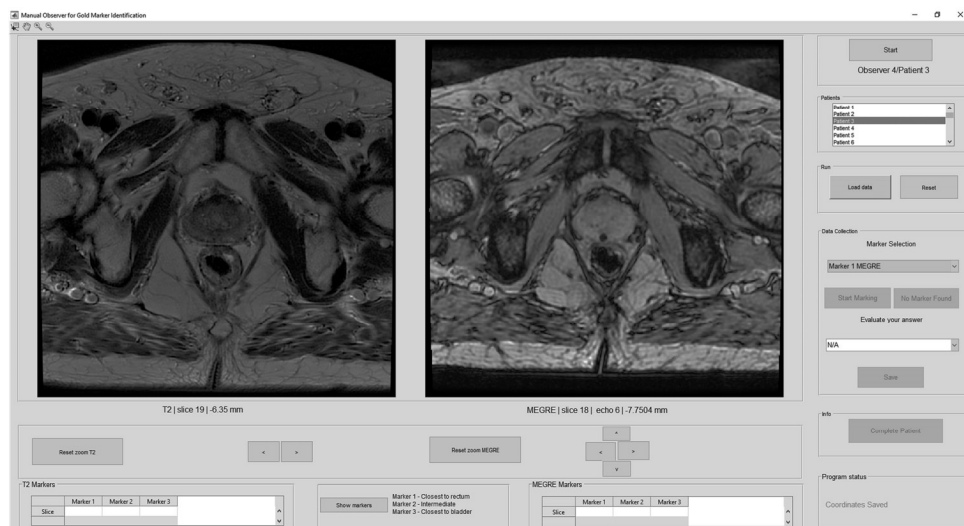


**Figure 20. Software for manual gold fiducial marker observer study**

Graphical user interface (GUI) used in the manual observer study for gold fiducial marker identification using MEGRE images. The observers were asked to locate the center of mass of the gold fiducial markers in both small FOV transverse T2w images (left) and transverse MEGRE images (right). The GUI allowed observers to zoom in and browse between image slices and echo times (arrows left/right and up/down). To help with spatial correlation between the different image types, slice position coordinates were displayed in the GUI below each slice, for both image types. The GUI did not enable the image types to be superimposed, blended or viewed in any other orientation.

The mean values and range of the observer sensitivity, specificity, and accuracy were calculated, giving values of 98 [97-100]%, 94 [92-100]% and 97 [96-100]%, respectively. To enable the calculation of these metrics, the number of true negative gold fiducial markers for each patient was set to one. The mean and range for the observer true positive rate (TPR) (defined as true positives/total number of gold fiducial markers in the study) were found to be 98 [97-100]%. The mean number of patients in which all gold fiducial markers were correctly identified was 41.5 out of 44, and the mean geometric accuracy was determined to be  $1.14 \pm 1.06$  (1 SD) [0.01-6.26] mm. These results reflect the manual observer performance exclusively in identifying the gold fiducial markers in a small FOV T2w image, using MEGRE images for support, and are published in **Paper III**. These results are thus dependent on both the small FOV T2w images and the MEGRE images.

The observers were also asked to identify the gold fiducial markers in the MEGRE images. Results regarding the detection performance in the MEGRE images have not been published previously. The mean values and range of observer sensitivity, specificity, and accuracy in the MEGRE images were 100 [99-100]%, 98 [96-100]%, and 99 [98-100]%, respectively. The mean and range in observer TPR were found to be 99.6 [99-100]%. The mean number of patients in which all gold fiducial markers were correctly identified was 43.5 out of 44, and the mean geometric accuracy was determined to be  $0.93 \pm 0.88$  (1 SD) [0.00-5.88] mm. These results are only dependent on the MEGRE images.

The results regarding fiducial marker detection were better in the MEGRE images than in the small FOV T2w image. This was mainly due to the challenge associated with locating the very small signal void from the gold fiducial marker in the small FOV T2w image, which was sometimes not visible at all. This problem could probably have been mitigated or eliminated by including image blending functionality in the graphical user interface, to enable visual guidance between the two image types. It is likely that the spatial correlation between the two image types, perceived by the observers, thereby would increase, and facilitate improved detection of small signal voids in the small FOV T2w image.

Several manual observation studies have been performed to assess the detection performance in gold fiducial marker identification. One or more MRI acquisition sequences have been used, and TPRs of 91%-98% and a mean geometric accuracy of 0.6 mm-0.9 mm have been reported (Kapanen et al., 2013, Ghose et al., 2016, Maspero et al., 2017c, Maspero et al., 2018b, Tenhunen et al., 2018, Pathmanathan et al., 2019). The results of these studies regarding geometric accuracy and TPR are similar to the results published in **Paper III**, regarding fiducial identification in the small FOV T2w image. Direct detection of gold fiducial markers in the MEGRE images showed a higher TPR, close to 100%.

## 5.4. Automatic fiducial marker identification

The main objectives of an MRI-only workflow are to reduce the number of imaging modalities needed for RTP, and thus the cost. It has been suggested that automated methods of gold fiducial marker detection save time and staff resources, and avoid interobserver differences (Ghose et al., 2016, Dinis Fernandes et al., 2017, Maspero et al., 2017c). The MEGRE images described above were also used as input in the development of an automatic method (Figure 21).

Existing MRI-only workflows described in the literature depend on separate MRI acquisition sequences for fiducial marker identification, target delineation, and sCT generation (Greer et al., 2011, Dowling et al., 2012, Tyagi et al., 2017a, Tenhunen et al., 2018). The use of multiple acquisition sequences is undesirable due to the risk of patient and organ motion between image acquisitions, and because they require image registration (Tyagi et al., 2017a, Tenhunen et al., 2018).

### 5.4.1. Development of an automatic detection method

To eliminate the problem of interscan patient motion, it would be preferable to identify the fiducials directly in the image geometry of interest, i.e. in the geometry where target delineation is performed. In the study described in **Paper III**, the fiducial markers were identified directly in the target delineation image geometry, i.e. the small FOV T2w image, in both the manual and automatic methods. The need for image registration was eliminated by identifying all possible fiducial candidate locations and then using the MEGRE images for selection and discrimination (Figure 21). The in-plane size of the signal voids in the small FOV T2w image are similar to the physical diameter of the fiducials (1 mm). The performance in detecting the gold fiducial markers directly in the MEGRE images was not assessed in the automatic method.

The useful features in the MEGRE images detectable with the human eye were the increase in the signal void area with increasing echo time, the circular shape of the signal voids, and the clearly visible signal voids at short echo times. These features were also exploited in the automatic digital image processing MATLAB code developed to automatically identify the gold fiducial markers.

Calculation of the signal void roundness and the expansion rate of the signal void area with increasing echo time was crucial in the automatic method. Both the identification and discrimination of gold fiducial markers were highly dependent on these metrics, thus relying on accurate image segmentation.



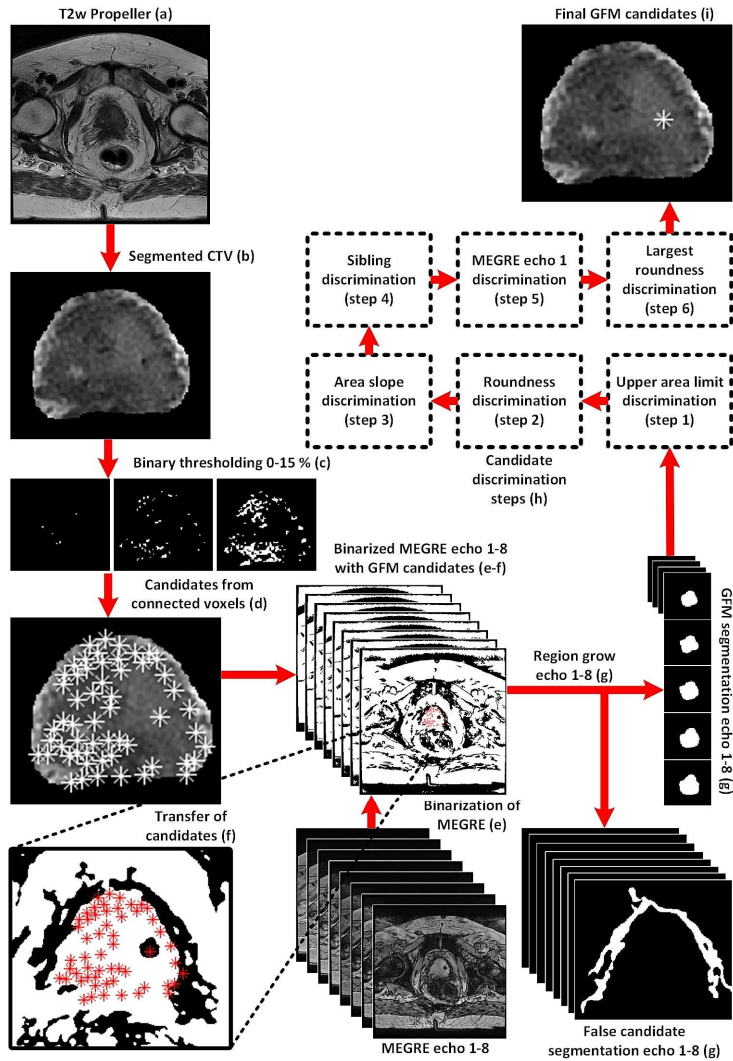


**Figure 21. Overview of the model developed for automatic fiducial detection**

A model was developed for automatic gold fiducial marker detection. a-b) Small FOV T2w image data were segmented using the CTV. c) Segmented data were binarized for multiple segmentation thresholds. d) Fiducial candidates were determined from connected binary voxels. e-f) MEGRE data were binarized and fiducial candidates transferred to corresponding locations in binarized MEGRE data. g) Locations of fiducial candidates in the binarized MEGRE images individually defined starting points for region growing segmentation, performed for all echo times. h) Fiducial candidate discrimination criteria were applied in a given order (steps 1-6) to determine the final gold fiducial marker candidates displayed in i). (Gold fiducial marker is abbreviated GFM in figure.)

#### 5.4.2. Automatic detection performance

The sensitivity, specificity, and accuracy of the automatic method were 84%, 74% and 81%, respectively. The TPR was found to be 84%. All three gold fiducial markers were correctly identified in 24/40 patients (=60%) and the geometric accuracy was determined to be  $1.28 \pm 1.25$  (1 SD) mm. The accuracy of 81% was inferior to the accuracy of 97% in the manual observer study. The specificity of 74% was also inferior. The inaccurate automatic segmentation of signal void areas was identified as the main problem, leading to errors in the calculation of the roundness and signal void area expansion rate, leading in turn to poorer identification and discrimination. To improve the automatic method, a prior knowledge model of the signal void volume should be implemented. Further, the current assessment of signal void area should be modified to assess the whole signal void volume instead.

The TPR of 84% for the automatic method was inferior to those of existing models described in the literature, where values of 84%-95% have been reported (Ghose et al., 2016, Dinis Fernandes et al., 2017, Maspero et al., 2017c). It should, however, be noted that none of the existing models identifies the gold fiducial marker directly in a target delineation image.

The automatic method developed here was applied to small FOV T2w images, but the principle could be adapted for use in large, high-quality FOV T2w images specifically for sCT generation. This could enable dose calculation, target delineation and gold fiducial marker identification to be performed in the same image geometry without the need for image registration, eliminating interscan differences. This concept has recently been explored in a manual manner with encouraging results (Persson et al., 2019).

### 5.5. Quality control of fiducial marker identification

The clinical implementation of MRI-only prostate radiotherapy requires safe and reliable procedures for gold fiducial marker identification. The performance of a new method should never be inferior to that of CT-based methods, and should ideally have a detection accuracy of 100%. No study described in the literature has yet reached this detection accuracy (Kapanen et al., 2013, Ghose et al., 2016, Dinis Fernandes et al., 2017, Maspero et al., 2017c, Maspero et al., 2018b, Tenhunen et al., 2018, Pathmanathan et al., 2019).

It is important to note that fiducial identification in CT images should not be regarded as a method with perfect geometric accuracy. A mean displacement of 0.7-2.17 mm has been reported, depending on the orientation of the fiducial during CT scanning (Owen et al., 2008). Slice thickness was identified as the major factor limiting the geometric accuracy in fiducial identification (Owen et al., 2008).

These findings are very similar to the observations made in the present work (**Paper III**), where the mean geometric accuracy was determined to be about 1 mm using MRI. This is also similar to the magnitude of fiducial migration (Ng et al., 2014, O'Neill et al., 2016) and differences in the distances between fiducial markers during the course of treatment (Castro et al., 2018).

In certain clinical implementations of MRI-only prostate radiotherapy, CT was still used for the identification of gold fiducial markers or to differentiate permanent brachytherapy seeds from fiducials (Tyagi et al., 2017a, Tenhunen et al., 2018). It has been suggested that the identification accuracy of fiducial markers could be increased by using multiple observers or a fourth fiducial marker (Maspero et al., 2018b). However, such measures would increase the cost. The development of improved and cost-effective gold fiducial marker identification methods combined with suitable QC procedures is preferable.

### 5.5.1. Development of a quality control method

As described in Section 5.1, an X-ray image is acquired during the gold fiducial implantation procedure at Skåne University Hospital in Lund using a mobile C-Arm X-ray system. The mobility of the X-ray system enables the lithotomy position of the patient to be maintained (Figure 17). In the event of a misplaced fiducial, the maintained patient position allows easy implantation of a fourth fiducial. A similar imaging procedure for routine fiducial placement verification has been reported in the literature (Thompson et al., 2008, Gill et al., 2012).

In the study presented in **Paper IV** it was demonstrated that the C-Arm X-ray image, henceforth denoted the CkV image, could be used to confirm the location of gold fiducial markers. The locations of the fiducials had previously been determined using only MRI images in an MRI-only workflow, and were known to be correct. As this CkV image was acquired during the clinical routine for the purpose of fiducial implantation verification, no extra imaging or redundant measures were needed for fiducial verification.

The method is dependent on sCT images containing burnt in synthetic fiducials, depicted as round, 2D high-intensity objects with a diameter of 4 mm (Figure 22). The locations of the synthetic fiducials were determined by the spatial position of the gold fiducial marker center of mass. DRR images were created from sCT images, as described in Section 1.3. A common image geometry was created in which the DRR and the CkV image could be overlaid to verify the correct identification and location of the gold fiducial markers. Verification was performed by measuring the difference in position of each single fiducial in the two images.

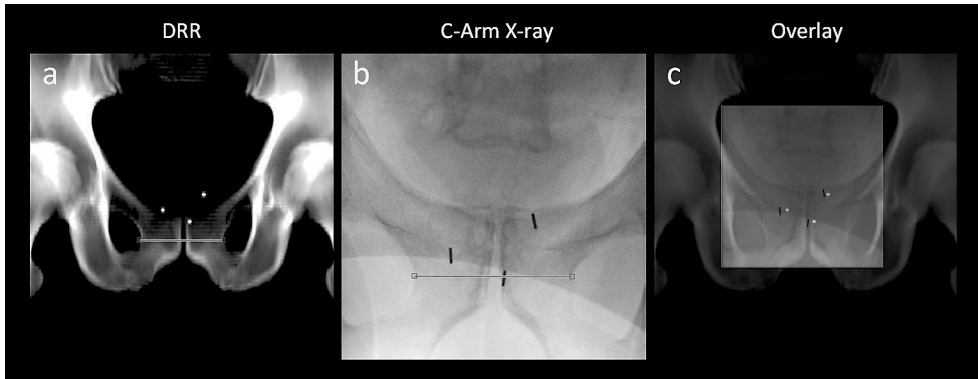


**Figure 22. DRR and C-Arm X-ray image**

Use of a C-Arm X-ray image (CkV image) to verify the locations of gold fiducial markers determined in an MRI-only workflow. a) DRR image generated from sCT images with burned in synthetic markers. b) CkV image acquired at fiducial marker implantation. As the DRR image and the CkV image had different scales, the CkV image was scaled to the DRR image using the distance between the left and right pubic bones across the pubic symphysis, indicated by the drawn lines in a) and b). c) After scaling, the CkV image was registered to the DRR image using the gold fiducial markers and overlaid. The identification and location of the gold fiducial markers was then verified by measuring the difference in position of each single fiducial in the two images.

Two problems had to be resolved to enable this process. 1) As the gold fiducial markers were implanted two weeks prior to MRI imaging, they could have migrated in the prostate, which would lead to a loss in spatial correlation, and migration was therefore assessed. 2) The CkV image did not contain any information on spatial resolution, which was needed to measure the distance between the fiducial markers. This was resolved by scaling the CkV image to the DRR image using the distance between the left and right pubic bones in both images (as shown in Figure 22).

### 5.5.2. Quality control performance

The mean absolute difference in the position of each fiducial in the two images was found to be  $1.7 \pm 1.4$  (1 SD) mm. The mean fiducial migration was determined to be  $1.2 \pm 0.7$  (1 SD) mm. This demonstrated the possibility of using a CkV image acquired at gold fiducial marker implantation, for fiducial marker position verification. All fiducial markers were confirmed to have been correctly identified. The minor fiducial migration was not considered a problem as the method did not require sub-mm precision.

In **Paper IV**, the commercial software MriPlanner from Spectronic Medical was used for sCT generation. As an anatomical distance between the pubic bones was measured in the sCT DRR image and compared to the corresponding distance in the CkV image, sCT images with high quality and geometric accuracy were vital. In two other studies, by Tenhunen et al. (2018) and Tyagi et al. (2017a), an in-house and a Philips MRCAT sCT generation method were used, respectively.

Both studies reported problems associated with gold fiducial marker identification. DRR images generated using these sCT generation methods have previously been reported to be acceptable for patient positioning (Korhonen et al., 2015, Kemppainen et al., 2018). The method described in **Paper IV** could therefore probably be applied to the methods used by Tenhunen et al. (2018) and Tyagi et al. (2017a) to improve fiducial identification, provided a CkV image is acquired at fiducial implantation.

To conclude, the method presented in **Paper IV** can be applied to both manual and automatic methods of fiducial marker identification. Furthermore, it eliminates the need to develop novel MRI acquisition sequences specifically for fiducial marker identification with the desired detection accuracy of 100%. A detection accuracy close to 100% was demonstrated in this work using MEGRE images, and these could therefore provide sufficient fiducial detection accuracy for the broad clinical implementation of MRI-only prostate radiotherapy.



# 6. Conclusions and Future Outlook

The work described in this thesis has paved the way for the implementation of a clinical MRI-only prostate radiotherapy workflow. Specifically, the work was focused on: 1) QC method development for MRI images intended for sCT generation of the male pelvis, 2) validation of the dosimetric accuracy and clinical robustness of a commercially available sCT generation method for prostate radiotherapy, and 3) the development of MRI-based methods and suitable QC procedures for intraprostatic gold fiducial marker visualization and differentiation.

## 6.1. Synthetic CT quality

The results of this work showed that the geometric distortion in a dedicated MRI acquisition sequence had negligible dosimetric impact, and no relevant geometric impact on the delineation of radiotherapy structures (**Paper I**). This suggests that the MRI acquisition sequence is suitable for sCT generation. The method developed could potentially be applied to other treatment sites.

Investigation of the dosimetric accuracy of sCT images, generated with the commercial product MriPlanner from Spectronic Medical, showed clinically negligible dose differences between sCT and CT images. sCT generation was robust for a variety of magnetic field strengths, MRI system vendors, and treatment techniques (**Paper II**). This clearly shows that sufficient dosimetric accuracy, geometric accuracy, and clinical robustness are achievable using an MRI-only prostate radiotherapy workflow. Implementation should therefore be feasible at all clinics.

## 6.2. Fiducial marker identification

The proposed MRI acquisition sequence for fiducial marker identification was shown to be a valid, robust, and feasible approach (**Paper III**). The method developed for automatic gold fiducial marker detection can probably be improved to achieve an acceptable detection level. An MRI-only prostate radiotherapy workflow without the need for any CT imaging can be safely implemented in the clinical setting using the proposed C-Arm X-ray (CkV) image method for fiducial verification QC (**Paper IV**).

### 6.3. Clinical implementation

Studies and QC methods intended for the investigation of dosimetric accuracy and fiducial marker identification in an MRI-only workflow have been presented. The methods developed and the convincing results of the studies paved the way for a prospective study of MRI-only radiotherapy of prostate cancer, called MRI-only Prostate RadiOTherapy Excluding CT (MR-PROTECT). The ultimate aim of this study is to safely implement an MRI-only radiotherapy workflow and deliver treatments to prostate cancer patients.

Preliminary results recently obtained by our group (Persson et al., 2019) showed that MRI-only treatment was successfully administered to 39 of 40 patients in a clinical setting at Skåne University Hospital in Lund, with only negligible dosimetric differences. One patient was too large for the FOV used in MRI acquisition, and was thus excluded from the study. The success of manual fiducial marker identification using MEGRE images was 100%, and fiducial locations were used for treatment positioning. The dosimetric and fiducial detection results are very encouraging, and in line with the results presented in this thesis (**Papers I, II and III**).

### 6.4. Future outlook

Multiple MRI acquisition sequences are currently required in MRI-only prostate radiotherapy workflows, which often means increased scan time and interscan patient motion (Tyagi et al., 2017a, Tenhunen et al., 2018). A single, high-resolution, fast MRI acquisition sequence, that enables target delineation, sCT generation, and gold fiducial marker identification in the same geometry, is therefore desirable.

Hip implants have previously been reported to be a contraindication for MRI-only RTP (Tyagi et al., 2017a, Kerkmeijer et al., 2018, Tenhunen et al., 2018), but recent work indicates that MRI-only RTP for prostate cancer using a 1.5 T MRI system is compatible with hip implants (Wyatt and McCallum, 2019). This should be further explored for 3 T MRI systems, where the effects of magnetic susceptibility and geometric distortion resulting from hip implants are greater.

A comprehensive MRI quality assurance (QA) program to ensure geometric accuracy and MRI system stability is crucial for a reliable MRI-only workflow (Paulson et al., 2015, Kerkmeijer et al., 2018). However, no QA standards for MRI in radiotherapy have yet been presented.

CT-independent sCT validation methods should be developed for large-scale clinical implementation. CBCT has been proposed as a promising candidate for this purpose (Palmer et al., 2018).



After successful validation and implementation of an MRI-only workflow, the possibility of reducing the target volume and possible improvements resulting from adaptive MRI-based treatment strategies, should be investigated. The use of functional MRI data for treatment follow-up and target delineation is also promising for future applications of MRI in radiotherapy (Khoo and Joon, 2006, van Schie et al., 2017, Olsson et al., 2019). MRI-only RTP for proton beam therapy has been reported to be feasible, and could be used to reduce the absorbed dose to healthy tissue (Koivula et al., 2016, Maspero et al., 2017b).

Automatic methods for fiducial identification using MEGRE images should be improved to increase detection accuracy, to match the near-perfect detection found in the manual observer study (**Paper III**). Machine learning or deep learning methods are expected to be beneficial for the four-dimensional data space of the MEGRE images. Such development is currently being pursued by the author. Another method of improving fiducial detection in MRI images could be to replace the gold fiducial markers with fiducials that can generate positive MRI signal. This type of marker must also be visible in other modalities used in radiotherapy clinics, such as kV X-ray imaging and CBCT imaging. The fiducial material should therefore contain radiopaque material, and have a low magnetic susceptibility.

Questions concerning dosimetric and geometric accuracy in MRI-only workflows are also of interest in relation to MR-linacs (Raaymakers et al., 2017, Tijssen et al., 2019). The methods presented in this thesis could probably be adapted and applied to MR-linac workflows to assess the dosimetric accuracy in sCT images when CT is not available.



# Acknowledgements

This work would not have been possible without the help of my colleagues, friends, and family, to whom I am forever grateful. I would like to express my deepest gratitude to my supervisor, **Professor Lars E. Olsson** for all his patience, guidance, and support during this work, especially during the finalization of this thesis. Despite your many obligations, you were always available in times of need for advice. Your insight and research experience have been exceptionally valuable. I truly believe I have grown as a person, a researcher and as a medical physicist as a result of this amazing journey.

I would also like to thank my three co-supervisors.

**Fredrik Nordström** – Your technical and clinical expertise was invaluable for my research, and I am especially grateful for your support during the writing of my first paper as a new PhD student.

**Adalsteinn Gunnlaugsson** – Great research requires a multidisciplinary competence, and I could not have asked for a better or more supportive oncologist. The combination of our clinical activities and research collaboration has really been the motor for the rapid clinical implementation of the research methods developed during the course of this work.

**Juha Korhonen** – Your many ideas and inspiration have made it a pleasure to work with you. Your open-mindedness, guidance, and welcoming attitude have been invaluable, and I will do my best to carry myself in the same manner as you. I hope we will collaborate again in the future.

I would also like to express my thanks to all my **colleagues** at the Department of Oncology and Radiation Physics in Lund and the Department of Medical Radiation Physics in Malmö. Thank you for being there for me in time of need.

Thanks also to **Sven Bäck**, **Per Munck af Rosenschöld** and **Tommy Knöös**, for believing in me, and for being the most supportive and understanding employers, enabling me to combine clinical duties with research activities. I especially appreciate your concern towards the end of my PhD studies.

I would like to thank **Senada Kapetanovic**, **Sveinung Groven**, **Urban Alkhed**, **Anna Lippe** and **Görel Ingner** for the acquisition of the MRI data used in this work, and for being awesome coworkers and MRI technologists.

Thanks to **Lotta Lundgren** for help with the X-ray system at the brachytherapy department, and thanks to **Sara Brockstedt** and **Sofie Ceberg** for their support and valuable help with revision of papers. Thanks also to **Silke Engelholm**, **Maria Gebre-Medhin** and **Per Nilsson** for help regarding the ethical aspects of this work, and for general support in starting up clinical projects. **Anders Olsson**, **Per Wendel** and **Jonatan Snäll** have provided valuable IT support and MRI machine support during this work – thank you for your time and effort. **Sevgi Emin** – thank you for being a good student, and for your help with the software and evaluation of the gold fiducial marker observer study.

I would like to thank all the participants in the Swedish **VINNOVA Gentle Radiotherapy project**. The success of this project has convinced me that hospitals need to collaborate more on a national level, whether it be MRI in radiotherapy or something else. We have come a long way, but this is hopefully just the beginning.

I would also like to thank **Carl Siverson** and the **Spectronic Medical staff** for good scientific collaboration and excellent support during the years of my PhD studies. I hope and believe our dedication has resulted in mutual benefits. I would also like to acknowledge the research support given by GE Healthcare in Sweden, especially that of **Axel Hartwig** and **Mathias Engström**.

To my former **colleagues in Gothenburg** – Thank you for introducing me to the amazing world of MRI, and thanks for all our wonderful nerdy discussions and pleasant times.

To **Emilia Persson**, my co-author and good friend – Thank you for the endless amounts of coffee, discussions and laughs through good and not so good times. We have both made great progress over the past years, and I am forever grateful for your support and friendship. This adventure would not have been as enjoyable without you. Thanks also to **Minna Lerner** for supporting me in my clinical duties during my paternal leave with Theo. I am very much looking forward to our future collaboration on an MRI-only workflow for the brain. Thank you **Patrik Brynolfsson** for helping out with some of my clinical commitments during the writing of this thesis.

Thank you to **Johan Olsrud** and **Anna Bäck** for both challenging and supporting me at my half-time seminar. Your guidance and curiosity were important for the rest of my PhD studies.

**Nils Rudqvist**, **Niclas Pettersson** and **Filip Szczepankiewicz** – You once told me that you would call me “grabben” (the kid) for the rest of my life if I didn’t get a PhD. I therefore feel very relieved to strip you of that pleasure and join the doctorate club. Some of you have moved far away, and I miss you every day. I am honored to be among such great intellectual friends, and look forward to future adventures with you.

Thank you **Henric Rydén**, **Bjarne Hansen** and **Johan Fischer** for being who you are. It's always a pleasure to meet you and discuss the rollercoaster rides of our lives. True friends are hard to come by, and I am really lucky to have you. **André Haraldsson** – Thank you for all our colorful scientific discussions on statistics and authorship. You also made my paternal leave more exciting than I expected. **Jonas Scherman** – my training protégé and great friend – thank you for all our interesting discussions on scientific issues and the choice of statistical methods. Your expert help on the thesis was invaluable.

Note to self: **Christian**, you finally made it all the way, you actually did it. I know you easily forget some things, so let me remind you of a couple of them for future reference: Everything has its process so don't rush things, or you will end up frustrated and with flawed methods somewhere around square one. Research takes time, and the best ideas and greatest epiphanies come outside the office. Don't act on your ideas immediately, they may not be sound in their present form, patience is the key. Don't work too late in the evening, lack of sleep ruins the next day. Remember what is most important to you, do the things you enjoy, and drink a lot of coffee with your colleagues, they are a great source of inspiration.

Till **Mamma** och **Pappa** – Jag har tydligen i väldigt ung ålder sagt ”Jag KAN gå på månen, det gäller bara att hålla balansen”. Inget stämmer bättre överens när man ska beskriva hur det är att doktorera, balans i livet har varit extremt viktigt och jag vill tacka er för att ni hjälpt mig åstadkomma detta. När man är liten är man ganska säker på att man inte vet så mycket om världen. När man är runt 20 år är övertygelsen om en allsmäktig kunskap ständigt överhängande. När man rör sig mot 35 år så inser man att föräldrarna fortfarande är en icke sinande källa av djup erfarenhet och att det fortfarande finns mycket kvar att lära. Trots detta har ni kanske inte alltid förstått vad jag har spenderat all min arbetstid på, men ni har alltid varit där. Ni har uppmanat mig att tro på mig själv, utforska det jag inte vet, vara stark och kämpa vidare i tuffa tider. Man kan inte önska sig mer än detta, tack! Till min älskade bror **Christoffer** och underbara familj vill jag säga tack för den tiden vi delar på helgerna, det betyder mycket för mig att ha er så nära.

Till **Marina** och **Theo**, mina fixa stjärnor – **Theo**, du är nu lite mer än 2 år gammal och tiden går mycket fortare än vad jag kan uppfatta. Jag hoppas att du inte känner att jag har försummat dig under dessa sista månader av förberedelser (våren 2019). Det är svårt att beskriva den kärlek och närhet jag känner till dig, jag kan inte säga annat än att inget är viktigare än du. När du är gammal nog att förstå denna text kommer du att ha många val och möjligheter framför dig i livet. Något jag lärt mig under min forskarutbildning, och som jag vill förmedla till dig, är att man inte nödvändigtvis behöver utesluta en sak för att få den andra. Med lite fantasi och planering så går det att göra båda, kanske inte samtidigt, men det går. Så var inte ledsen för sakerna du inte får gjort just nu, det kommer en tid för dessa också.

**Marina**, det är en konstig känsla att vara här i slutet på en lång, rolig, utvecklande och ibland ganska jobbig resa. Men jag har aldrig känt mig ensam i min båt för du har alltid funnits där och sett till att båten inte tar in alldeles för mycket vatten. Du har hjälpt mig sätta gränser i min arbetsinsats och visat mig att resultaten nödvändigtvis inte blir sämre av att sluta jobba vid en rimlig tid på kvällen. Dessa erfarenheter kan annars vara väldigt dyra att skaffa sig. Du har agerat terapeut, fru, mamma och underbar livskamrat, allt på samma gång. Jag vet att det inte har varit lätt för dig, och jag är dig väldigt tacksam för all stöttning jag har fått när jag behövt den som mest. Med dig vill jag spendera alla mina dagar!

## Funding

This research was supported by:

- VINNOVA: Gentle Radiotherapy project (2016-03847 and 2016-02529)
- Allmänna sjukhusets i Malmö Stiftelse för bekämpande av cancer
- Stiftelsen för cancerforskning vid Onkologiska kliniken vid Universitetssjukhuset MAS
- Skåne University Hospital, Lund, Sweden

# References

- Adjeiwaah, M., Bylund, M., Lundman, J. A., Karlsson, C. T., Jonsson, J. H. & Nyholm, T. 2018. Quantifying the Effect of 3T Magnetic Resonance Imaging Residual System Distortions and Patient-Induced Susceptibility Distortions on Radiation Therapy Treatment Planning for Prostate Cancer. *Int J Radiat Oncol Biol Phys.*, 100, 317-324.
- Adjeiwaah, M., Bylund, M., Lundman, J. A., Soderstrom, K., Zackrisson, B., Jonsson, J. H., Garpebring, A. & Nyholm, T. 2019. Dosimetric Impact of MRI Distortions: A Study on Head and Neck Cancers. *Int J Radiat Oncol Biol Phys*, 103, 994-1003.
- Arabi, H., Dowling, J. A., Burgos, N., Han, X., Greer, P. B., Koutsouvelis, N. & Zaidi, H. 2018. Comparative study of algorithms for synthetic CT generation from MRI: Consequences for MRI-guided radiation planning in the pelvic region. *Med Phys*, 45, 5218-5233.
- Bakker, C. J., Moerland, M. A., Bhagwandien, R. & Beersma, R. 1992. Analysis of machine-dependent and object-induced geometric distortion in 2DFT MR imaging. *Magn Reson Imaging*, 10, 597-608.
- Baldwin, L. N., Wachowicz, K. & Fallone, B. G. 2009. A two-step scheme for distortion rectification of magnetic resonance images. *Med Phys*, 36, 3917-26.
- Baldwin, L. N., Wachowicz, K., Thomas, S. D., Rivest, R. & Fallone, B. G. 2007. Characterization, prediction, and correction of geometric distortion in 3 T MR images. *Med Phys*, 34, 388-99.
- Barentsz, J. O., Richenberg, J., Clements, R., Choyke, P., Verma, S., Villeirs, G., Rouviere, O., Logager, V., Futterer, J. J. & European Society of Urogenital, R. 2012. ESUR prostate MR guidelines 2012. *Eur Radiol*, 22, 746-57.
- Beard, C. J., Kijewski, P., Bussiere, M., Gelman, R., Gladstone, D., Shaffer, K., Plunkett, M., Castello, P. & Coleman, C. N. 1996. Analysis of prostate and seminal vesicle motion: implications for treatment planning. *Int J Radiat Oncol Biol Phys*, 34, 451-8.
- Bellon, E. M., Haacke, E. M., Coleman, P. E., Sacco, D. C., Steiger, D. A. & Gangarosa, R. E. 1986. MR artifacts: a review. *AJR Am J Roentgenol*, 147, 1271-81.
- Benedek, H., Lerner, M., Nilsson, P., Knöös, T., Gunnlaugsson, A. & Ceberg, C. 2018. The effect of prostate motion during hypofractionated radiotherapy can be reduced by using flattening filter free beams. *Physics and Imaging in Radiation Oncology*, 6, 66-70.
- Blomqvist, L., Bäck, A., Ceberg, C., Enblad, G., Frykholm, G., Johansson, M., Olsson, L. & Zackrisson, B. 2013. MR in radiotherapy – an important step towards personalized treatment? Report from the SSM's scientific council on ionizing radiation within oncology. SSM.

- Brunt, J. N. 2010. Computed tomography-magnetic resonance image registration in radiotherapy treatment planning. *Clin Oncol (R Coll Radiol)*, 22, 688-97.
- Cao, J. J., Huang, W., Wu, H. S., Cao, M., Zhang, Y. & Jin, X. D. 2018. Prostatic Calculi: Do They Matter? *Sex Med Rev*, 6, 482-491.
- Castro, P., Roch, M., Zapatero, A., Büchser, D., Garayoa Roca, J., Ansón, C., Hernández, D., Cabrerizo, C., Chevalier, M., González, S. & Perez, L. 2018. Multicomponent Assessment of the Geometrical Uncertainty and Consequent Margins in Prostate Cancer Radiotherapy Treatment Using Fiducial Markers. *International Journal of Medical Physics, Clinical Engineering and Radiation Oncology*, 07, 503-521.
- Chan, M. F., Cohen, G. N. & Deasy, J. O. 2015. Qualitative evaluation of fiducial markers for radiotherapy imaging. *Technol Cancer Res Treat*, 14, 298-304.
- Chandarana, H., Wang, H., Tijssen, R. H. N. & Das, I. J. 2018. Emerging role of MRI in radiation therapy. *J Magn Reson Imaging*, 48, 1468-1478.
- Chen, L., Price, R. A., Jr., Nguyen, T. B., Wang, L., Li, J. S., Qin, L., Ding, M., Palacio, E., Ma, C. M. & Pollack, A. 2004. Dosimetric evaluation of MRI-based treatment planning for prostate cancer. *Phys Med Biol*, 49, 5157-70.
- Chen, S., Qin, A., Zhou, D. & Yan, D. 2018. Technical Note: U-net-generated synthetic CT images for magnetic resonance imaging-only prostate intensity-modulated radiation therapy treatment planning. *Med Phys*, 45, 5659-5665.
- Chen, Z., Ma, C. M., Paskalev, K., Li, J., Yang, J., Richardson, T., Palacio, L., Xu, X. & Chen, L. 2006. Investigation of MR image distortion for radiotherapy treatment planning of prostate cancer. *Phys Med Biol*, 51, 1393-403.
- Christiansen, R. L., Jensen, H. R. & Brink, C. 2017. Magnetic resonance only workflow and validation of dose calculations for radiotherapy of prostate cancer. *Acta Oncol*, 56, 787-791.
- Dean, C. J., Sykes, J. R., Cooper, R. A., Hatfield, P., Carey, B., Swift, S., Bacon, S. E., Thwaites, D., Sebag-Montefiore, D. & Morgan, A. M. 2012. An evaluation of four CT-MRI co-registration techniques for radiotherapy treatment planning of prone rectal cancer patients. *Br J Radiol*, 85, 61-8.
- Debois, M., Oyen, R., Maes, F., Verswijvel, G., Gatti, G., Bosmans, H., Feron, M., Bellon, E., Kutcher, G., Van Poppel, H. & Vanuytsel, L. 1999. The contribution of magnetic resonance imaging to the three-dimensional treatment planning of localized prostate cancer. *Int J Radiat Oncol Biol Phys*, 45, 857-65.
- Dinis Fernandes, C., Dinh, C. V., Steggerda, M. J., ter Beek, L. C., Smolic, M., van Buuren, L. D., Pos, F. J. & van der Heide, U. A. 2017. Prostate fiducial marker detection with the use of multi-parametric magnetic resonance imaging. *Phys Imaging Radiat Oncol*, 1, 14-20.
- Dirix, P., Haustermans, K. & Vandecaveye, V. 2014. The value of magnetic resonance imaging for radiotherapy planning. *Semin Radiat Oncol*, 24, 151-9.
- Doran, S. J., Charles-Edwards, L., Reinsberg, S. A. & Leach, M. O. 2005. A complete distortion correction for MR images: I. Gradient warp correction. *Phys Med Biol*, 50, 1343-61.



- Dowling, J. A., Lambert, J., Parker, J., Salvado, O., Fripp, J., Capp, A., Wratten, C., Denham, J. W. & Greer, P. B. 2012. An atlas-based electron density mapping method for magnetic resonance imaging (MRI)-alone treatment planning and adaptive MRI-based prostate radiation therapy. *Int J Radiat Oncol Biol Phys*, 83, e5-11.
- Edmund, J. M. & Nyholm, T. 2017. A review of substitute CT generation for MRI-only radiation therapy. *Radiat Oncol*, 12, 28.
- Eilertsen, K., Vestad, L. N., Geier, O. & Skretting, A. 2008. A simulation of MRI based dose calculations on the basis of radiotherapy planning CT images. *Acta Oncol*, 47, 1294-302.
- Emmerich, J., Laun, F. B., Pfaffenberger, A., Schilling, R., Denoix, M., Maier, F., Sterzing, F., Bostel, T. & Straub, S. 2018. Technical Note: On the size of susceptibility-induced MR image distortions in prostate and cervix in the context of MR-guided radiation therapy. *Med Phys*, 45, 1586-1593.
- Ferlay, J., Soerjomataram, I., Dikshit, R., Eser, S., Mathers, C., Rebelo, M., Parkin, D. M., Forman, D. & Bray, F. 2015. Cancer incidence and mortality worldwide: sources, methods and major patterns in GLOBOCAN 2012. *Int J Cancer*, 136, E359-86.
- Fransson, A., Andreo, P. & Potter, R. 2001. Aspects of MR image distortions in radiotherapy treatment planning. *Strahlenther Onkol*, 177, 59-73.
- GE-Healthcare 2011. *Discovery\* MR750w 3.0T Wide Bore MR with GEM Suite - Technical Data*, General Electric Company.
- Ghose, S., Mitra, J., Rivest-Henault, D., Fazlollahi, A., Stanwell, P., Pichler, P., Sun, J., Fripp, J., Greer, P. B. & Dowling, J. A. 2016. MRI-alone radiation therapy planning for prostate cancer: Automatic fiducial marker detection. *Med Phys*, 43, 2218.
- Gill, S., Li, J., Thomas, J., Bressel, M., Thursky, K., Styles, C., Tai, K. H., Duchesne, G. M. & Foroudi, F. 2012. Patient-reported complications from fiducial marker implantation for prostate image-guided radiotherapy. *Br J Radiol*, 85, 1011-7.
- Glide-Hurst, C., Nejad-Davaran, S., Weiss, S., Zheng, W., Chetty, I. J. & Renisch, S. 2018. Per-organ assessment of subject-induced susceptibility distortion for MR-only male pelvis treatment planning. *Radiat Oncol*, 13, 149.
- Glover GH, P. N. 1986. *Method for correcting image distortion due to gradient nonuniformity*. United States patent application 565,256.
- Greer, P. B., Dahl, K., Ebert, M. A., Wratten, C., White, M. & Denham, J. W. 2008. Comparison of prostate set-up accuracy and margins with off-line bony anatomy corrections and online implanted fiducial-based corrections. *J Med Imaging Radiat Oncol*, 52, 511-6.
- Greer, P. B., Dowling, J. A., Lambert, J. A., Fripp, J., Parker, J., Denham, J. W., Wratten, C., Capp, A. & Salvado, O. 2011. A magnetic resonance imaging-based workflow for planning radiation therapy for prostate cancer. *Med J Aust*, 194, S24-7.
- Gunnlaugsson, A., Persson, E., Gustafsson, C., Kjellén, E., Ambolt, P., Engelholm, S., Nilsson, P. & Olsson, L. E. 2019. Target definition in radiotherapy of prostate cancer using magnetic resonance imaging only workflow. *Physics and Imaging in Radiation Oncology*, 9, 89-91.

- Gustafsson, C., Sohlin, M. & Filipsson, L. 2016. *Method book for the use of MRI in radiotherapy* [Online]. Available: <http://gentleradiotherapy.se/methodology-guide-for-mr-in-rt/> [Accessed 2019-04-05].
- Helle, M. S., N, Frantzen-Steneker, M., Schulz, H., Stehning, C., Heide, U. & Renisch, S. 2014. Evaluation of Dixon based Soft Tissue and Bone Classification in the Pelvis for MR-only-based Radiation Therapy Planning. *Proc. Intl. Soc. Mag. Reson. Med.* 22.
- Henderson, D. R., Tree, A. C., Harrington, K. J. & van As, N. J. 2018. Dosimetric Implications of Computerised Tomography-Only versus Magnetic Resonance-Fusion Contouring in Stereotactic Body Radiotherapy for Prostate Cancer. *Medicines (Basel)*, 5, 32.
- Henschel, B., Oehler, W., Strauss, D., Ulrich, A. & Malich, A. 2011. Definition of the CTV prostate in CT and MRI by using CT-MRI image fusion in IMRT planning for prostate cancer. *Strahlenther Onkol*, 187, 183-90.
- Hood, M. N., Ho, V. B., Smirniotopoulos, J. G. & Szumowski, J. 1999. Chemical shift: the artifact and clinical tool revisited. *Radiographics*, 19, 357-71.
- Hricak, H. 2005. MR imaging and MR spectroscopic imaging in the pre-treatment evaluation of prostate cancer. *Br J Radiol*, 78 Spec No 2, S103-11.
- Huang, K. C., Cao, Y., Baharom, U. & Balter, J. M. 2016. Phantom-based characterization of distortion on a magnetic resonance imaging simulator for radiation oncology. *Phys Med Biol*, 61, 774-90.
- Hyun, J. S. 2018. Clinical Significance of Prostatic Calculi: A Review. *World J Mens Health*, 36, 15-21.
- IAEA 2004. *Commissioning and Quality Assurance of Computerized Planning Systems for Radiation Treatment of Cancer*, Vienna, INTERNATIONAL ATOMIC ENERGY AGENCY.
- IAEA 2016. *Accuracy Requirements and Uncertainties in Radiotherapy*, Vienna, INTERNATIONAL ATOMIC ENERGY AGENCY.
- Jackson, A. S., Reinsberg, S. A., Sohaib, S. A., Charles-Edwards, E. M., Mangar, S. A., South, C. P., Leach, M. O. & Dearnaley, D. P. 2007. Distortion-corrected T2 weighted MRI: a novel approach to prostate radiotherapy planning. *Br J Radiol*, 80, 926-33.
- Janke, A., Zhao, H., Cowin, G. J., Galloway, G. J. & Doddrell, D. M. 2004. Use of spherical harmonic deconvolution methods to compensate for nonlinear gradient effects on MRI images. *Magn Reson Med*, 52, 115-22.
- Johansson, A., Karlsson, M., Yu, J., Asklund, T. & Nyholm, T. 2012. Voxel-wise uncertainty in CT substitute derived from MRI. *Med Phys*, 39, 3283-90.
- Johnstone, E., Wyatt, J. J., Henry, A. M., Short, S. C., Sebag-Montefiore, D., Murray, L., Kelly, C. G., McCallum, H. M. & Speight, R. 2018. Systematic Review of Synthetic Computed Tomography Generation Methodologies for Use in Magnetic Resonance Imaging-Only Radiation Therapy. *Int J Radiat Oncol Biol Phys*, 100, 199-217.
- Jonsson, J. H., Garpebring, A., Karlsson, M. G. & Nyholm, T. 2012. Internal fiducial markers and susceptibility effects in MRI-simulation and measurement of spatial accuracy. *Int J Radiat Oncol Biol Phys*, 82, 1612-8.

- Kapanen, M., Collan, J., Beule, A., Seppala, T., Saarilahti, K. & Tenhunen, M. 2013. Commissioning of MRI-only based treatment planning procedure for external beam radiotherapy of prostate. *Magn Reson Med*, 70, 127-35.
- Karlsson, M., Karlsson, M. G., Nyholm, T., Amies, C. & Zackrisson, B. 2009. Dedicated magnetic resonance imaging in the radiotherapy clinic. *Int J Radiat Oncol Biol Phys*, 74, 644-51.
- Kassim, I., Joosten, H., Barnhoorn, J. C., Heijmen, B. J. & Dirkx, M. L. 2011. Implications of artefacts reduction in the planning CT originating from implanted fiducial markers. *Med Dosim*, 36, 119-25.
- Kemppainen, R., Vaara, T., Joensuu, T. & Kiljunen, T. 2018. Accuracy and precision of patient positioning for pelvic MR-only radiation therapy using digitally reconstructed radiographs. *Phys Med Biol*, 63, 055009.
- Kerkhof, E. M., Put, R. W. v. d., Raaymakers, B. W., van der Heide, U. A., van Vulpen, M. & Lagendijk, J. J. W. 2008. Variation in target and rectum dose due to prostate deformation: an assessment by repeated MR imaging and treatment planning. *Physics in Medicine and Biology*, 53, 5623-5634.
- Kerkmeijer, L. G. W., Maspero, M., Meijer, G. J., van der Voort van Zyp, J. R. N., de Boer, H. C. J. & van den Berg, C. A. T. 2018. Magnetic Resonance Imaging only Workflow for Radiotherapy Simulation and Planning in Prostate Cancer. *Clin Oncol (R Coll Radiol)*, 30, 692-701.
- Khoo, V. S. & Joon, D. L. 2006. New developments in MRI for target volume delineation in radiotherapy. *Br J Radiol*, 79 Spec No 1, S2-15.
- Koivula, L., Wee, L. & Korhonen, J. 2016. Feasibility of MRI-only treatment planning for proton therapy in brain and prostate cancers: Dose calculation accuracy in substitute CT images. *Med Phys*, 43, 4634.
- Korhonen, J., Kapanen, M., Keyrilainen, J., Seppala, T. & Tenhunen, M. 2014a. A dual model HU conversion from MRI intensity values within and outside of bone segment for MRI-based radiotherapy treatment planning of prostate cancer. *Med Phys*, 41, 011704.
- Korhonen, J., Kapanen, M., Keyrilainen, J., Seppala, T., Tuomikoski, L. & Tenhunen, M. 2014b. Influence of MRI-based bone outline definition errors on external radiotherapy dose calculation accuracy in heterogeneous pseudo-CT images of prostate cancer patients. *Acta Oncol*, 53, 1100-6.
- Korhonen, J., Kapanen, M., Sonke, J. J., Wee, L., Salli, E., Keyrilainen, J., Seppala, T. & Tenhunen, M. 2015. Feasibility of MRI-based reference images for image-guided radiotherapy of the pelvis with either cone-beam computed tomography or planar localization images. *Acta Oncol*, 54, 889-95.
- Korsager, A. S., Carl, J. & Riis Ostergaard, L. 2016. Comparison of manual and automatic MR-CT registration for radiotherapy of prostate cancer. *J Appl Clin Med Phys*, 17, 294-303.
- Korsholm, M. E., Waring, L. W. & Edmund, J. M. 2014. A criterion for the reliable use of MRI-only radiotherapy. *Radiat Oncol*, 9, 16.

- Kupelian, P. A., Willoughby, T. R., Meeks, S. L., Forbes, A., Wagner, T., Maach, M. & Langen, K. M. 2005. Intraprostatic fiducials for localization of the prostate gland: monitoring intermarker distances during radiation therapy to test for marker stability. *Int J Radiat Oncol Biol Phys*, 62, 1291-6.
- Köhler, M., Vaara, T., Van Grootel, M., Hoogeveen, R., Kemppainen, R. & Renisch, S. 2015. MR-only simulation for radiotherapy planning treatment planning. *White paper: Philips MRCAT for prostate dose calculations using only MRI data*, 1-16.
- Lambert, J., Greer, P. B., Menk, F., Patterson, J., Parker, J., Dahl, K., Gupta, S., Capp, A., Wratten, C., Tang, C., Kumar, M., Dowling, J., Hauville, S., Hughes, C., Fisher, K., Lau, P., Denham, J. W. & Salvado, O. 2011. MRI-guided prostate radiation therapy planning: Investigation of dosimetric accuracy of MRI-based dose planning. *Radiother Oncol*, 98, 330-4.
- Landberg, T., Chavaudra, J., Dobbs, J., Hanks, G., Johansson, K.-A., Möller, T. & Purdy, J. 1993. Report 50. *Journal of the International Commission on Radiation Units and Measurements*, os26, NP-NP.
- Low, D. A., Harms, W. B., Mutic, S. & Purdy, J. A. 1998. A technique for the quantitative evaluation of dose distributions. *Med Phys*, 25, 656-61.
- Lundman, J. A., Bylund, M., Garpebring, A., Thellenberg Karlsson, C. & Nyholm, T. 2017. Patient-induced susceptibility effects simulation in magnetic resonance imaging. *Phys Imaging Radiat Oncol*, 1, 41-45.
- Maspero, M., Savenije, M. H. F., Dinkla, A. M., Seevinck, P. R., Intven, M. P. W., Jurgenliemk-Schulz, I. M., Kerkmeijer, L. G. W. & van den Berg, C. A. T. 2018a. Dose evaluation of fast synthetic-CT generation using a generative adversarial network for general pelvis MR-only radiotherapy. *Phys Med Biol*, 63, 185001.
- Maspero, M., Seevinck, P. R., Schubert, G., Hoesl, M. A., van Asselen, B., Viergever, M. A., Legendijk, J. J., Meijer, G. J. & van den Berg, C. A. 2017a. Quantification of confounding factors in MRI-based dose calculations as applied to prostate IMRT. *Phys Med Biol*, 62, 948-965.
- Maspero, M., Seevinck, P. R., Willems, N. J. W., Sikkes, G. G., de Kogel, G. J., de Boer, H. C. J., van der Voort van Zyp, J. R. N. & van den Berg, C. A. T. 2018b. Evaluation of gold fiducial marker manual localisation for magnetic resonance-only prostate radiotherapy. *Radiation Oncology*, 13, 105.
- Maspero, M., van den Berg, C. A. T., Landry, G., Belka, C., Parodi, K., Seevinck, P. R., Raaymakers, B. W. & Kurz, C. 2017b. Feasibility of MR-only proton dose calculations for prostate cancer radiotherapy using a commercial pseudo-CT generation method. *Phys Med Biol*, 62, 9159-9176.
- Maspero, M., van den Berg, C. A. T., Zijlstra, F., Sikkes, G. G., de Boer, H. C. J., Meijer, G. J., Kerkmeijer, L. G. W., Viergever, M. A., Legendijk, J. J. W. & Seevinck, P. R. 2017c. Evaluation of an automatic MR-based gold fiducial marker localisation method for MR-only prostate radiotherapy. *Phys Med Biol*, 62, 7981-8002.
- McJury, M., O'Neill, A., Lawson, M., McGrath, C., Grey, A., Page, W. & O'Sullivan, J. M. 2011. Assessing the image quality of pelvic MR images acquired with a flat couch for radiotherapy treatment planning. *Br J Radiol*, 84, 750-5.

- McRobbie, D. W. 2007. *MRI from picture to proton*, Cambridge, UK ; New York, Cambridge University Press.
- Menard, C., Paulson, E., Nyholm, T., McLaughlin, P., Liney, G., Dirix, P. & van der Heide, U. A. 2018. Role of Prostate MR Imaging in Radiation Oncology. *Radiol Clin North Am*, 56, 319-325.
- Metcalf, P., Liney, G. P., Holloway, L., Walker, A., Barton, M., Delaney, G. P., Vinod, S. & Tome, W. 2013. The potential for an enhanced role for MRI in radiation-therapy treatment planning. *Technol Cancer Res Treat*, 12, 429-46.
- Michiels, J., Bosmans, H., Pelgrims, P., Vandermeulen, D., Gybels, J., Marchal, G. & Suetens, P. 1994. On the problem of geometric distortion in magnetic resonance images for stereotactic neurosurgery. *Magn Reson Imaging*, 12, 749-65.
- Moman, M. R., van der Heide, U. A., Kotte, A. N., van Moorselaar, R. J., Bol, G. H., Franken, S. P. & van Vulpen, M. 2010. Long-term experience with transrectal and transperineal implantations of fiducial gold markers in the prostate for position verification in external beam radiotherapy; feasibility, toxicity and quality of life. *Radiother Oncol*, 96, 38-42.
- Murphy, G., Haider, M., Ghai, S. & Sreeharsha, B. 2013. The expanding role of MRI in prostate cancer. *AJR Am J Roentgenol*, 201, 1229-38.
- Mustafi, D., Fan, X., Peng, B., Foxley, S., Palgen, J. & Newstead, G. M. 2015. Using MRI to detect and differentiate calcium oxalate and calcium hydroxyapatite crystals in air-bubble-free phantom. *Phys Med*, 31, 1075-1079.
- Ng, M., Brown, E., Williams, A., Chao, M., Lawrentschuk, N. & Chee, R. 2014. Fiducial markers and spacers in prostate radiotherapy: current applications. *BJU Int*, 113 Suppl 2, 13-20.
- Nyholm, T. & Jonsson, J. 2014. Counterpoint: Opportunities and challenges of a magnetic resonance imaging-only radiotherapy work flow. *Semin Radiat Oncol*, 24, 175-80.
- Nyholm, T., Nyberg, M., Karlsson, M. G. & Karlsson, M. 2009. Systematisation of spatial uncertainties for comparison between a MR and a CT-based radiotherapy workflow for prostate treatments. *Radiat Oncol*, 4, 54.
- O'Neill, A. G., Jain, S., Hounsell, A. R. & O'Sullivan, J. M. 2016. Fiducial marker guided prostate radiotherapy: a review. *Br J Radiol*, 89, 20160296.
- Oliveira, F. P. & Tavares, J. M. 2014. Medical image registration: a review. *Comput Methods Biomech Biomed Engin*, 17, 73-93.
- Olsrud, J., Latt, J., Brockstedt, S., Romner, B. & Bjorkman-Burtscher, I. M. 2005. Magnetic resonance imaging artifacts caused by aneurysm clips and shunt valves: dependence on field strength (1.5 and 3 T) and imaging parameters. *J Magn Reson Imaging*, 22, 433-7.
- Olsson, L. E., Johansson, M., Zackrisson, B. & Blomqvist, L. K. 2019. Basic concepts and applications of functional magnetic resonance imaging for radiotherapy of prostate cancer. *Physics and Imaging in Radiation Oncology*, 9, 50-57.
- Owen, R., Kron, T., Foroudi, F., Cox, J., Zhu, L., Cramb, J., Sparks, L. & Duchesne, G. 2008. The Detectability and Localization Accuracy of Implanted Fiducial Markers Determined on In-Room Computerized Tomography (CT) and Electronic Portal Images (EPI). *Medical Dosimetry*, 33, 226-233.

- Owringi, A. M., Greer, P. B. & Glide-Hurst, C. K. 2018. MRI-only treatment planning: benefits and challenges. *Phys Med Biol*, 63, 05TR01.
- Pallotta, S. & Bucciolini, M. 2010. A simple method to test the geometrical reliability of digital reconstructed radiograph (DRR). *J Appl Clin Med Phys*, 11, 3128.
- Palmer, E., Persson, E., Ambolt, P., Gustafsson, C., Gunnlaugsson, A. & Olsson, L. E. 2018. Cone beam CT for QA of synthetic CT in MRI only for prostate patients. *J Appl Clin Med Phys*, 19, 44-52.
- Parker, C. 2003. Magnetic resonance imaging in the radiation treatment planning of localized prostate cancer using intra-prostatic fiducial markers for computed tomography co-registration. *Radiother Oncol*, 66, 217-224.
- Pathmanathan, A. U., Schmidt, M. A., Brand, D. H., Kousi, E., van As, N. J. & Tree, A. C. 2019. Improving fiducial and prostate capsule visualization for radiotherapy planning using MRI. *J Appl Clin Med Phys*, 20, 27-36.
- Pathmanathan, A. U., van As, N. J., Kerkmeijer, L. G. W., Christodouleas, J., Lawton, C. A. F., Vesprini, D., van der Heide, U. A., Frank, S. J., Nill, S., Oelfke, U., van Herk, M., Li, X. A., Mittauer, K., Ritter, M., Choudhury, A. & Tree, A. C. 2018. Magnetic Resonance Imaging-Guided Adaptive Radiation Therapy: A "Game Changer" for Prostate Treatment? *Int J Radiat Oncol Biol Phys*, 100, 361-373.
- Paulson, E. S., Erickson, B., Schultz, C. & Allen Li, X. 2015. Comprehensive MRI simulation methodology using a dedicated MRI scanner in radiation oncology for external beam radiation treatment planning. *Med Phys*, 42, 28-39.
- Persson, E., Gustafsson, C., Nilsson, J., Engelholm, S., Bäck, S., Olsson, L. & Gunnlaugsson, A. 2019. Treating prostate cancer with MRI-only radiotherapy (EP-2063). *ESTRO 38*. Milan, Italy.
- Persson, E., Gustafsson, C., Nordstrom, F., Sohlén, M., Gunnlaugsson, A., Petruson, K., Rintela, N., Hed, K., Blomqvist, L., Zackrisson, B., Nyholm, T., Olsson, L. E., Siversson, C. & Jonsson, J. 2017. MR-OPERA: A Multicenter/Multivendor Validation of Magnetic Resonance Imaging-Only Prostate Treatment Planning Using Synthetic Computed Tomography Images. *Int J Radiat Oncol Biol Phys*, 99, 692-700.
- Port, J. D. & Pomper, M. G. 2000. Quantification and minimization of magnetic susceptibility artifacts on GRE images. *J Comput Assist Tomogr*, 24, 958-64.
- Price, R. G., Knight, R. A., Hwang, K. P., Bayram, E., Nejad-Davarani, S. P. & Glide-Hurst, C. K. 2017. Optimization of a novel large field of view distortion phantom for MR-only treatment planning. *J Appl Clin Med Phys*, 18, 51-61.
- Raaymakers, B. W., Jurgenliemk-Schulz, I. M., Bol, G. H., Glitznér, M., Kotte, A., van Asselen, B., de Boer, J. C. J., Bluemink, J. J., Hackett, S. L., Moerland, M. A., Woodings, S. J., Wolthaus, J. W. H., van Zijp, H. M., Philippens, M. E. P., Tijssen, R., Kok, J. G. M., de Groot-van Breugel, E. N., Kiekebosch, I., Meijers, L. T. C., Nomden, C. N., Sikkes, G. G., Doornaert, P. A. H., Eppinga, W. S. C., Kasperts, N., Kerkmeijer, L. G. W., Tersteeg, J. H. A., Brown, K. J., Pais, B., Woodhead, P. & Lagendijk, J. J. W. 2017. First patients treated with a 1.5 T MRI-Linac: clinical proof of concept of a high-precision, high-field MRI guided radiotherapy treatment. *Phys Med Biol*, 62, L41-L50.

- Rasch, C., Barillot, I., Remeijer, P., Touw, A., van Herk, M. & Lebesque, J. V. 1999. Definition of the prostate in CT and MRI: a multi-observer study. *Int J Radiat Oncol Biol Phys*, 43, 57-66.
- Reinsberg, S. A., Doran, S. J., Charles-Edwards, E. M. & Leach, M. O. 2005. A complete distortion correction for MR images: II. Rectification of static-field inhomogeneities by similarity-based profile mapping. *Phys Med Biol*, 50, 2651-61.
- Roach, M., 3rd, Faillace-Akazawa, P., Malfatti, C., Holland, J. & Hricak, H. 1996. Prostate volumes defined by magnetic resonance imaging and computerized tomographic scans for three-dimensional conformal radiotherapy. *Int J Radiat Oncol Biol Phys*, 35, 1011-8.
- Roberson, P. L., McLaughlin, P. W., Narayana, V., Troyer, S., Hixson, G. V. & Kessler, M. L. 2005. Use and uncertainties of mutual information for computed tomography/magnetic resonance (CT/MR) registration post permanent implant of the prostate. *Med Phys*, 32, 473-82.
- Rosewall, T., Kong, V., Vesprini, D., Catton, C., Chung, P., Ménard, C. & Bayley, A. 2009. Prostate delineation using CT and MRI for radiotherapy patients with bilateral hip prostheses. *Radiotherapy and Oncology*, 90, 325-330.
- Sander, L., Langkilde, N. C., Holmberg, M. & Carl, J. 2014. MRI target delineation may reduce long-term toxicity after prostate radiotherapy. *Acta Oncol*, 53, 809-14.
- Scarbrough, T. J. & Fuller, C. D. 2006. Fiducial Markers in Image-guided Radiotherapy of the Prostate. *US Oncological Disease*, 1, 75-9.
- Schadewaldt, N., Schulz, H., Helle, M., Frantzen-Stenecker, M., Heide, U. & Renisch, S. 2014. SU-E-J-141: Comparison of Dose Calculation On Automatically Generated MRBased ED Maps and Corresponding Patient CT for Clinical Prostate EBRT Plans. *Medical Physics*, 41, 188-188.
- Schallenkamp, J. M., Herman, M. G., Kruse, J. J. & Pisansky, T. M. 2005. Prostate position relative to pelvic bony anatomy based on intraprostatic gold markers and electronic portal imaging. *Int J Radiat Oncol Biol Phys*, 63, 800-11.
- Schenck, J. F. 1996. The role of magnetic susceptibility in magnetic resonance imaging: MRI magnetic compatibility of the first and second kinds. *Med Phys*, 23, 815-50.
- Schmidt, M. A. & Payne, G. S. 2015. Radiotherapy planning using MRI. *Phys Med Biol*, 60, R323-61.
- Segedin, B. & Petric, P. 2016. Uncertainties in target volume delineation in radiotherapy – are they relevant and what can we do about them? *Radiology and Oncology*, 50, 254-262.
- Seppala, T., Visapaa, H., Collan, J., Kapanen, M., Beule, A., Kouri, M., Tenhunen, M. & Saarilahti, K. 2015. Converting from CT- to MRI-only-based target definition in radiotherapy of localized prostate cancer: A comparison between two modalities. *Strahlenther Onkol*, 191, 862-8.
- Sfanos, K. S., Wilson, B. A., De Marzo, A. M. & Isaacs, W. B. 2009. Acute inflammatory proteins constitute the organic matrix of prostatic corpora amylacea and calculi in men with prostate cancer. *Proc Natl Acad Sci U S A*, 106, 3443-8.
- Siversson, C., Nordstrom, F., Nilsson, T., Nyholm, T., Jonsson, J., Gunnlaugsson, A. & Olsson, L. E. 2015. Technical Note: MRI only prostate radiotherapy planning using the statistical decomposition algorithm. *Med Phys*, 42, 6090-7.

- Spees, W. M., Buhl, N., Sun, P., Ackerman, J. J., Neil, J. J. & Garbow, J. R. 2011. Quantification and compensation of eddy-current-induced magnetic-field gradients. *J Magn Reson*, 212, 116-23.
- Stanescu, T. & Jaffray, D. 2018. Technical Note: Harmonic analysis applied to MR image distortion fields specific to arbitrarily shaped volumes. *Med Phys*, 45, 3705-12.
- Stanescu, T., Wachowicz, K. & Jaffray, D. A. 2012. Characterization of tissue magnetic susceptibility-induced distortions for MRIgRT. *Med Phys*, 39, 7185-93.
- Steenbakkens, R. J. H. M., Deurloo, K. E. I., Nowak, P. J. C. M., Lebesque, J. V., van Herk, M. & Rasch, C. R. N. 2003. Reduction of dose delivered to the rectum and bulb of the penis using MRI delineation for radiotherapy of the prostate. *Int J Radiat Oncol Biol Phys*, 57, 1269-1279.
- Sun, J., Dowling, J., Pichler, P., Menk, F., Rivest-Henault, D., Lambert, J., Parker, J., Arm, J., Best, L., Martin, J., Denham, J. W. & Greer, P. B. 2015a. MRI simulation: end-to-end testing for prostate radiation therapy using geometric pelvic MRI phantoms. *Phys Med Biol*, 60, 3097-109.
- Sun, J., Dowling, J. A., Pichler, P., Parker, J., Martin, J., Stanwell, P., Arm, J., Menk, F. & Greer, P. B. 2015b. Investigation on the performance of dedicated radiotherapy positioning devices for MR scanning for prostate planning. *J Appl Clin Med Phys*, 16, 4848.
- Sun, J., Pichler, P., Dowling, J., Menk, F., Stanwell, P., Arm, J. & Greer, P. B. 2014. MR simulation for prostate radiation therapy: effect of coil mounting position on image quality. *Br J Radiol*, 87, 20140325.
- Tanner, S. F., Finnigan, D. J., Khoo, V. S., Mayles, P., Dearnaley, D. P. & Leach, M. O. 2000. Radiotherapy planning of the pelvis using distortion corrected MR images: the removal of system distortions. *Phys Med Biol*, 45, 2117-32.
- Tenhunen, M., Korhonen, J., Kapanen, M., Seppala, T., Koivula, L., Collan, J., Saarilahti, K. & Visapaa, H. 2018. MRI-only based radiation therapy of prostate cancer: workflow and early clinical experience. *Acta Oncol*, 57, 902-907.
- Thompson, A., Fox, C., Foroudi, F., Styles, C., Tai, K. H., Owen, R. & Laferlita, M. 2008. Planning and implementing an implanted fiducial programme for prostate cancer radiation therapy. *J Med Imaging Radiat Oncol*, 52, 419-24.
- Thwaites, D. 2013. Accuracy required and achievable in radiotherapy dosimetry: have modern technology and techniques changed our views? *Journal of Physics: Conference Series*, 444, 012006.
- Tijssen, R. H. N., Philippens, M. E. P., Paulson, E. S., Glitzner, M., Chugh, B., Wetscherek, A., Dubec, M., Wang, J. & van der Heide, U. A. 2019. MRI commissioning of 1.5T MR-linac systems – a multi-institutional study. *Radiotherapy and Oncology*, 132, 114-120.
- Torfeh, T., Hammoud, R., McGarry, M., Al-Hammadi, N. & Perkins, G. 2015. Development and validation of a novel large field of view phantom and a software module for the quality assurance of geometric distortion in magnetic resonance imaging. *Magn Reson Imaging*, 33, 939-49.



- Torfeh, T., Hammoud, R., Perkins, G., McGarry, M., Aouadi, S., Celik, A., Hwang, K. P., Stancanello, J., Petric, P. & Al-Hammadi, N. 2016. Characterization of 3D geometric distortion of magnetic resonance imaging scanners commissioned for radiation therapy planning. *Magn Reson Imaging*, 34, 645-53.
- Tyagi, N., Fontenla, S., Zelefsky, M., Chong-Ton, M., Ostergren, K., Shah, N., Warner, L., Kadbi, M., Mechalakos, J. & Hunt, M. 2017a. Clinical workflow for MR-only simulation and planning in prostate. *Radiat Oncol*, 12, 119.
- Tyagi, N., Fontenla, S., Zhang, J., Cloutier, M., Kadbi, M., Mechalakos, J., Zelefsky, M., Deasy, J. & Hunt, M. 2017b. Dosimetric and workflow evaluation of first commercial synthetic CT software for clinical use in pelvis. *Phys Med Biol*, 62, 2961-2975.
- Ulin, K., Urie, M. M. & Cherlow, J. M. 2010. Results of a multi-institutional benchmark test for cranial CT/MR image registration. *Int J Radiat Oncol Biol Phys*, 77, 1584-9.
- Umair, M., Javed, I., Rehman, M., Madni, A., Javeed, A., Ghafoor, A. & Ashraf, M. 2016. Nanotoxicity of Inert Materials: The Case of Gold, Silver and Iron. *J Pharm Pharm Sci*, 19, 161-80.
- Usmani, N., Sloboda, R., Kamal, W., Ghosh, S., Pervez, N., Pedersen, J., Yee, D., Danielson, B., Murtha, A., Amanie, J. & Monajemi, T. 2011. Can Images Obtained With High Field Strength Magnetic Resonance Imaging Reduce Contouring Variability of the Prostate? *Int J Radiat Oncol Biol Phys*, 80, 728-734.
- Walker, A., Liney, G., Holloway, L., Dowling, J., Rivest-Henault, D. & Metcalfe, P. 2015. Continuous table acquisition MRI for radiotherapy treatment planning: distortion assessment with a new extended 3D volumetric phantom. *Med Phys*, 42, 1982-91.
- Walker, A., Metcalfe, P., Liney, G., Batumalai, V., Dundas, K., Glide-Hurst, C., Delaney, G. P., Boxer, M., Yap, M. L., Dowling, J., Rivest-Henault, D., Pogson, E. & Holloway, L. 2016. MRI geometric distortion: Impact on tangential whole-breast IMRT. *J Appl Clin Med Phys*, 17, 7-19.
- van der Heide, U. A., Kotte, A. N., Dehnad, H., Hofman, P., Lagenijk, J. J. & van Vulpen, M. 2007. Analysis of fiducial marker-based position verification in the external beam radiotherapy of patients with prostate cancer. *Radiother Oncol*, 82, 38-45.
- van Herk, M. 2004. Errors and margins in radiotherapy. *Semin Radiat Oncol*, 14, 52-64.
- van Herk, M., Remeijer, P., Rasch, C. & Lebesque, J. V. 2000. The probability of correct target dosage: dose-population histograms for deriving treatment margins in radiotherapy. *Int J Radiat Oncol Biol Phys*, 47, 1121-35.
- van Schie, M. A., Steenbergen, P., Dinh, C. V., Ghobadi, G., van Houdt, P. J., Pos, F. J., Heijmink, S., van der Poel, H. G., Renisch, S., Vik, T. & van der Heide, U. A. 2017. Repeatability of dose painting by numbers treatment planning in prostate cancer radiotherapy based on multiparametric magnetic resonance imaging. *Phys Med Biol*, 62, 5575-5588.
- Wang, D., Strugnell, W., Cowin, G., Doddrell, D. M. & Slaughter, R. 2004. Geometric distortion in clinical MRI systems Part I: evaluation using a 3D phantom. *Magn Reson Imaging*, 22, 1211-21.

- Wegener, D., Zips, D., Thorwarth, D., Weiss, J., Othman, A. E., Grosse, U., Notohamiprodjo, M., Nikolaou, K. & Muller, A. C. 2019. Precision of T2 TSE MRI-CT-image fusions based on gold fiducials and repetitive T2 TSE MRI-MRI-fusions for adaptive IGRT of prostate cancer by using phantom and patient data. *Acta Oncol*, 58, 88-94.
- Weygand, J., Fuller, C. D., Ibbott, G. S., Mohamed, A. S., Ding, Y., Yang, J., Hwang, K. P. & Wang, J. 2016. Spatial Precision in Magnetic Resonance Imaging-Guided Radiation Therapy: The Role of Geometric Distortion. *Int J Radiat Oncol Biol Phys*, 95, 1304-16.
- Widmark, A. 2008. *Phase III study of HYPOfractionated RadioTherapy of intermediate risk localised Prostate Cancer* [Online]. BioMed Central. Available: <http://www.isrctn.com/ISRCTN45905321> [Accessed 2019-04-05].
- Villeirs, G. M. & De Meerleer, G. O. 2007. Magnetic resonance imaging (MRI) anatomy of the prostate and application of MRI in radiotherapy planning. *Eur J Radiol*, 63, 361-8.
- Villeirs, G. M., Van Vaerenbergh, K., Vakaet, L., Bral, S., Claus, F., De Neve, W. J., Verstraete, K. L. & De Meerleer, G. O. 2005. Interobserver delineation variation using CT versus combined CT + MRI in intensity-modulated radiotherapy for prostate cancer. *Strahlenther Onkol*, 181, 424-30.
- Wood, T. J., Davis, A. T., Earley, J., Edyvean, S., Findlay, U., Lindsay, R., Nisbet, A., Palmer, A. L., Plaistow, R. & Williams, M. 2018. IPEM topical report: the first UK survey of dose indices from radiotherapy treatment planning computed tomography scans for adult patients. *Phys Med Biol*, 63, 185008.
- Wyatt, J., Hedley, S., Johnstone, E., Speight, R., Kelly, C., Henry, A., Short, S., Murray, L., Sebag-Montefiore, D. & McCallum, H. 2018. Evaluating the repeatability and set-up sensitivity of a large field of view distortion phantom and software for magnetic resonance-only radiotherapy. *Phys Imaging Radiat Oncol*, 6, 31-38.
- Wyatt, J. & McCallum, H. 2019. Applying a commercial atlas-based synthetic Computed Tomography algorithm to patients with hip prostheses for prostate Magnetic Resonance-only radiotherapy. *Radiotherapy and Oncology*, 133, 100-105.
- Yan, Y., Yang, J., Beddar, S., Ibbott, G., Wen, Z., Court, L. E., Hwang, K.-P., Kadbi, M., Krishnan, S., Fuller, C. D., Frank, S. J., Yang, J., Balter, P., Kudchadker, R. J. & Wang, J. 2018. A methodology to investigate the impact of image distortions on the radiation dose when using magnetic resonance images for planning. *Physics in Medicine & Biology*, 63, 085005.
- Yu, H., McKenzie, C. A., Shimakawa, A., Vu, A. T., Brau, A. C., Beatty, P. J., Pineda, A. R., Brittain, J. H. & Reeder, S. B. 2007. Multiecho reconstruction for simultaneous water-fat decomposition and T2\* estimation. *J Magn Reson Imaging*, 26, 1153-61.
- Zangger, K. & Armitage, L. M. 1999. Silver and gold NMR. *Met Based Drugs*, 6, 239-45.
- Zeng, G. G., McGowan, T. S., Larsen, T. M., Bruce, L. M., Moran, N. K., Tsao, J. R. & MacPherson, M. S. 2008. Calcifications are potential surrogates for prostate localization in image-guided radiotherapy. *Int J Radiat Oncol Biol Phys*, 72, 963-6.

Paper I





# Assessment of dosimetric impact of system specific geometric distortion in an MRI only based radiotherapy workflow for prostate

C Gustafsson<sup>1,2</sup>, F Nordström<sup>3</sup>, E Persson<sup>1</sup>, J Brynolfsson<sup>4</sup>  
and L E Olsson<sup>2</sup>

<sup>1</sup> Department of Hematology, Oncology and Radiation Physics, Skåne University Hospital, Lund, Sweden

<sup>2</sup> Department of Medical Physics, Lund University, Malmö, Sweden

<sup>3</sup> Department of Medical Physics and Biomedical Engineering, Sahlgrenska University Hospital, Gothenburg, Sweden

<sup>4</sup> Spectronic Medical AB, Helsingborg, Sweden

E-mail: christian.k.gustafsson@skane.se

Received 11 August 2016, revised 4 February 2017

Accepted for publication 9 February 2017

Published 17 March 2017



## Abstract

Dosimetric errors in a magnetic resonance imaging (MRI) only radiotherapy workflow may be caused by system specific geometric distortion from MRI. The aim of this study was to evaluate the impact on planned dose distribution and delineated structures for prostate patients, originating from this distortion. A method was developed, in which computer tomography (CT) images were distorted using the MRI distortion field.

The displacement map for an optimized MRI treatment planning sequence was measured using a dedicated phantom in a 3 T MRI system.

To simulate the distortion aspects of a synthetic CT (electron density derived from MR images), the displacement map was applied to CT images, referred to as distorted CT images. A volumetric modulated arc prostate treatment plan was applied to the original CT and the distorted CT, creating a reference and a distorted CT dose distribution.

By applying the inverse of the displacement map to the distorted CT dose distribution, a dose distribution in the same geometry as the original CT images was created. For 10 prostate cancer patients, the dose difference between the reference dose distribution and inverse distorted CT dose distribution was analyzed in isodose level bins.

The mean magnitude of the geometric distortion was 1.97 mm for the radial distance of 200–250 mm from isocenter. The mean percentage dose

differences for all isodose level bins, were  $\leq 0.02\%$  and the radiotherapy structure mean volume deviations were  $< 0.2\%$ .

The method developed can quantify the dosimetric effects of MRI system specific distortion in a prostate MRI only radiotherapy workflow, separated from dosimetric effects originating from synthetic CT generation. No clinically relevant dose difference or structure deformation was found when 3D distortion correction and high acquisition bandwidth was used. The method could be used for any MRI sequence together with any anatomy of interest.

**Keywords:** MRI only, distortion, MRI radiotherapy, QA, synthetic CT, MRI treatment planning

(Some figures may appear in colour only in the online journal)

## 1. Introduction

The use of dedicated magnetic resonance imaging (MRI) scanners in radiotherapy centers has rapidly increased due to the superior soft tissue contrast of the MRI compared to computer tomography (CT) (Karlsson *et al* 2009, Blomqvist *et al* 2013). For external radiotherapy of prostate cancer, MRI can add clinical value to the target delineation process (Debois *et al* 1999, Jackson *et al* 2007). Simultaneous use of multimodal image information from CT and MRI often requires a registration of the images into a common frame of reference. This multimodal image registration between CT and MRI can result in an increased spatial uncertainty and therefore result in a deviation of the planned dose to the patient (Nyholm *et al* 2009). To avoid these uncertainties, techniques to provide electron density information from MRI have been developed, enabling a workflow excluding the CT. These workflows are often referred to as MRI only workflows where a synthetic CT image, created from MRI, replaces the CT. Several techniques to generate synthetic CTs has been proposed (Lambert *et al* 2011, Dowling *et al* 2012, Johansson *et al* 2012, Hsu *et al* 2013, Edmund *et al* 2014, Korhonen *et al* 2014, Andreasen *et al* 2015, Siversson *et al* 2015). The time, effort and resources spent per patient can also be reduced by excluding the CT from the radiotherapy workflow. This would also be beneficial as no ionizing radiation is used during radiotherapy planning.

The generation of a synthetic CT requires a field of view (FOV) covering the outer body contour for accurate treatment planning. Magnetic resonance (MR) images solely used for organ at risk (OAR)- and target delineation, does not require coverage of the outer body contour. These MR images are often acquired with a smaller FOV and used in conjunction with CT.

Geometric accuracy in the images used for radiotherapy treatment planning and positioning is essential and CT is considered as the gold standard in this context. Geometric distortion are known to exist in MRI and concerns regarding the use of MRI in radiotherapy has therefore been raised (Weygand *et al* 2016). The geometric distortion from MRI can be divided into system specific or patient/object specific distortion. The system specific distortion can originate from the non-linear gradients or from the non-homogenous static magnetic field (Bakker *et al* 1992, Doran *et al* 2005, Reinsberg *et al* 2005). The patient/object specific distortion can originate from magnetic susceptibility or from chemical shift effects (Bellon *et al* 1986, Bakker *et al* 1992).

The size of the geometric distortion originating from the non-linear gradients is increasing with increasing distance from the MRI magnetic isocenter (Wang *et al* 2004b, Walker *et al* 2014) and is therefore highly dependent on the size of the FOV used in the MRI acquisition.

It has been shown that the system specific geometric distortion are larger than the patient specific geometric distortion (Wang *et al* 2004b) and that non-linear gradients are the main source of geometric distortion (Baldwin *et al* 2007). The system specific geometric distortion in terms of non-linear gradients can in modern MR scanners be corrected in 2 dimensions (2D) using MRI vendor specific software (Wang *et al* 2004b). The availability of 3D correction of the non-linear gradients can be dependent on the acquisition sequence and acquisition parameters (Walker *et al* 2015). The system- and patient/object specific geometric distortion, in terms of induced non-homogeneities in the magnetic field, can be mitigated by the use of active magnetic field shimming (Weygand *et al* 2016).

Several methods have been proposed for measuring and mapping the system specific geometric distortion using dedicated phantoms (Koch *et al* 2003, Wang *et al* 2004a, Torfeh *et al* 2015). These phantoms often have some kind of visual signal markers at known spatial positions. To assess the geometric distortion, the marker positions in the MR images is compared with the physical location of the markers. Due to the need of large volume coverage special phantoms have been designed for that purpose (Tadic *et al* 2014, Torfeh *et al* 2015, Walker *et al* 2015, Huang *et al* 2016).

A geometric distortion of  $<2$  mm in the anatomy of interest is desired for the use of MRI in radiotherapy (Walker *et al* 2015, Weygand *et al* 2016). It was previously shown that residual geometric distortion, measured for a clinically relevant acquisition sequence together with 3D correction, were  $>2$  mm at distances  $>15$  cm from the isocenter (Walker *et al* 2015). It was also concluded that the origin of the geometric distortion were dominated by effects from non-linear gradients.

It is of broad and immediate interest to study the dosimetric effects from system specific geometric distortion in an MRI only radiotherapy workflow for prostate. Attempts has earlier been made to quantify how the geometric error in MRI propagates through the MRI only radiotherapy treatment planning process and how it affects the planned dose distribution (Mah *et al* 2002, Petersch *et al* 2004, Sun *et al* 2015).

The combined dosimetric impact from the system specific geometric distortion and a synthetic CT generation method was recently investigated (Bolard and Bulling 2016). Dosimetric errors originating from multiple previously published synthetic CT generation methods has also been studied (Kim *et al* 2015). In the clinical introduction of an MRI only radiotherapy treatment planning workflow it is important to solely quantify the dosimetric errors from geometric distortion. The methodology presented in this work enables separation of the dosimetric errors introduced by the system specific geometric distortion from the dosimetric errors originating from the synthetic CT generation itself.

The aim of this study was to (1) develop a method for MRI quality control and validation of clinical MRI sequences for the use in an MRI only radiotherapy workflow. (2) Evaluate the magnitude of the system specific geometric distortion in an MRI system and the impact on delineated structures. (3) Evaluate, using the developed method, the dosimetric impact of the system specific geometric distortion. This was done using a clinical MRI acquisition sequence, designed for an MRI only prostate radiotherapy workflow. We propose a methodology to apply the geometric distortion, originating from system related distortion in MRI, on pre-existing patient CT images.

## 2. Methods

The study was divided into three parts where the first part covered the measurement of geometric distortion in MRI, the generation of the displacement map and its application. The second part investigated the impact of geometric distortion on delineated radiotherapy structures (RT structures). The final part investigated the dosimetric impact of geometric distortion in MRI only treatment planning. The workflow of the method, illustrated in figure 2, was repeated for 10 prostate cancer patients (median age 75 years, median weight 84 kg and median length 173 cm), consecutive chosen from an ongoing *in vivo* MRI only treatment planning study.

### 2.1. Data acquisition, displacement map generation and its application

A commercially available 3D phantom designed to assess geometric accuracy for large FOVs (Spectronic Medical AB, Helsingborg, Sweden) was used in this study. The phantom contained 1177 spherical markers, with a marker diameter of 17 mm, filled with polyethylene glycol. The markers were organized in a grid on layers of extruded polystyrene which covered  $438.7 \times 346.0 \times 470.0 \text{ mm}^3$  (width (*W*), height (*H*), length (*L*)). The outer case of the phantom covered  $502 \times 404 \times 534 \text{ mm}^3$  (*W*, *H*, *L*) and was built by a layer of polyvinyl chloride (PVC), with a thickness of 1 mm around the phantom and 10 mm at the sides. Total weight of the phantom was 9.8 kg. A 3 T wide bore 70 cm MRI system (Discovery 750W, Software DV25R02-1549b, General Electric Healthcare, Milwaukee, WI) was selected for investigation. The phantom was scanned using the built in 2 channel body RF- multi transmit and receive coil (figure 1). The patient CT images used in this study were acquired with a Siemens Somatom Definition AS+ (Siemens Healthcare, Forchheim, Germany), slice thickness 3 mm, reconstructed diameter 500 mm, reconstructed in plane resolution  $0.98 \text{ mm} \times 0.98 \text{ mm}$ , peak kilo voltage output 120 kV, exposure time 500 ms, tube current 291 mA–677 mA.

For accurate and comparable mapping of the geometric distortion, arising principally from system specific geometric distortion, it was of importance that an identical MRI sequence was used for the phantom and the *in vivo* MRI only treatment planning study. The parameters used in the phantom MRI acquisition sequence were copied from the *in vivo* MRI acquisition sequence used in an ongoing Swedish multi-center study (MR-only prostate external radiotherapy, MR-OPERA). Due to the phantom size, the FOV and number of slices had to be adjusted. The *in vivo* study was performed with MRI acquisition sequence parameters described in table 1. The acquisition sequence for the phantom was considered and referred to as the optimized acquisition sequence.

The phantom was placed above the superior cavity on the MRI patient table, no table top was used (figure 1). The phantom was scanned with the optimized acquisition sequence. The displacement map was calculated using a cloud based commercial analysis software, GRADE version 1.0.32 (Spectronic Medical AB, Helsingborg, Sweden). GRADE automatically calculated the locations of the phantom markers in the MR images using a non-rigid image registration with a digital reference model of the phantom. Reference markers from the digital reference phantom model were generated by a rigid registration between the digital reference phantom model and the MR images using only the markers close to the isocenter, where geometric distortion were considered to be negligible. For each marker, the difference in location between the reference marker in the rigidly registered digital reference phantom model and the marker in the MR images were calculated. The displacement map, describing the difference in the location of the markers, were calculated using inverse mapping (Beier and Neely 1992) and generated with the pixel dimensions  $0.875 \text{ mm} \times 0.875 \text{ mm} \times 0.8741 \text{ mm}$ . A binary mask was applied to the displacement map to exclude peripheral sub-volumes with non-reliable displacement data.





**Figure 1.** The commercially available phantom from Spectronic Medical AB is designed to assess geometric accuracy. It was placed on the MRI table without table top. Lines on the phantom surface were used to align the phantom using the built in laser positioning system on the MRI.

Using an in-house built MATLAB software version R2015a (Mathworks Inc., Sherborn, MA, USA), the displacement map were linearly interpolated (down sampled) to match the pixel dimensions of the CT images. The magnitude of the geometric distortion for separate spatial directions were derived from, and equal to, the data from the displacement map. The relative orientation of the displacement map in space with respect to the CT images was taken into account before applying the displacement map to the CT. This was performed by a translation of the left–right and inferior–superior center of the displacement map to the DICOM user defined origin in the CT images (determined by the position of external skin markers, applied to the patient before CT scanning). A translation of the anterior–posterior center of the displacement map positioned the posterior anatomy of the CT images in the corresponding MRI geometry.

To simulate a clinical scan situation, and to avoid the use of unreliable displacement data originating from a peripheral part of the phantom, the displacement map was limited to 30 cm in the inferior–superior direction before being applied to the CT images. CT data outside of the 30 cm inferior–superior coverage was left undistorted. The displacement map was applied to the CT images as a geometric transformation using linear interpolation, from here on referred to as distCT images (figure 2).

To estimate the possible impact of object specific geometric distortion an additional MRI scan was performed on the phantom. The magnitude of the object specific geometric distortion in the optimized acquisition sequence was assumed to be proportional to the magnitude of the deviations in the static magnetic field and inversely proportional to the read out gradient strength (Weygand *et al* 2016). The deviations in the magnetic field, induced by the magnetic susceptibility of the phantom, was measured using the sequence IDEAL IQ (General Electric Healthcare, Milwaukee, WI), acquisition sequence parameters described in table 1. The clinical purpose of IDEAL IQ is *in vivo* fat quantification and depends on a correct assessment of the deviations in the static magnetic field, i.e. field mapping. The phantom volume field map was exported and the magnitude of the object specific geometric distortion was

**Table 1.** MRI acquisition sequence parameters for the acquisition sequences referred to in this study. The *in vivo* MRI acquisition sequence was used in an ongoing Swedish multi-center study (MR-only prostate external radiotherapy, MR-OPERA). The optimized acquisition sequence was used to scan the phantom to acquire the displacement map. The IDEAL IQ sequence was used to estimate the possible impact of object specific geometric distortion.

| Parameter                     | <i>In vivo</i> study  | Optimized acquisition sequence | IDEAL IQ                              |
|-------------------------------|-----------------------|--------------------------------|---------------------------------------|
| Coil                          | GE GEM anterior array | Built-in body                  | Built-in body                         |
| Sequence type                 | FSE <sup>a</sup>      | FSE <sup>a</sup>               | GRE                                   |
| 2D/3D                         | 2D                    | 2D                             | 3D                                    |
| Scan plane                    | Axial                 | Axial                          | Axial                                 |
| Freq. FOV                     | 448 mm <sup>b</sup>   | 448 mm <sup>b</sup>            | 500 mm <sup>b</sup>                   |
| Phase FOV                     | 314 mm <sup>c</sup>   | 403 mm <sup>c</sup>            | 500 mm                                |
| Scan matrix (freq. × phase)   | 640 × 512             | 640 × 512                      | 160 × 160                             |
| Recon. matrix (freq. × phase) | 1024 × 1024           | 1024 × 1024                    | 256 × 256                             |
| TR                            | 15 000.0 ms           | 15 000.0 ms                    | 6.0 ms                                |
| TE                            | 96 ms                 | 96 ms                          | 0.89, 1.63, 2.36, 3.10, 3.83, 4.56 ms |
| Slice thickness               | 2.5 mm                | 2.5 mm                         | 6.0 mm                                |
| Slice spacing                 | 0.0 mm                | 0.0 mm                         | 0.0 mm                                |
| Number of slices              | 88                    | 200                            | 100                                   |
| Number of echoes              | 1                     | 1                              | 6                                     |
| 3D geometry correction        | On                    | On                             | Off                                   |
| Bandwidth/pixel               | 390 Hz                | 390 Hz                         | 1389 Hz                               |
| Shimming method               | Auto (first order)    | Auto (first order)             | Auto (first order)                    |
| RF transmit mode              | Multi transmit        | Multi transmit                 | Quadrature                            |
| Acquisition time              | 7 min                 | 24 min                         | 6.5 min                               |

<sup>a</sup> Sequence used was fast recovery fast spin echo (FRFSE).

<sup>b</sup> Right–left direction.

<sup>c</sup> Anterior–posterior direction.

calculated given a read out gradient strength of 13.1 mT m<sup>-1</sup> (used in the optimized acquisition sequence).

## 2.2. Impact on RT structures

To assess the possible geometric distortion for target- and OAR anatomy, the impact on the delineated RT structures in the CT images was investigated. This was done using an in-house developed MATLAB software. By using the phantom marker locations from the detected markers in the MR images and the reference marker locations, supplied by Spectronic Medical AB and described in section 2.1, the displacement was calculated for all points in the RT structures. The relative orientation of the displacement data in space with respect to the RT structure was taken into account before calculating the displacement to the RT structure points, using the same orientation adaptations as described in section 2.1. The displacement was applied to the RT structure points using linear interpolation.

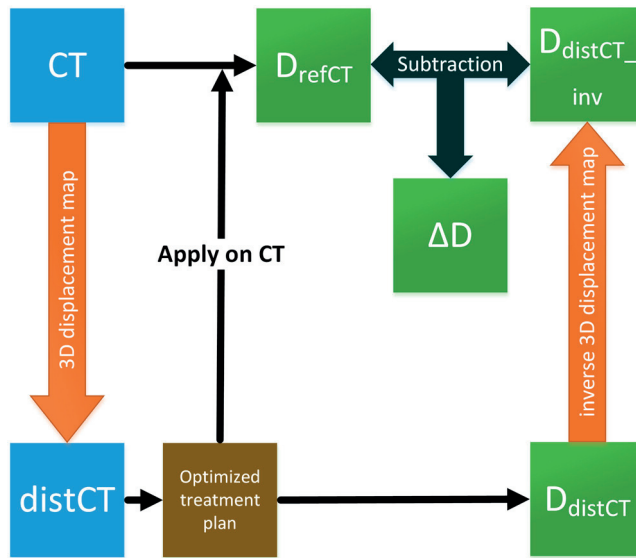


**Figure 2.** Flow chart of operations on CT images and dose distributions. CT = original CT images, distCT = distorted CT images,  $D_{\text{distCT}}$  = dose distribution from distCT,  $D_{\text{refCT}}$  = dose distribution from CT,  $D_{\text{distCT}_{\text{inv}}}$  = dose distribution from distCT with the inverse of the displacement map applied,  $\Delta D$  = dose difference  $D_{\text{refCT}} - D_{\text{distCT}_{\text{inv}}}$ .

The external surface of the RT structures were defined using additional RT structure points inserted in the areas encompassed by the first and last slice of the RT structure volume. A 3D boundary and its convex hull was calculated from the external surface, and the ratio of the volume within the 3D convex hull for distorted and original RT structures was calculated. In an absence of volume deviation, between original and distorted RT structure, a uniform translation and/or deformation with constant volume, of the whole RT structure could exist. This could give rise to deviation in the RT structure but no deviation in RT structure volume. To be able to detect such an event, the magnitude of the distortion in each spatial direction were calculated for each RT structure.

### 2.3. Treatment planning and dosimetric analysis

The RT structures for target and OAR were copied from the original CT to the distCT images. The RT structures were not deformed prior to copying them as the only objective was to enable the calculation of an acceptable treatment plan. A single arc 10 MV VMAT prostate treatment plan (78 Gy/39 fractions) were optimized on the distCT images using the Eclipse Treatment Planning system version 13.6 (Varian Medical Systems, Palo Alto, USA). The final dose distribution, referred to as  $D_{\text{distCT}}$ , was calculated using the Analytical Anisotropic Algorithm. The treatment plan was confirmed to fulfill the dose criteria in the conventional arm of the Swedish multicenter Phase III study of HYPO-fractionated Radiotherapy of intermediate risk localized Prostate Cancer (Widmark 2008). The created treatment plan was applied and recalculated with identical field setup and number of monitor units on the original CT images, creating a reference dose distribution  $D_{\text{refCT}}$ . This was performed in order to exclude any difference due to a slightly different plan delivery. Workflow is illustrated in figure 2. The dose

distributions  $D_{\text{distCT}}$  and  $D_{\text{refCT}}$  were linearly interpolated to match the pixel dimensions of the CT images.

The percentage dose difference between  $D_{\text{distCT}}$  and  $D_{\text{refCT}}$  was not calculated directly, since the distCT was considered geometrically incorrect. In an MRI only workflow, the dose distribution calculated on a synthetic CT (resembled by the distCT) is the dose distribution that would have been used for treatment. By applying the inverse of the displacement map to the  $D_{\text{distCT}}$  the planned dose distribution was transferred into a geometrically correct frame of reference which easily could be compared to the dose distribution of the original CT ( $D_{\text{refCT}}$ ), considered the gold standard. The inversely deformed dose distribution was referred to as  $D_{\text{distCT}_{\text{inv}}}$ . This is in analogy with the process of adaptive radiotherapy in a conventional CT based workflow using deformable image registration and dose warping (Veiga *et al* 2015).

The inverse of the displacement map (not to be confused with inverse mapping) was iteratively calculated using the function `InvertDisplacementFieldImageFilter` in Simple ITK 0.9.0 (open-source) together with ITK 4.7.2 (Yoo *et al* 2002). To verify the existence of an inverse to the displacement map and detect possible noninvertible displacement data, the value and the sign of the determinant of the displacement map Jacobian was evaluated for all patients. The value of zero corresponds to a nonexistent inverse and negative values are indicative of noninvertible and unrealistic deformations (Chen *et al* 2008, Veiga *et al* 2015). The inverse of the displacement map was applied using nearest neighbor interpolation in an in-house developed MATLAB software.

The percentage dose difference (normalized to 78 Gy), referred to as  $\Delta D$ , was calculated in the interval 0%–100% by subtracting  $D_{\text{refCT}}$  and  $D_{\text{distCT}_{\text{inv}}}$  in segmented binned isodose levels with a binning of 5%. The segmentations were determined from the  $D_{\text{refCT}}$  using binary masks. The mean and the standard deviation of the segmented  $\Delta D$  was calculated for each binary mask, i.e. for each binned isodose level, for each patient. The binning method was performed rather than using intentionally distorted RT structures or re-delineated RT structures in the distCT. A manual re-delineation in the distCT images would give rise to additional uncertainties as a result. The workflow is illustrated in figure 2.

### 3. Results

#### 3.1. Geometric distortion measurements

The mean, minimum and maximum magnitude of the phantom geometric distortion in separate spatial directions, for complete and limited phantom volumes is presented in table 2. The mean magnitude for the geometric distortion was largest for the inferior–superior direction. This behavior was true in both the limited (30 cm inferior–superior) and the complete phantom volume. The mean and maximum magnitude of the phantom geometric distortion as a function of radial distance from the isocenter of the MRI, is presented for the complete phantom volume in table 3. The mean and maximum magnitude of the deviations in the static magnetic field, together with the calculated magnitude of the object specific geometric distortion for the complete phantom volume, is displayed in table 4.

#### 3.2. Impact on RT structures

The mean volume ratio between distorted RT structures and original RT structures among all patients in the study was  $1.00 \pm 0.00$  for CTV, PTV, femoral head left, femoral head right, bladder and rectum. For the RT structure Body it was  $1.01 \pm 0.00$ .

**Table 2.** Mean, minimum (min) and maximum (max) magnitude of the phantom geometric distortion for separate spatial directions, for complete and limited (30 cm inferior–superior) phantom volumes. Data was binary masked for both phantom volumes to exclude peripheral sub-volumes with non-reliable displacement data. Data was not interpolated to match the pixel dimensions of the CT images.

|                         | Left–right (mm) |      |       | Anterior–posterior (mm) |      |       | Inferior–superior (mm) |      |      |
|-------------------------|-----------------|------|-------|-------------------------|------|-------|------------------------|------|------|
|                         | Mean            | Min  | Max   | Mean                    | Min  | Max   | Mean                   | Min  | Max  |
| Limited phantom volume  | 0.082 ± 0.19    | 0.00 | 3.60  | 0.070 ± 0.16            | 0.00 | 3.51  | 0.36 ± 0.76            | 0.00 | 9.67 |
| Complete phantom volume | 0.13 ± 0.37     | 0.00 | 12.28 | 0.10 ± 0.33             | 0.00 | 12.58 | 0.47 ± 0.96            | 0.00 | 9.67 |

**Table 3.** Mean and maximum magnitude of the phantom geometric distortion, complete phantom volume, as a function of radial distance from the isocenter of the MRI. Data was binary masked to exclude peripheral sub-volumes with non-reliable displacement data. Data was not interpolated to match the pixel dimensions of the CT images.

| Radial distance from isocenter and distortion (mm) |      |         |      |         |      |         |      |
|--|------|---------|------|---------|------|---------|------|
| <100   |      | 100–150 |      | 150–200 |      | 200–250 |      |
| Mean   | Max  | Mean    | Max  | Mean    | Max  | Mean    | Max  |
| 0.17   | 0.43 | 0.3     | 0.82 | 0.57    | 1.85 | 1.97    | 7.86 |

**Table 4.** Mean and maximum magnitude of deviations in the magnetic field (ppm) for the phantom volume, as a function of radial distance from the isocenter of the MRI, measured with the IDEAL IQ sequence. The calculated magnitude of the object specific geometric distortion for the phantom using the optimized sequence is displayed in parenthesis.

| Measured deviation of the magnetic field (ppm) and calculated distortion (mm) at different radial distances from isocenter (mm) |             |              |             |             |              |             |              |
|---|-------------|--------------|-------------|-------------|--------------|-------------|--------------|
| <100  |             | 100–150      |             | 150–200     |              | 200–250     |              |
| Mean  | Max         | Mean         | Max         | Mean        | Max          | Mean        | Max          |
| 0.36 (0.082)  | 3.29 (0.75) | 0.37 (0.084) | 2.79 (0.64) | 0.85 (0.20) | 13.03 (2.98) | 1.81 (0.41) | 19.11 (4.38) |

The mean magnitude of the distortion in the RT structures among all patients in left–right and inferior–superior direction was  $0.00 \pm 0.00$  mm for CTV, PTV, femoral head left, femoral head right, bladder and rectum. For the anterior–posterior direction it was  $0.01 \pm 0.00$  mm. For the RT structure Body it was  $0.13 \pm 0.04$  mm,  $0.09 \pm 0.05$  mm and  $0.44 \pm 0.09$  mm for the left–right, anterior–posterior and inferior–superior direction.

### 3.3. Development of the method and dosimetric impact

A method to assess dosimetric impact of system specific distortion in an MRI only workflow was developed. The mean number of pixels in the distortion field having a negative determinant of its Jacobian among all patients were 0.008%. The corresponding pixel positions were at the most peripheral part of the phantom data. No pixels had a determinant of its Jacobian equal to zero.

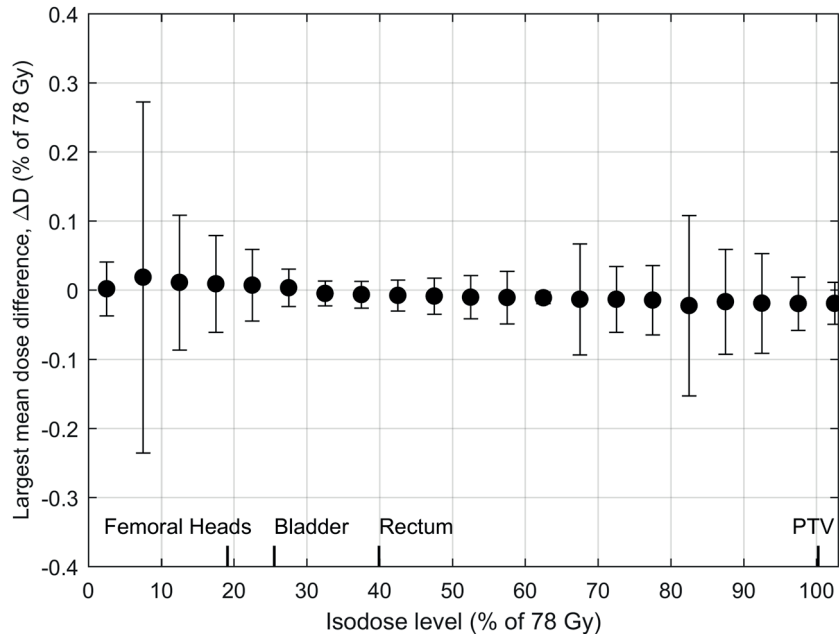


**Figure 3.** Largest mean percentage dose differences among all patients in the study (solid points). At each isodose level, the largest mean percentage dose difference ( $\pm 1$  standard deviation) among all patients in the study is shown. CT dose distribution is used as reference. The average of the median percentage dose to target and OAR among all patients in the study is shown (line markers on the isodose level axis).

The largest mean percentage dose difference for each isodose level and the average of the median percentage dose to target and OAR (among all patients in the study) is shown in figure 3. The largest negative and positive mean percentage dose difference for all isodose levels were  $-0.02\% \pm 0.13\%$  (isodose level bin 80%–85%) and  $0.02\% \pm 0.25\%$  (isodose level bin 5%–10%).

#### 4. Discussion

The work performed in this study introduced a method to assess dosimetric impact of system specific distortion in an MRI only workflow. The method was not influenced by any errors that might solely originate from the assignment of Hounsfield units in a synthetic CT generation.

The system specific distortion for an MRI only optimized sequence was assessed using a phantom. As expected, the distortion was greater with increasing radius from the isocenter of the MRI (Torfeh *et al* 2015, Weygand *et al* 2016). The distortion data in this study were also in good agreement with a previous study using an identical pulse sequence (Torfeh *et al* 2015).

A possible interference in the measurement of the system specific distortion was object specific distortion, determined by the shape and magnetic susceptibility of the phantom material. We estimated the susceptibility effects induced by the phantom by the IDEAL IQ sequence. Using this sequence the effects from the phantom and the static magnetic field were added and could not be separated, which was an inherent limitation of the method. However, in spite of this, the measured deviations were small. Furthermore, patient specific distortions were beyond the scope of this study. The calculated mean magnitude of the object specific

geometric distortion was  $<0.5$  mm for all radial distances of  $<250$  mm from the isocenter and was considered negligible for the purpose of this work. The results showed that the system specific geometric distortion were larger than the object specific geometric distortion and that non-linear gradients were the main source of the geometric distortion.

The size of the mean deviation in RT structure volume ratios were consistent with the mean magnitude of the distortion in each spatial direction for each RT structure, i.e. a larger deviation in a RT structure volume was associated with a larger distortion. This corresponded to a non-distorted anatomy of the target and OAR in the distCT images. It was previously concluded that the mean distortion for all RT structures (body excluded) for a simulated prostate MRI only treatment workflow, was  $<1$  mm, both with and without 3D distortion correction (Sun *et al* 2015). Our results were similar.

The method developed in this work quantified the dosimetric effects from geometric distortion in MRI only treatment planning for prostate. Validation of MRI only treatment planning, using synthetically generated CTs and conventional CTs, includes several uncertainties such as repositioning between multiple modalities, bladder- and rectum filling, and body- and organ structure changes. Additionally, the synthetic CT generation method itself can introduce an error. In previous studies specifically aimed at the assessment of dosimetric errors originating from geometric distortion of the MRI system, synthetic CTs with bulk density assignment has been used (Sun *et al* 2015, Bolard and Bulling 2016).

Earlier studies aimed to study the dose difference in generated synthetic CTs compared to conventional CTs for prostate reports a mean dose difference to target of less than 2% (Lambert *et al* 2011, Dowling *et al* 2012, Kapanen *et al* 2013, Korhonen *et al* 2014, Siverson *et al* 2015). This is higher than in the present study. This is to be expected as our method, in contrary to the studies above, focus on the uncertainties from the system specific geometric distortion and does not rely on bulk density assignment. Furthermore, dose warping (Veiga *et al* 2015) has been used in our method and to the best of our knowledge, this is the first time in literature that dose warping has been used to assess the effects of distortion in an MRI only workflow.

However, in contrast to dose warping between cone beam CT and CT, our method does not rely on deformable image registration between image sets. Instead, the inverse of the measured distortion field was used. The accuracy of the approach was ensured by investigating the properties of the Jacobian. Furthermore, interpolation effects were minimized by using a high spatial resolution for all matrices (same as CT). When adopting our dose warping approach, we recommend the actions above to be performed. If the image distortion is small (i.e. central part of the images), the error introduced when simply comparing the two dose matrices without any dose warping would be small. However, this is not the case when larger image distortion exists (e.g. peripheral part of the images).

The natural body processes occurring during the MRI scan of a patient will affect the geometry of the synthetic CT. This is important to consider when evaluating the dosimetric deviations between a CT and a synthetic CT. Natural bladder filling will lead to an increase in bladder volume. A study performed, under MRI scan conditions similar to those of an MRI only prostate treatment planning session, showed an increase in bladder volume in the study subjects ranging from 3% to 101% (McBain *et al* 2009). From our results, using an optimized acquisition protocol, it can therefore be expected that natural bladder volume changes is significantly larger than the bladder volume changes induced by system specific geometric distortion.

For quantification of the percentage dose difference, an analysis in segmented binned isodose levels was performed. This eliminated the need for intentionally distorting the RT structures to fit the distorted anatomy of the distCT images. In previous studies this issue has

been overlooked for the dosimetric evaluation by merely copying the RT structures between the MR images and CT images (Chen *et al* 2004a, 2004b). In the present work it was shown that the influence on the RT structures due to geometric distortion from the optimized sequence were insignificant. This may not always be the case when evaluating the geometric distortion for other MRI acquisition sequences. Dose-volume histogram (DVH) analysis was therefore not included in this work as a part of the evaluation. Furthermore, in contrast to the use of DVH analysis, the segmented binned isodose levels provides information on the dose difference for a continuous range of isodose levels.

To conclude, it is of importance that the MRI acquisition sequence used for any MRI only treatment planning are validated. A method is presented in this work which may be used for this type of validation.

## 5. Conclusions

A method was developed to assess the dosimetric impact of system specific geometric distortion. The dosimetric impact was not influenced by any errors that could originate from the assignment of Hounsfield units in a synthetic CT generation method. It required clinical CT image material from the anatomy of interest and the production of a displacement map, originating from a measurement of a dedicated phantom designed to assess geometric accuracy in MRI. Both of these requirements should be feasible to satisfy in a clinic aiming to introduce MRI only treatment planning. The developed method enabled quantification of the dosimetric effects of MRI system specific distortion for prostate MRI only radiotherapy treatment planning. The dosimetric effect and impact on delineated RT structures were negligible. The method has the potential to be used for any MRI acquisition sequence together with any anatomy of interest.

## Acknowledgments

This work was partially funded by Vinnova, Sweden's innovation agency, through the national project Gentle Radiotherapy with grant number 2014-00743 and 'Allmänna sjukhusets i Malmö Stiftelse för bekämpande av cancer'. Ethics approval was requested for 'Validering av MR som underlag för strålbehandling' and given 2015-10-19 by Regionala etikprövningsnämnden in Umeå, Avdelningen för medicinsk forskning, diary number 2015-311-31M.

## References

- Andreasen D, Van Leemput K, Hansen R H, Andersen J A and Edmund J M 2015 Patch-based generation of a pseudo CT from conventional MRI sequences for MRI-only radiotherapy of the brain *Med Phys* **42** 1596–605
- Bakker C J, Moerland M A, Bhagwandien R and Beersma R 1992 Analysis of machine-dependent and object-induced geometric distortion in 2DFT MR imaging *Magn. Reson. Imaging* **10** 597–608
- Baldwin L N, Wachowicz K, Thomas S D, Rivest R and Fallone B G 2007 Characterization, prediction, and correction of geometric distortion in 3 T MR images *Med. Phys.* **34** 388–99
- Beier T and Neely S 1992 Feature-based image metamorphosis *SIGGRAPH Comput. Graph.* **26** 35–42
- Bellon E M, Haacke E M, Coleman P E, Sacco D C, Steiger D A and Gangarosa R E 1986 MR artifacts: a review *AJR Am. J. Roentgenol.* **147** 1271–81
- Blomqvist L, Bäck A, Ceberg C, Enblad G, Frykholm G, Johansson M, Olsson L and Zackrisson B 2013 MR in radiotherapy—an important step towards personalized treatment? *Report from the SSM's Scientific Council on Ionizing Radiation within Oncology SSM*



- Bolard G and Bulling S 2016 MO-FG-CAMPUS-JeP2-03: clinical commissioning of MR-only prostate treatment planning workflow *Med. Phys.* **43** 3721
- Chen L, Price R A Jr, Nguyen T B, Wang L, Li J S, Qin L, Ding M, Palacio E, Ma C M and Pollack A 2004a Dosimetric evaluation of MRI-based treatment planning for prostate cancer *Phys. Med. Biol.* **49** 5157–70
- Chen L, Price R A Jr, Wang L, Li J, Qin L, Mcneeley S, Ma C M, Freedman G M and Pollack A 2004b MRI-based treatment planning for radiotherapy: dosimetric verification for prostate IMRT *Int. J. Radiat. Oncol. Biol. Phys.* **60** 636–47
- Chen M, Lu W, Chen Q, Ruchala K J and Olivera G H 2008 A simple fixed-point approach to invert a deformation field *Med. Phys.* **35** 81–8
- Debois M *et al* 1999 The contribution of magnetic resonance imaging to the three-dimensional treatment planning of localized prostate cancer *Int. J. Radiat. Oncol. Biol. Phys.* **45** 857–65
- Doran S J, Charles-Edwards L, Reinsberg S A and Leach M O 2005 A complete distortion correction for MR images: I. Gradient warp correction *Phys. Med. Biol.* **50** 1343–61
- Dowling J A, Lambert J, Parker J, Salvado O, Fripp J, Capp A, Wratten C, Denham J W and Greer P B 2012 An atlas-based electron density mapping method for magnetic resonance imaging (MRI)-alone treatment planning and adaptive MRI-based prostate radiation therapy *Int. J. Radiat. Oncol. Biol. Phys.* **83** e5–11
- Edmund J M, Kjer H M, Van Leemput K, Hansen R H, Andersen J A and Andreasen D 2014 A voxel-based investigation for MRI-only radiotherapy of the brain using ultra short echo times *Phys. Med. Biol.* **59** 7501–19
- Hsu S H, Cao Y, Huang K, Feng M and Balter J M 2013 Investigation of a method for generating synthetic CT models from MRI scans of the head and neck for radiation therapy *Phys. Med. Biol.* **58** 8419–35
- Huang K C, Cao Y, Baharom U and Balter J M 2016 Phantom-based characterization of distortion on a magnetic resonance imaging simulator for radiation oncology *Phys. Med. Biol.* **61** 774–90
- Jackson A S, Reinsberg S A, Sohaib S A, Charles-Edwards E M, Mangar S A, South C P, Leach M O and Dearnaley D P 2007 Distortion-corrected T2 weighted MRI: a novel approach to prostate radiotherapy planning *Br. J. Radiol.* **80** 926–33
- Johansson A, Karlsson M, Yu J, Asklund T and Nyholm T 2012 Voxel-wise uncertainty in CT substitute derived from MRI *Med. Phys.* **39** 3283–90
- Kapanen M, Collan J, beule A, Seppala T, Saarihahti K and Tenhunen M 2013 Commissioning of MRI-only based treatment planning procedure for external beam radiotherapy of prostate *Magn. Reson. Med.* **70** 127–35
- Karlsson M, Karlsson M G, Nyholm T, Amies C and Zackrisson B 2009 Dedicated magnetic resonance imaging in the radiotherapy clinic *Int. J. Radiat. Oncol. Biol. Phys.* **74** 644–51
- Kim J, Garbarino K, Schultz L, Levin K, Movsas B, Siddiqui M S, Chetty I J and Glide-Hurst C 2015 Dosimetric evaluation of synthetic CT relative to bulk density assignment-based magnetic resonance-only approaches for prostate radiotherapy *Radiat. Oncol.* **10** 239
- Koch N, Liu H H, Olsson L E and Jackson E F 2003 Assessment of geometrical accuracy of magnetic resonance images for radiation therapy of lung cancers *J. Appl. Clin. Med. Phys.* **4** 352–64
- Korhonen J, Kapanen M, Keyrilainen J, Seppala T and Tenhunen M 2014 A dual model HU conversion from MRI intensity values within and outside of bone segment for MRI-based radiotherapy treatment planning of prostate cancer *Med. Phys.* **41** 011704
- Lambert J *et al* 2011 MRI-guided prostate radiation therapy planning: investigation of dosimetric accuracy of MRI-based dose planning *Radiother. Oncol.* **98** 330–4
- Mah D, Steckner M, Hanlon A, Freedman G, Milestone B, Mitra R, Shukla H, Movsas B, Horwitz E, Vaisanen P P and Hanks G E 2002 MRI simulation: effect of gradient distortions on three-dimensional prostate cancer plans *Int. J. Radiat. Oncol. Biol. Phys.* **53** 757–65
- McBain C A, Khoo V S, Buckley D L, Sykes J S, Green M M, Cowan R A, Hutchinson C E, Moore C J and Price P M 2009 Assessment of bladder motion for clinical radiotherapy practice using cine-magnetic resonance imaging *Int. J. Radiat. Oncol. Biol. Phys.* **75** 664–71
- Nyholm T, Nyberg M, Karlsson M G and Karlsson M 2009 Systematisation of spatial uncertainties for comparison between a MR and a CT-based radiotherapy workflow for prostate treatments *Radiat. Oncol.* **4** 54
- Petersch B, Bogner J, Fransson A, Lorang T and Potter R 2004 Effects of geometric distortion in 0.2 T MRI on radiotherapy treatment planning of prostate cancer *Radiother. Oncol.* **71** 55–64

- Reinsberg S A, Doran S J, Charles-Edwards E M and Leach M O 2005 A complete distortion correction for MR images: II. Rectification of static-field inhomogeneities by similarity-based profile mapping *Phys. Med. Biol.* **50** 2651–61
- Siverssón C, Nordström F, Nilsson T, Nyholm T, Jonsson J, Gunnlaugsson A and Olsson L E 2015 Technical note: MRI only prostate radiotherapy planning using the statistical decomposition algorithm *Med. Phys.* **42** 6090–7
- Sun J *et al* 2015 MRI simulation: end-to-end testing for prostate radiation therapy using geometric pelvic MRI phantoms *Phys. Med. Biol.* **60** 3097–109
- Tadic T, Jaffray D A and Stanescu T 2014 Harmonic analysis for the characterization and correction of geometric distortion in MRI *Med. Phys.* **41** 112303
- Torfeh T, Hammoud R, McGarry M, Al-Hammadi N and Perkins G 2015 Development and validation of a novel large field of view phantom and a software module for the quality assurance of geometric distortion in magnetic resonance imaging *Magn. Reson. Imaging* **33** 939–49
- Veiga C, Lourenco A M, Mouinuddin S, Van Herk M, Modat M, Ourselin S, Royle G and McClelland J R 2015 Toward adaptive radiotherapy for head and neck patients: uncertainties in dose warping due to the choice of deformable registration algorithm *Med. Phys.* **42** 760–9
- Walker A, Liney G, Holloway L, Dowling J, Rivest-Henault D and Metcalfe P 2015 Continuous table acquisition MRI for radiotherapy treatment planning: distortion assessment with a new extended 3D volumetric phantom *Med. Phys.* **42** 1982–91
- Walker A, Liney G, Metcalfe P and Holloway L 2014 MRI distortion: considerations for MRI based radiotherapy treatment planning *Australas. Phys. Eng. Sci. Med.* **37** 103–13
- Wang D, Doddrell D M and Cowin G 2004a A novel phantom and method for comprehensive 3-dimensional measurement and correction of geometric distortion in magnetic resonance imaging *Magn. Reson. Imaging* **22** 529–42
- Wang D, Strugnell W, Cowin G, Doddrell D M and Slaughter R 2004b Geometric distortion in clinical MRI systems Part I: evaluation using a 3D phantom *Magn. Reson. Imaging* **22** 1211–21
- Weygand J, Fuller C D, Ibbott G S, Mohamed A S, Ding Y, Yang J, Hwang K P and Wang J 2016 Spatial precision in magnetic resonance imaging-guided radiation therapy: the role of geometric distortion *Int. J. Radiat. Oncol. Biol. Phys.* **95** 1304–16
- Widmark A 2008 *Phase III study of Hypofractionated Radiotherapy of Intermediate Risk Localised prostate Cancer* (Online). BioMed Central. Available: [www.isrctn.com/ISRCTN45905321](http://www.isrctn.com/ISRCTN45905321) (Accessed 25 July 2016)
- Yoo T S, Ackerman M J, Lorensen W E, Schroeder W, Chalana V, Aylward S, Metaxas D and Whitaker R 2002 Engineering and algorithm design for an image processing Api: a technical report on ITK—the insight toolkit *Stud. Health Technol. Inform.* **85** 586–92

Paper II





Physics Contribution

# MR-OPERA: A Multicenter/Multivendor Validation of Magnetic Resonance Imaging—Only Prostate Treatment Planning Using Synthetic Computed Tomography Images



Emilia Persson, MSc,<sup>\*,†</sup> Christian Gustafsson, MSc,<sup>\*,†</sup>  
Fredrik Nordström, PhD,<sup>‡</sup> Maja Sohlín, MD, PhD,<sup>‡</sup>  
Adalsteinn Gunnlaugsson, MD, PhD,<sup>\*</sup> Karin Petruson, MD, PhD,<sup>§</sup>  
Niina Rintelä, MSc,<sup>||</sup> Kristoffer Hed, BSc,<sup>||</sup>  
Lennart Blomqvist, MD, PhD,<sup>¶,#,\*\*</sup> Björn Zackrisson, MD, PhD,<sup>¶</sup>  
Tufve Nyholm, PhD,<sup>¶,††</sup> Lars E. Olsson, PhD,<sup>†</sup> Carl Siversson, PhD,<sup>‡‡</sup>  
and Joakim Jonsson, PhD<sup>¶</sup>

<sup>\*</sup>Department of Hematology, Oncology, and Radiation Physics, Skåne University Hospital, Lund;

<sup>†</sup>Department of Medical Physics, Lund University, Malmö; Departments of <sup>‡</sup>Medical Physics and Biomedical Engineering, and <sup>§</sup>Oncology, Sahlgrenska University Hospital, Gothenburg; <sup>||</sup>Medical Radiation Physics and Nuclear Medicine, and <sup>\*\*</sup>Department of Diagnostic Radiology, Karolinska University Hospital, Stockholm; <sup>¶</sup>Department of Radiation Sciences, Umeå University, Umeå;

<sup>#</sup>Department of Molecular Medicine and Surgery, Karolinska Institutet, Stockholm; <sup>††</sup>Department of Immunology, Genetics, and Pathology, Uppsala University, Uppsala; and <sup>‡‡</sup>Spectronic Medical AB, Helsingborg, Sweden

Received Nov 1, 2016, and in revised form May 12, 2017. Accepted for publication Jun 7, 2017.

## Summary

This study aimed to validate a commercially available software for MR to synthetic computed tomography (CT) conversion for use in an MRI-only prostate external radiation therapy workflow.

**Purpose:** To validate the dosimetric accuracy and clinical robustness of a commercially available software for magnetic resonance (MR) to synthetic computed tomography (sCT) conversion, in an MR imaging—only workflow for 170 prostate cancer patients.

**Methods and Materials:** The 4 participating centers had MriPlanner (Spectronic Medical), an atlas-based sCT generation software, installed as a cloud-based service. A T2-weighted MR sequence, covering the body contour, was added to the clinical protocol. The MR images were sent from the MR scanner workstation to the

Reprint requests to: Emilia Persson, MSc, Department of Hematology, Oncology, and Radiation Physics, Skåne University Hospital, Klinikgatan 5, 22185 Lund, Sweden. Tel: (+46) (0) 72-509-00-75; E-mail: Emilia.Persson@skane.se

Funding: This work was partially funded by Vinnova, Sweden's innovation agency, through the national project Gentle Radiotherapy with

grant number 2016-03847, 'Allmänna sjukhusets i Malmö Stiftelse för bekämpande av cancer', The Swedish testbed for innovative radiation therapy and Skånes Universitetssjukhus stiftelser.

Conflict of interest: F.N. and C.S. are employed by Spectronic Medical.

**Acknowledgment**—The authors thank the clinical staff at the centers for their excellent help throughout the study.

A multicenter study design was used to compare CT-based treatment plans with recalculated synthetic CT plans for 170 prostate cancer patients. The software was found to be robust for a variety of field strengths, vendors, and treatment techniques.

MriPlanner platform. The sCT was automatically returned to the treatment planning system. Four MR scanners and 2 magnetic field strengths were included in the study. For each patient, a CT-treatment plan was created and approved according to clinical practice. The sCT was rigidly registered to the CT, and the clinical treatment plan was recalculated on the sCT. The dose distributions from the CT plan and the sCT plan were compared according to a set of dose-volume histogram parameters and gamma evaluation. Treatment techniques included volumetric modulated arc therapy, intensity modulated radiation therapy, and conventional treatment using 2 treatment planning systems and different dose calculation algorithms.

**Results:** The overall (multicenter/multivendor) mean dose differences between sCT and CT dose distributions were below 0.3% for all evaluated organs and targets. Gamma evaluation showed a mean pass rate of 99.12% (0.63%, 1 SD) in the complete body volume and 99.97% (0.13%, 1 SD) in the planning target volume using a 2%/2-mm global gamma criteria.

**Conclusions:** Results of the study show that the sCT conversion method can be used clinically, with minimal differences between sCT and CT dose distributions for target and relevant organs at risk. The small differences seen are consistent between centers, indicating that an MR imaging-only workflow using MriPlanner is robust for a variety of field strengths, vendors, and treatment techniques. © 2017 The Author(s). Published by Elsevier Inc. This is an open access article under the CC BY-NC-ND license (<http://creativecommons.org/licenses/by-nc-nd/4.0/>).

## Introduction

The limited soft tissue contrast of computed tomography (CT) images makes definition of the target and organs at risk (OARs) difficult for radiation therapy treatment planning. This has led to the widespread introduction of magnetic resonance imaging (MRI) into radiation therapy clinics during recent years (1). Magnetic resonance imaging exhibits excellent soft tissue contrast and has been shown to increase accuracy in target definitions for several tumor sites, as well as to add value to the delineation of OARs (2-6). Although MR images have an important role in the delineation process, CT imaging has retained its position as the imaging modality of choice for the treatment planning process (dose calculation and generation of images for patient positioning). This is mainly attributed to the high geometric accuracy of CT and its unique relationship to the attenuation of the imaged tissue, which is needed for inhomogeneity-corrected dose calculations. To accomplish this multimodal approach of treatment preparation, image registration has been widely used to transfer MR-based treatment volumes to the CT images used for treatment planning.

There are, however, several disadvantages with this workflow. The cost of using multiple imaging modalities in the preparation steps of radiation therapy is not insignificant, and the geometric uncertainty associated with the co-registration of MR and CT images acquired at different time points and at different imaging devices may be significant. In absolute numbers the uncertainties in CT-MR registration has been estimated to be 2 mm (1 SD) (7). Systematic registration errors will propagate through the treatment planning process and cause a systematic error

that will persist throughout the entire treatment. In contrast to random errors, such as those introduced by day-to-day positioning, the systematic errors are more serious and could lead to a displacement of the dose distribution (8). This has led several groups to investigate the possibilities of using MRI only for both delineations and treatment planning, under the assumption that the uncertainty in the identification of the markers based on MR data will be smaller than the uncertainty in the co-registration between CT and MR.

To allow dose calculations based on MRI, methods have been developed to convert MR images to images similar to CT, often denoted as synthetic CT (sCT) images. Several methods have been proposed: (1) direct conversion of pixel values using specialized sequences, such as ultra-short echo time imaging in combination with other sequences (9-11); (2) population atlas techniques, which use deformable image registration to warp a label image to an MR image (12-15); or (3) a voxel-based affine registration approach (16). Further, manual and semi-manual segmentation techniques to divide an MR image into tissue classes that are assigned electron densities exist (17-20). All of these techniques have shown promising results, with point or mean dose deviations to the target in the vicinity of 1%. These studies have often been limited in terms of size of the patient cohorts and are mostly single-center studies, with a single scanner and field strength, using in-house-developed software. This has limited the widespread adoption of MRI-only treatment planning.

In this MR-Only Prostate External Radiotherapy (MR-OPERA) study, the aim was to verify the dosimetric accuracy and robustness to clinical input data of a commercially available software for MR to sCT conversion of the male pelvis. The

atlas-based generation algorithm used in the software has previously been described (21). The study included 170 patients from 4 different university hospitals in Sweden, using different MR vendors and field strengths.

## Methods and Materials

### Patients

From October 2015 to June 2016, a total of 170 consecutive patients were included in a non-interventional, prospective, multicenter study, approved by the Umeå Regional ethics review board. Inclusion criteria were patients referred to MR and CT imaging before prostate radiation therapy. No height, weight, or age restrictions were imposed; however, patients with large surgical implants such as hip prosthesis were not eligible. Study participation did not affect the prescribed treatment, because the doses were recalculated to simulate MRI-only treatment.

### Imaging

The conversion software used in the study required a T2-weighted MR image with large field of view (FOV), covering the entire patient contour, with sufficient coverage for treatment planning in the cranio-caudal direction. Further, the sequence was required to be corrected for geometric distortions and acquired with sufficient bandwidth to limit the impact of these. Such sequence was added to the standard protocol consisting of target and marker localization sequences (scan time 30–45 minutes). The study sequence was limited to approximately 5 minutes. All centers imaged the patients in treatment position on both CT and MR, using a flat tabletop and immobilization with ankle and knee support. Magnetic resonance and CT imaging parameters are specified in Tables 1 and 2. The RF (radiofrequency) coils, 18-channel body 18 long (used for the 2 Siemens scanners) and 16-channel GEM Anterior Array (used for the 2 GE scanners), were centered over the symphysis on a stiff coil bridge. Quality assurance of the MR scanners was performed according to local practice at each center.

### sCT generation and treatment planning

The algorithm used in the conversion software MriPlanner (Spectronic Medical, Helsingborg, Sweden) has previously

been described (21). The algorithm is based on an automated atlas-based conversion method that requires T2-weighted MR images for sCT generation. Since the previous publication the software has been updated with a new training data set, acquired at a single center. In practice the software integrates into the clinical workflow by configuring a Digital Imaging in Communications and Medicine (DICOM) node within the hospital, which receives and anonymizes patient data and generates a key. The anonymized patient data is then automatically uploaded to a cloud-based conversion service, which generates the sCT and returns it to the DICOM node. The patient information is restored using the previously generated key, and the sCT is automatically returned to the radiation therapy department for treatment planning.

One modification of the MriPlanner workflow was needed for this study: the CT was also uploaded to the cloud service so that the generated sCT could be rigidly registered according to bony anatomy to the CT before replanning. The sCT was returned with the same resolution as the CT. This additional step was needed to account for patient rotations between MR and CT. A simple treatment planning isocenter translation would result in a rotated dose distribution, which would limit the possibility of accurate comparisons.

A CT-based treatment plan was created according to clinical practice at each clinic (for technical details see Table 3). The CT plan was transferred to the rigidly registered sCT, and the dose was recalculated, resulting in 2 plans with identical beam setup. Target volumes and OARs were transferred from the CT to the sCT, whereas separate external contours were created for the CT and sCT images.

### Evaluation

The dose-volume histogram (DVH) evaluation was carried out in CERR (version 4.6), a computational environment for radiation therapy research (22), between the original CT plan and the recalculated sCT plan, using the resulting dose matrices and CT structures. The protocol from the conventional arm in the Swedish multicenter phase 3 study of hypo-fractionated radiation therapy of intermediate-risk localized prostate cancer (23) was used as a reference for the dose-volume criteria to be evaluated. Gamma evaluation (24) was carried out using Medical Interactive Creative Environment, version 0.3.0.209 (available at [www.gentleradiotherapy.se](http://www.gentleradiotherapy.se)) (25) within the complete volumes,

**Table 1** Imaging devices used at all centers

| Center (no. of patients) | CT scanner   | MR scanner and field strength |
|--------------------------|--|-------------------------------|
| Center 1 (68)            | Siemens Somatom Definition AS+                       | GE Discovery, 750w 3.0T       |
| Center 2 (54)            | Philips Brilliance Big Bore                          | GE Signa, PET/MR 3.0T         |
| Center 3 (42)            | Toshiba Aquilion LB                                  | Siemens Aera 1.5T             |
| Center 4 (6)             | Siemens Somatom Definition AS+ or GE LightSpeed RT16 | Siemens Skyra 3.0T            |

Abbreviations: MR = magnetic resonance; PET = positron emission tomography.

**Table 2** Scan protocol parameters for the T2-weighted MR used for sCT generation

| Parameter                          | MR scan             | CT      |
|------------------------------------|---------------------|---------|
| Slice thickness (mm)               | 2.5-3.0             | 2.5-3.0 |
| kV                                 |                     | 120     |
| Resolution x/y plane (mm)          |                     | 1/1     |
| Resolution x/y plane (recon.) (mm) | 0.44-0.88/0.44-0.88 |         |
| Slice gap (mm)                     | 0                   |         |
| Distortion correction              | On                  |         |
| Bandwidth 3T (Hz/pixel)            | 244-390             |         |
| Bandwidth 1.5T (Hz/pixel)          | 215                 |         |
| FOV (mm)                           | 448                 |         |
| No. of slices                      | 88-100              |         |
| Time to echo (ms)                  | 96-98               |         |
| Time to repetition (ms)            | 11,930-15,000       |         |
| Flip angle (°)                     | 130-160             |         |
| Slice acquisition                  | 2-Dimensional       |         |
| Postprocessing                     | Homogenization      |         |
| Sequence type                      | Spin echo           |         |

Abbreviations: CT = computed tomography; FOV = field of view; kV = kilovoltage; MR = magnetic resonance; sCT = synthetic CT.

with a dose cutoff at 15% and within the planning target volume using global gamma criteria of 3%/3 mm, 2%/2 mm, and 1%/1 mm. The gamma calculations within

**Table 3** Summary of the treatment planning techniques used for all centers and patient-specific aspects for the 145 evaluated patients

| Parameter  | No. of patients |
|--|-----------------|
| Target   |                 |
| Prostate   | 76              |
| Prostate and vesicles  | 52              |
| Prostate, vesicles, and iliac lymph nodes                      | 17              |
| Prescribed dose (Gy) – fractionation (Gy/fraction × fractions) |                 |
| 78 – 2 × 39  | 78              |
| 77 – 2.2 × 35  | 3               |
| 74 – 2 × 25 + 3 × 8  | 2               |
| 72.5 – 2.5 × 29  | 3               |
| 66 – 3 × 22  | 18              |
| 63 – 3 × 21  | 3               |
| 50 – 2 × 25  | 25              |
| 45 – 3 × 15  | 5               |
| 28 – 2 × 14, boost plan  | 8               |
| Treatment technique  |                 |
| IMRT   | 20              |
| VMAT   | 107             |
| Conventional, 3-field  | 18              |
| Treatment planning system                                      |                 |
| Varian Eclipse   | 100             |
| Elekta Oncentra MasterPlan                                     | 45              |
| Calculation model  |                 |
| AAA  | 100             |
| PB   | 45              |

Abbreviations: AAA = anisotropic analytical algorithm; IMRT = intensity modulated radiation therapy; PB = pencil beam; VMAT = volumetric modulated arc therapy.

MICE are implemented according to the method described by Wendling et al (26).

Two 1-sided tests of equivalence for paired samples (TOST-P) (27) were performed with an equivalence interval of (−0.5%, 0.5%) for all evaluated DVH criteria at a 95% confidence level. Dose criteria were evaluated as percentage of the prescribed dose and the volume criteria as absolute volume difference in percentage units. Equivalence testing is used to prove equality.

Differences in the external contour can arise owing to repositioning between CT and MR, which affects the sCT dose calculation and comparison. To investigate how differences in the external contours between the CT and sCT affected the dose comparison, a subset of patients (n=28, prescribed 78 Gy to the prostate, included at center 1) were further evaluated using an sCT that was corrected to have the same external contour as the CT. After the rigid registration of the sCT and CT, the CT external contour was used to create a new sCT external contour. Air inside of the new external contour was replaced with water, and tissue outside the new external contour was removed and replaced with air.

## Results

All patients who were uploaded to MriPlanner had successfully generated sCTs, including patients who were subsequently excluded owing to deviations from the study protocol (see below). The exclusions were due to operator fault or incorrect inclusion of study participants. The software was integrated into the current clinical workflows without modifications or any additional procedures. The mean (range) body mass index of the study population was 26.9 (18.0-37.7) kg/m<sup>2</sup>, and median (range) age was 72 (56-87) years.

After inclusion a total of 25 patients had to be excluded owing to 3-dimensional distortion correction inadvertently being turned off (n=12), the entire body contour was not included inside the FOV (n=4), limited FOV in slice direction due to operator fault (n=2), inclusion despite hip implants noted after MR imaging (n=2), extreme difference in rectum filling between MR and CT (n=1), patient included having been injected with an anatomy-distorting gel between prostate and rectum (n=1), extremely poor image quality of MR image (n=1), and patients imaged without coil holder (n=2), leaving a total of 145 patients available for evaluation. Eight patients with nodal involvement had an insufficient FOV in the slice direction to cover the complete target. Their boost plans, covering the prostate, were calculated. Figure 1 displays the height and weight distribution of the study population.

The mean dose deviations between sCT and CT were found to be very small, below 0.3% for all evaluated organs and targets; for a complete DVH comparison, see Table 4. With an equivalence interval of (−0.5%, 0.5%), the evaluated dose and volume points were shown to be equivalent at a 95% confidence interval using the TOST-P procedure described in reference 27. All P values were below 5e-7.



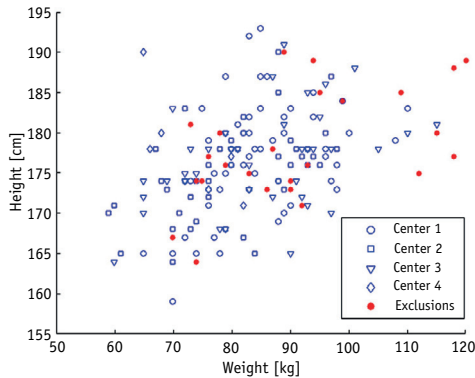


**Fig. 1.** Distribution of weight and height in the study population. Included patients, separated by included center, are presented in blue (circles, squares, triangles, and diamonds). Exclusions are presented in red (filled circles). (A color version of this figure is available at [www.redjournal.org](http://www.redjournal.org).)

The deviations between sCT and CT organ mean doses ranged between  $-1.15\%$  and  $1.42\%$  (Fig. 2a-d). The 4 centers showed similar results. Small differences were seen

between the prescriptions (ie, fractionation schemes found in Table 3), with an SD below 0.2% for the mean dose deviations.

The body-corrected sCTs showed smaller dose differences from the CT as compared with the original sCT for the 28 patients evaluated. The mean dose differences approached zero after correction. Standard deviations and maximum differences decreased (Figs. 3a and 3b). Gamma evaluation results are presented in Table 5 for the complete study population and the body-corrected subpopulation.

## Discussion

The present study investigated the accuracy and robustness of a commercial software that enables the transition from a multimodal CT-MR workflow to an MRI-only workflow for external radiation therapy of prostate cancer. The MRI-only treatment planning procedure described in this study requires only minor changes in clinical routine, adding a large FOV T2-weighted MRI sequence of approximately 5 minutes and discarding the CT examination altogether.

The study was performed at 4 different clinics, with different clinical workflows, hardware, and software. Treatment plans generated using sCT were dosimetrically

**Table 4** Mean dose deviation between sCT and CT

| Parameter                  | Mean deviation sCT vs CT (% of prescribed dose or volume percentage difference) (1 SD) | Mean deviation sCT vs CT (absolute dose [Gy] or volume percentage point difference) (1 SD) |
|----------------------------|--|--|
| Body                       |  |  |
| Maximum                    | 0.18 (0.79)  | 0.13 (0.50)  |
| PTV                        |  |  |
| Mean                       | 0.23 (0.42)  | 0.16 (0.28)  |
| D99%                       | 0.21 (0.50)  | 0.14 (0.35)  |
| V95%                       | 0.21 (0.65)  | 0.20 (0.62)  |
| CTV                        |  |  |
| Mean                       | 0.24 (0.44)  | 0.17 (0.29)  |
| Minimum                    | 0.21 (0.54)  | 0.14 (0.36)  |
| Bladder*                   |  |  |
| Mean                       | 0.04 (0.27)  | 0.03 (0.18)  |
| Rectum                     |  |  |
| Mean                       | 0.16 (0.42)  | 0.10 (0.28)  |
| V90%                       | 1.37 (3.56)  | 0.18 (0.42)  |
| V75%                       | 0.21 (2.74)  | 0.03 (0.59)  |
| V65%                       | 0.26 (1.99)  | 0.04 (0.59)  |
| Femoral heads <sup>†</sup> |  |  |
| Mean                       | 0.04 (0.18)  | 0.03 (0.11)  |
| Maximum                    | 0.05 (0.19)  | 0.03 (0.11)  |
|                            | 0.05 (0.38)  | 0.03 (0.26)  |
|                            | 0.07 (0.49)  | 0.06 (0.31)  |

*Abbreviations:* CT = computed tomography; CTV = clinical target volume; PTV = planning target volume; sCT = synthetic CT.

Total mean dose deviation between sCT and CT (145 patients). Deviations expressed in percentage of prescribed dose (mean, maximum, minimum, and D99%) or volume percentage difference (V95%, V90%, V75%, and V65%) (left column) and absolute change (in Gy) or volume percentage point difference (right column). Volume change evaluated for patients prescribed 78 Gy, according to the conventional arm of the HYPO-fractionated radiation therapy of intermediate-risk localized Prostate Cancer protocol.

\* One patient excluded owing to structure missing in the clinical plan.

<sup>†</sup> Results for 105 patients, exclusions due to structure not contoured in clinical routine.

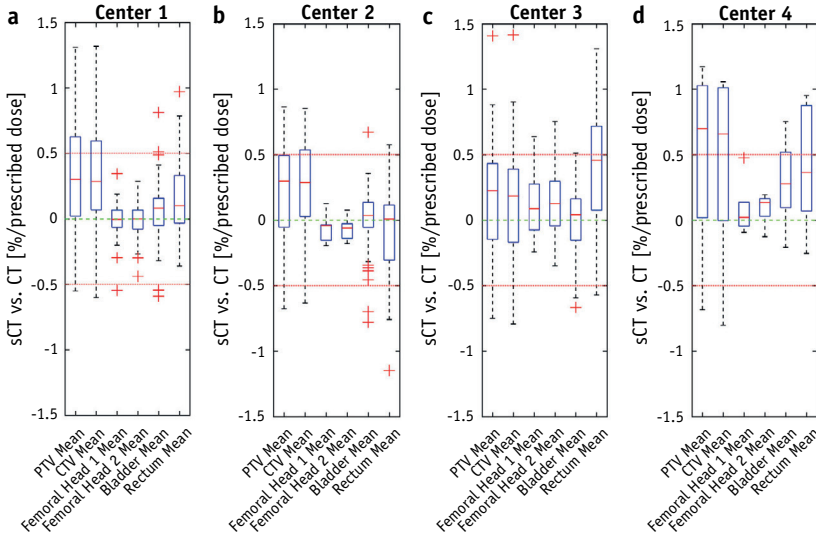


**Fig. 2.** (a-d) Individual center results. Deviations between synthetic computed tomography (sCT) and CT mean doses (sCT – CT, % of prescribed dose) at the 4 included centers for planning target volume (PTV), clinical target volume (CTV), femoral heads, bladder, and rectum.

accurate as compared with CT. In general, the dose differences observed between sCT- and CT-based plans were small and were shown to be statistically equivalent on

a 95% confidence level within  $\pm 0.5\%$ . The rectum volume criteria displays a higher mean deviation compared with the other OARs, which can be an influence of change in rectum filling or the replacement of gas with soft tissue in the sCT generation (21). A small systematic overshoot in Figure 2 is seen along with outliers near 1.5% dose deviation. The outliers were found to be patients with large outer body contour differences. The MR was frequently found systematically smaller in the anterior-posterior direction compared with the CT. This causes a higher sCT dose after recalculation. We hypothesize that this is an effect of the longer examination time of the MR compared with the CT. The study sequence was positioned at the end of the MR protocol for most patients, after an approximately 30- to 40-minute scan time. Patient relaxation could presumably cause the patients' anterior-posterior thickness to decrease and increase in the left-right direction, which was also seen in the data. In contrast to the MR examination, the CT examination is fast, and the patients are often more tense. The results indicate that the differences in patient external contour influence the dose comparison considerably, and after correcting for patient outline differences the differences are negligible. Hence, disparities in patient position are likely to be a major contributor in the small dose differences seen in our results. The differences in external patient contour also affected the gamma evaluation, but the results are still well within clinical acceptance criteria.

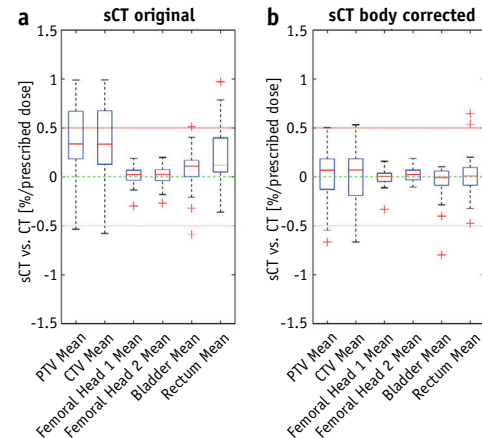


**Fig. 3.** (a, b) Body-corrected result. Results for 28 patients prescribed 78 Gy, evaluated with both an original synthetic computed tomography (sCT) and a body-corrected sCT compared with the CT. The original sCT/CT comparison (a) and the body-corrected sCT/CT comparison (b) for planning target volume (PTV), clinical target volume (CTV), femoral heads, bladder, and rectum mean doses (sCT – CT).

Previous studies on MRI-only prostate radiation therapy report results similar to ours. Commercially available MRCAT (MR for Calculating ATenuation, Phillips

**Table 5** Gamma evaluation

| Parameter   | 3%/3 mm <sub>g</sub>        | 2%/2 mm <sub>g</sub>       | 1%/1 mm <sub>g</sub>      |
|---|-----------------------------|----------------------------|---------------------------|
| Original sCT, complete study population (N = 145)     |                             |                            |                           |
| PTV   | 99.99 (0.06)                | 99.97 (0.13)               | 98.28 (4.58)              |
| Total   | 99.62 (0.36)                | 99.12 (0.63)               | 97.69 (1.26)              |
| >15%  | 99.66 (0.42)                | 99.30 (0.68)               | 97.94 (1.35)              |
| Subpopulation (n=28), body-corrected sCT/original sCT |                             |                            |                           |
| PTV   | 100.00 (0.00)/100.00 (0.00) | 99.98 (0.09)/100.00 (0.00) | 99.64 (1.70)/97.82 (3.96) |
| Total   | 100.00 (0.00)/99.72 (0.28)  | 100.00 (0.01)/99.38 (0.38) | 99.50 (0.45)/98.24 (0.79) |
| >15%  | 100.00 (0.00)/99.79 (0.29)  | 100.00 (0.01)/99.59 (0.42) | 99.96 (0.14)/98.43 (0.98) |

Abbreviations: PTV = planning target volume; sCT = synthetic computed tomography. Values in parentheses are 1 SD.

Healthcare, Vantaa, Finland) was reported to produce treatment plans with dose differences CT-sCT of 0.25% (0.17% SD) to the planning target volume and 0.42% (0.50% SD) for organs at risk (28). In that study the entire study population (n=13) was corrected for differences in patient external contour using an approach similar to the one presented in our study for the body-corrected subpopulation. A key difference between the method described in our study and MRCAT is that the latter is vendor specific. Other methods have been presented in the literature, also showing very high accuracy, but these are, to our knowledge, still in development or single-center use (12, 20, 29).

This study aimed at verifying the MRI-only method in a situation as close as possible to the clinical environment, without extensive corrections of the sCT data, to find the worst-case differences between the CT- and MR-based workflows. Because the MR and CT images were acquired at different occasions, ranging from 30 minutes to 1 day apart depending on the clinic, changes in internal anatomy were inevitable. The repositioning of the patient between modalities will also introduce differences in the external anatomy. Such differences could have been corrected for by using deformable registration, which is an approach that has been used previously (21). We opted to not employ such methods to preserve the integrity of the input data as much as possible. Therefore, the dose differences presented in our study are composed of actual errors in Hounsfield unit conversion as well as differences in patient anatomy and possible geometric distortions (remaining after correction) in the input MR data. Our study uses the conventional MR/CT workflow as a reference and recalculates the dose on the sCT for comparison. Another strategy would be to create a treatment plan optimized on the sCT for comparison against the CT, a method that has been shown to differ very little from our method (30, 31).

In this work the dosimetric accuracy in the MRI-only workflow is of primary interest. However, other important aspects of the treatment are also affected by removing the CT images, primarily patient positioning. Because many prostate cancer patients are positioned using implanted gold fiducials, configuration of suitable marker localization sequences that can be acquired in immediate succession to the sequence used for sCT generation is important. To

achieve a workflow with improved geometric accuracy compared with the CT/MR workflow, the uncertainty in the fiducial marker localization cannot exceed the MR-CT registration uncertainty. A future improvement would be to develop markers that are visible directly on the treatment planning sequence. Further, it would be of importance to the MRI-only workflow to integrate automatic fiducial detection (32). If markers are not used, the sCT should work well for matching against cone-beam CT scans and orthogonal X rays or megavoltage portal images, earlier demonstrated (33). The geometric fidelity of the sCT images will be investigated for such purpose in a future study.

In the implementation of MRI-only, it becomes crucial to ensure properly executed MRI procedures. Exclusions in this study were mainly due to improper inclusion or operator fault, which could be captured at an early stage with proper MR quality assurance (QA) procedures and staff training. Eight patients had insufficient target coverage in the slice direction. This was a consequence of the study design. The extra acquisition time allowed for adding on the sCT sequence to the protocol was restricted to approximately 5 minutes. In this time frame the necessary number of slices to cover the entire target volume for the 8 patients could not be acquired. This specific issue will not be the case in an actual MRI-only environment, with a dedicated MRI-only protocol. Education and training are important parts of the implementation process of MRI-only and are necessary to avoid operator fault at the MR scanner. Mistakes, such as an inadvertently turned-off 3-dimensional correction, could be prevented by staff training and working documents. Automatic control of the MR parameters at the MR scanner could be a possible method to detect erroneous parameter settings. This would not prevent operator faults, although it would be detected at an early stage of the process. Although no serious errors in sCT generation could be found in this study, a routine to detect potential errors is still needed. A simple sanity check of the Hounsfield unit distribution would probably be sufficient, or the use of patient-specific QA if a higher level of certainty is desirable. Methods for such QA procedures are an important part of MRI-only and should be developed and tested thoroughly before an implementation of the technique can be considered completed.

When the registration step between the treatment planning CT and MR images is eliminated, an important uncertainty is removed. The small differences found between CT- and sCT-based dose calculations in the present study must be set in contrast to the total uncertainty in radiation therapy. When considering the complete workflow, including uncertainties in beam calibration, relative dosimetry, dose calculations, and dose delivery, the International Commission on Radiation Protection states an estimated standard uncertainty of 5% in a clinical setup (34). The added uncertainty of a synthetically generated dose calculation image, shown in our study to differ only by fractions of a percent from CT-based dose calculations, is likely negligible in comparison to the total uncertainty. The dose differences presented in our study are well within previously published criterion of reliable MRI-only dose calculations (31). Furthermore, most of the dose difference is likely to stem from the difficulty in comparing images acquired at different occasions and not from the actual sCT conversion in itself, analogous to comparing fractional doses on cone-beam CTs in the traditional workflow.

## Conclusions

In conclusion, the MR-OPERA study shows that an MRI-only treatment planning workflow using MriPlanner software is dosimetrically accurate and robust for a variety of vendors, field strengths, and treatment techniques. The differences observed between CT and sCT dose distribution are small, and when compared with other uncertainties in radiation therapy they are negligible. The suggested method will allow implementation of an MRI-only workflow for external prostate radiation therapy in most clinics.

## References

- Karlsson M, Karlsson MG, Nyholm T, Amies C, Zackrisson B. Dedicated magnetic resonance imaging in the radiotherapy clinic. *Int J Radiat Oncol Biol Phys* 2009;74:644-651.
- Datta NR, David R, Gupta RK, et al. Implications of contrast-enhanced CT-based and MRI-based target volume delineations in radiotherapy treatment planning for brain tumors. *J Cancer Res Ther* 2008;4:9-13.
- Prabhakar R, Hareesh KP, Ganesh T, et al. Comparison of computed tomography and magnetic resonance based target volume in brain tumors. *J Cancer Res Ther* 2007;3:121-123.
- Rasch CR, Steenbakkers RJ, Fitton I, et al. Decreased 3D observer variation with matched CT-MRI, for target delineation in nasopharynx cancer. *Radiat Oncol* 2010;5:21.
- Khoos EL, Schick K, Plank AW, et al. Prostate contouring variation: Can it be fixed? *Int J Radiat Oncol Biol Phys* 2012;82:1923-1929.
- Roach M 3rd, Faillace-Akazawa P, Malfatti C, et al. Prostate volumes defined by magnetic resonance imaging and computerized tomographic scans for three-dimensional conformal radiotherapy. *Int J Radiat Oncol Biol Phys* 1996;35:1011-1018.
- Nyholm T, Nyberg M, Karlsson MG, Karlsson M. Systematisation of spatial uncertainties for comparison between a MR and a CT-based radiotherapy workflow for prostate treatments. *Radiation oncology* 2009;4:54.
- van Herk M, Remeijer P, Rasch C, et al. The probability of correct target dosage: Dose-population histograms for deriving treatment margins in radiotherapy. *Int J Radiat Oncol Biol Phys* 2000;47:1121-1135.
- Hsu SH, Cao Y, Huang K, et al. Investigation of a method for generating synthetic CT models from MRI scans of the head and neck for radiation therapy. *Phys Med Biol* 2013;58:8419-8435.
- Johansson A, Karlsson M, Nyholm T. CT substitute derived from MRI sequences with ultrashort echo time. *Medical physics* 2011;38:2708-2714.
- Paradis E, Cao Y, Lawrence TS, et al. Assessing the dosimetric accuracy of magnetic resonance-generated synthetic CT images for focal brain VMAT radiation therapy. *Int J Radiat Oncol Biol Phys* 2015;93:1154-1161.
- Dowling JA, Lambert J, Parker J, et al. An atlas-based electron density mapping method for magnetic resonance imaging (MRI)-alone treatment planning and adaptive MRI-based prostate radiation therapy. *Int J Radiat Oncol Biol Phys* 2012;83:e5-e11.
- Greer PB, Dowling JA, Lambert JA, et al. A magnetic resonance imaging-based workflow for planning radiation therapy for prostate cancer. *Med J Aust* 2011;194:S24-S27.
- Sjölund J, Forsberg D, Andersson M, et al. Generating patient specific pseudo-CT of the head from MR using atlas-based regression. *Phys Med Biol* 2015;60:825-839.
- Stanescu T, Jans HS, Pervez N, et al. A study on the magnetic resonance imaging (MRI)-based radiation treatment planning of intracranial lesions. *Phys Med Biol* 2008;53:3579-3593.
- Andreasen D, Van Leemput K, Edmund JM. A patch-based pseudo-CT approach for MRI-only radiotherapy in the pelvis. *Med Phys* 2016;43:4742.
- Jonsson JH, Karlsson MG, Karlsson M, Nyholm T. Treatment planning using MRI data: an analysis of the dose calculation accuracy for different treatment regions. *Radiation oncology* 2010;5:62.
- Korhonen J, Kapanen M, Keyriläinen J, et al. Absorbed doses behind bones with MR image-based dose calculations for radiotherapy treatment planning. *Med Phys* 2013;40:011701.
- Lambert J, Greer PB, Menk F, et al. MRI-guided prostate radiation therapy planning: Investigation of dosimetric accuracy of MRI-based dose planning. *Radiother Oncol* 2011;98:330-334.
- Kim J, Glide-Hurst C, Doerner A, et al. Implementation of a novel algorithm for generating synthetic CT images from magnetic resonance imaging data sets for prostate cancer radiation therapy. *Int J Radiat Oncol Biol Phys* 2015;91:39-47.
- Siversson C, Nordstrom F, Nilsson T, Nyholm T, Jonsson J, Gunnlaugsson A, et al. Technical Note: MRI only prostate radiotherapy planning using the statistical decomposition algorithm. *Medical physics* 2015;42:6090-6097.
- Deasy JO, Blanco AI, Clark VH. CERR: A computational environment for radiotherapy research. *Med Phys* 2003;30:979-985.
- Widmark A. Phase III study of HYPOfractionated RadioTherapy of intermediate risk localised Prostate Cancer. Available at: [www.isrctn.com/ISRCTN45905321](http://www.isrctn.com/ISRCTN45905321). Accessed May 1, 2017.
- Low DA, Harms WB, Mutic S, et al. A technique for the quantitative evaluation of dose distributions. *Med Phys* 1998;25:656-661.
- Nyholm T, Berglund M, Brynolfsson P, Jonsson J. EP-1533: ICE-Studio- An interactive visual reaserch tool for image analysis. *Radiotherapy and Oncology* 2015;115.
- Wendling M, Zijp LJ, McDermott LN, et al. A fast algorithm for gamma evaluation in 3D. *Med Phys* 2007;34:1647-1654.
- Mara CA, Cribbie RA. Paired-samples test of equivalence. *Commun Stat Simul Comput* 2012;41:15.
- Köhler M, Vaara T, Grootel MV, et al. MR-only simulation for radiotherapy planning. Amsterdam, The Netherlands: Philips white paper; 2015.
- Korhonen J, Kapanen M, Keyriläinen J, et al. A dual model HU conversion from MRI intensity values within and outside of bone segment for MRI-based radiotherapy treatment planning of prostate cancer. *Med Phys* 2014;41:011704.
- Jonsson JH, Akhtari MM, Karlsson MG, Johansson A, Asklund T, Nyholm T. Accuracy of inverse treatment planning on substitute CT

- images derived from MR data for brain lesions. *Radiat Oncol* 2015; 10:13.
31. Korsholm ME, Waring LW, Edmund JM. A criterion for the reliable use of MRI-only radiotherapy. *Radiat Oncol* 2014;9:16.
  32. Ghose S, Mitra J, Rivest-Henault D, et al. MRI-alone radiation therapy planning for prostate cancer: Automatic fiducial marker detection. *Med Phys* 2016;43:2218.
  33. Korhonen J, Kapanen M, Sonke JJ, et al. Feasibility of MRI-based reference images for image-guided radiotherapy of the pelvis with either cone-beam computed tomography or planar localization images. *Acta Oncol* 2015;54:889-895.
  34. International Commission on Radiation Protection. Prevention of accidents to patients undergoing radiation therapy. ICRP publication 86. *Ann ICRP* 2000;30.



Paper III







# Registration free automatic identification of gold fiducial markers in MRI target delineation images for prostate radiotherapy

Christian Gustafsson<sup>a)</sup>

Department of Hematology, Oncology and Radiation Physics, Skåne University Hospital, Lund 221 85, Sweden  
Department of Medical Radiation Physics, Lund University, Malmö 205 02, Sweden

Juha Korhonen

Department of Nuclear Medicine, Helsinki University Central Hospital, Helsinki 00290, Finland  
Department of Radiology, Helsinki University Central Hospital, Helsinki 00290, Finland  
Department of Radiation Therapy, Comprehensive Cancer Center, Helsinki University Central Hospital, Helsinki 00290, Finland

Emilia Persson

Department of Hematology, Oncology and Radiation Physics, Skåne University Hospital, Lund 221 85, Sweden  
Department of Medical Radiation Physics, Lund University, Malmö 205 02, Sweden

Adalsteinn Gunnlaugsson

Department of Hematology, Oncology and Radiation Physics, Skåne University Hospital, Lund 221 85, Sweden

Tufve Nyholm

Department of Radiation Sciences, Umeå University, Umeå 90187, Sweden  
Department of Immunology, Genetics and Pathology, Uppsala University, Uppsala 95105, Sweden

Lars E. Olsson

Department of Medical Radiation Physics, Lund University, Malmö 205 02, Sweden

(Received 26 May 2017; revised 14 July 2017; accepted for publication 6 August 2017;  
published 11 September 2017)

**Purpose:** The superior soft tissue contrast of magnetic resonance imaging (MRI) compared to computed tomography (CT) has urged the integration of MRI and elimination of CT in radiotherapy treatment (RT) for prostate. An intraprostatic gold fiducial marker (GFM) appears hyperintense on CT. On T2-weighted (T2w) MRI target delineation images, the GFM appear as a small signal void similar to calcifications and post biopsy fibrosis. It can therefore be difficult to identify the markers without CT. Detectability of GFMs can be improved using additional MR images, which are manually registered to target delineation images. This task requires manual labor, and is associated with interoperator differences and image registration errors. The aim of this work was to develop and evaluate an automatic method for identification of GFMs directly in the target delineation images without the need for image registration.

**Methods:** T2w images, intended for target delineation, and multiecho gradient echo (MEGRE) images intended for GFM identification, were acquired for prostate cancer patients. Signal voids in the target delineation images were identified as GFM candidates. The GFM appeared as round, symmetric, signal void with increasing area for increasing echo time in the MEGRE images. These image features were exploited for automatic identification of GFMs in a MATLAB model using a patient training dataset ( $n = 20$ ). The model was validated on an independent patient dataset ( $n = 40$ ). The distances between the identified GFM in the target delineation images and the GFM in CT images were measured. A human observatory study was conducted to validate the use of MEGRE images.

**Results:** The sensitivity, specificity, and accuracy of the automatic method and the observatory study was 84%, 74%, 81% and 98%, 94%, 97%, respectively. The mean absolute difference in the GFM distances for the automatic method and observatory study was  $1.28 \pm 1.25$  mm and  $1.14 \pm 1.06$  mm, respectively.

**Conclusions:** Multiecho gradient echo images were shown to be a feasible and reliable way to perform GFM identification. For clinical practice, visual inspection of the results from the automatic method is needed at the current stage. © 2017 The Authors. *Medical Physics* published by Wiley Periodicals, Inc. on behalf of American Association of Physicists in Medicine. [<https://doi.org/10.1002/mp.12516>]

Key words: fiducial marker, MRI only, prostate cancer, radiation therapy, synthetic CT

## 1. INTRODUCTION

Since the introduction of modern radiotherapy treatment planning (RTP), computed tomography (CT) has been the

primary imaging modality used for RTP and delineation of target and organs at risk (OAR). A major drawback using CT images for this purpose is the limited soft tissue contrast. Magnetic resonance imaging (MRI) has superior soft tissue

contrast compared to CT and a widespread introduction of MRI into the radiotherapy clinics have therefore been seen in recent years.<sup>1,2</sup> It has also been proved that MRI can add clinical value to the target delineation process in external beam radiation therapy (EBRT), in particular of prostate.<sup>3,4</sup>

Today MRI is mainly used for target delineation in combination with CT. This procedure requires image registration between CT and MRI. Despite the superior contrast of MRI, the CT is helpful to provide the Hounsfield unit (HU) map of the tissues as input for the treatment planning calculations.

In the image registration process, an additional spatial uncertainty can be introduced in the RTP.<sup>5</sup> To avoid this and still profit from the superior soft tissue contrast in MRI, a workflow solely based on MRI (where the CT is excluded) is desired. Such a workflow is referred to as an MRI only workflow. In this workflow, the Hounsfield units of the tissue are calculated from the MR images and the resulting images are referred to as a synthetic CT (sCT). Multiple methods for creating sCT for prostate RTP has been presented.<sup>6–10</sup>

The dosimetric accuracy in high-quality sCTs for prostate cancer RTP is sufficient.<sup>6,7,11–13</sup> The sCTs can also be used as reference images for image-guided RT.<sup>14</sup> Thus, the entire RTP workflow can be conducted with MRI only.<sup>15</sup> At certain clinics, the prostate MRI only workflow has been used for standard clinical practice since 2012.<sup>10,15</sup> The workflow, however, draws from lack of automatic gold fiducial marker detection.

For standard EBRT of prostate cancer, the ordained total radiation dose to the prostate is divided into a number of smaller treatment fractions (e.g., 39 fractions over 8 weeks, total dose 78 Gy). A reproducible patient setup for the delivery of each treatment fraction to the prostate is essential. A common method to facilitate such a patient setup is to, prior to the start of the EBRT, insert small cylinder-shaped gold fiducial markers (GFMs) into the prostate. After setup of the patient at the RT table, the GFMs can be visualized using on board image guidance techniques such as x-ray imaging or cone beam CT (CBCT), and the patient position can be adjusted in connection to each treatment fraction. The visualization of the GFMs is straightforward on x-ray, CT, and CBCT as they appear hyperintense. However, x-ray-based images suffer from beam hardening and streak artifacts around GFMs.

In MR images, the GFMs are hypointense as they do not produce any genuine nuclear magnetic resonance signal.<sup>16</sup> The GFMs and the surrounding tissue interact with, and distorts the external static magnetic field in different ways. This can be quantitatively measured and is referred to as magnetic susceptibility. Due to the difference in magnetic susceptibility between GFMs and tissue, the MR signal around the GFMs is degraded.<sup>17,18</sup> The GFMs are therefore visualized as signal voids with shape and size dependent on the nature of the MRI sequence, the acquisition parameters, and the shape and orientation of the GFMs.<sup>17,19</sup>

Previous studies have investigated different ways of detecting and visualizing a metallic structure within the patient. Both spin echo and gradient echo MRI sequences have been suggested to improve the signal void visibility.<sup>20–26</sup>

Combinations of different MRI sequences has also been suggested.<sup>27,28</sup> The use of more exotic sequences to even enable a positive contrast of the metal has been developed.<sup>29–32</sup>

The use of multiple dedicated MRI sequences for prostate RTP is common. The proposed MRI only workflows for EBRT of prostate present in the literature all depend on separate MRI sequences for GFM identification, target delineation, and sCT generation.<sup>12,25,33,34</sup>

The use of separate sequences is unfavorable due to several reasons. First, multiple sequences increase the examination time. Secondly, there is a risk of patient motion between the image acquisitions which often requires image registration. An MRI sequence that would identify the GFMs, enable sCT generation, and target delineation in one single sequence with reasonable scan time is therefore desirable. To the best of our knowledge, the use of such a sequence has not been presented in the literature. To address the issue above concerning image registration, it would be of benefit to identify the GFMs directly in the image of interest.

T2-weighted (T2w) MRI sequences based on fast spin echo (FSE) are recommended and generally used for visualizing the internal structure of the prostate as the image contrast is sensitive for pathology.<sup>35</sup> With clinically used T2w FSE-based sequences, it has been shown that the delineation of GFMs has a maintained clinical acceptable spatial accuracy and that they are only visualized as small signal voids.<sup>19</sup> This behavior is due to several factors. The transversal orientation of the T2w image and the inferior–superior orientation of the long axis of the cylinder-shaped GFMs expose a cross section of the GFM that is minimal in the transversal imaging plane. Furthermore, the effect of the difference in magnetic susceptibility between the GFMs and the surrounding tissue is mitigated due to the reduction of susceptibility-induced signal losses provided by the FSE technique.

Intraprostatic calcifications of > 2 mm in diameter are estimated to exist in one-third of the patients undergoing EBRT of prostate cancer.<sup>36</sup> The calcifications may have a similar signal behavior as GFMs in T2w sequences, i.e., a signal void.<sup>25,37,38</sup> The same signal behavior may also be found from vessels in the prostate or post biopsy fibrosis and hemorrhages.<sup>37,39</sup> It can therefore be challenging to differentiate GFMs in T2w FSE-based sequences (Fig. 1).

The elimination of the manual task of identifying the GFMs in an MRI only workflow would be cost-effective and also eliminate the interobservatory differences and repeatability issues among human operators.

The feasibility of automatic GFM identification without the need for a dedicated identification sequence was demonstrated in T1-weighted images using a template matching approach where 67% of the patients (n = 15) had all markers correctly identified. By manual detection, 73% of the same patients had all markers correctly identified. The authors also concluded the need for improved differentiation between GFMs and intraprostatic calcifications.<sup>37</sup>

Another method for automatic GFM identification were recently proposed utilizing a machine learning pattern recognition framework using image information from a

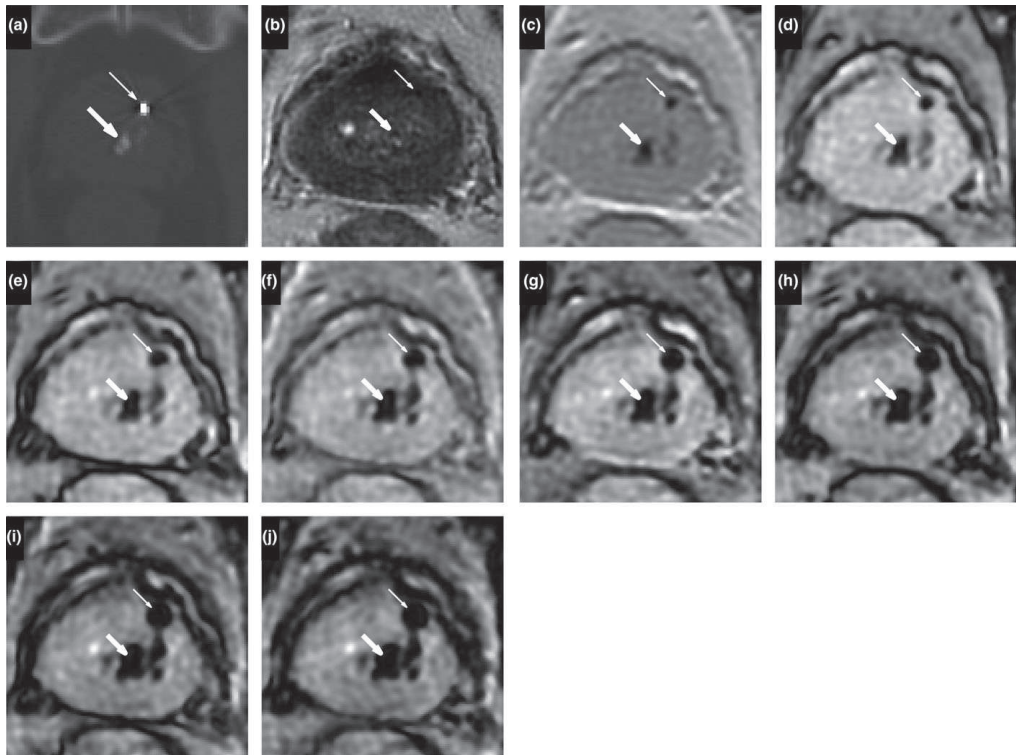


FIG. 1. An example of challenging differentiation between gold fiducial markers (GFMs) and intraprostatic calcifications. A GFM and an intraprostatic calcification are shown in the figures as thinner and bold arrows, respectively. The images depict the visualization of the objects using (a) CT, (b) MRI T2w PROPELLER, (c–j) MRI MEGRE for increasing echo times in the span 2.38–23.6 ms with an inter echo time of 3.03 ms. The GFM creates a round signal void with increasing area in the MEGRE images.

multiparametric acquisition protocol containing five different MRI series. About 81% of the patients ( $n = 32$ ) had all markers correctly identified.<sup>40</sup>

Neither of the methods aimed at identifying the GFMs in the target sequence and image registration is therefore inevitable. To remove the need for image registration or the need to account for possible within-session motion in MRI only workflows, we propose an alternative method.

The aim of this study was to: (a) develop a model for GFM identification and differentiation against intraprostatic calcifications, directly applied to the target delineation sequence without the need for image registration, (b) evaluate the developed model in an automated software for GFM identification, and (c) compare the performance of the automatic method against human observers.

## 2. MATERIALS AND METHODS

The proposed method relied on images from a clinical T2w target delineation FSE- and a clinical multiecho gradient

echo (MEGRE)-based sequence. These kinds of acquisition sequences are available on all MRI platforms. The methodology exploited the increased sensitivity to susceptibility effects resulting in increasing artifact size with increasing echo time (TE) in a MEGRE-based MRI sequence (Fig. 2). Gold fiducial marker candidates were automatically determined in the T2w MR images and mapped to an approximate position in the MEGRE images. All further analyses were performed in the MEGRE images (Fig. 3). The final GFM candidates were determined in the T2w image geometry.

### 2.A. GFM identification

A model for automatic identification and differentiation of GFM candidates in transversal T2w MR images intended for prostate target delineation was developed in MATLAB (version R2016a; Mathworks Inc., Sherborn, MA, USA). The model used a training dataset to identify GFM candidates by cross-correlating image data from multiple MRI sequences. The values of the model parameters was, unless stated

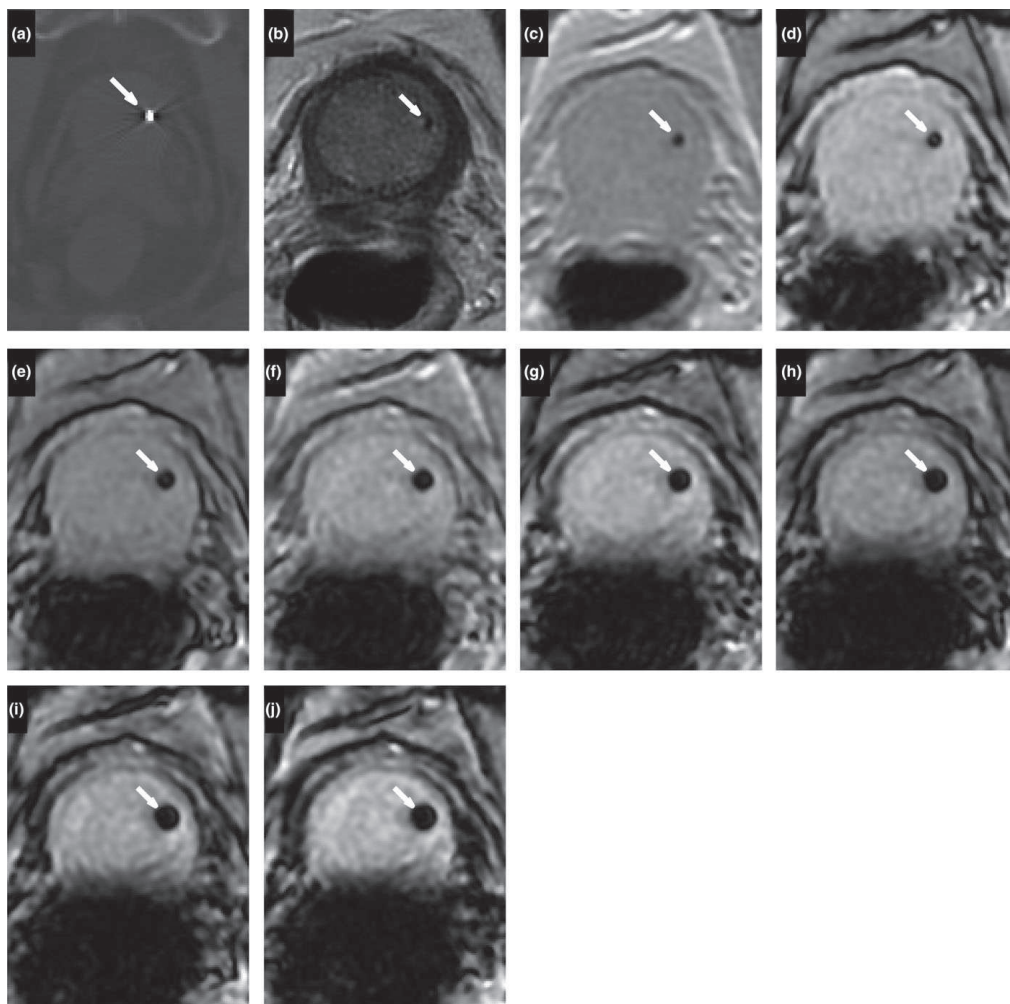


FIG. 2. Visualization of a gold fiducial marker (GFM) with different TEs. Figure shows GFM (bold arrow) in (a) CT, (b) MRI T2w PROPELLER, (c–j) MRI MEGRE for increasing TE in the span 2.38–23.6 ms with an inter echo time of 3.03 ms. The shape of the signal void from the GFM is round and the area is increasing with increasing TE. The images (c–j) visualize also the dependence of increasing echo time to the artifact below the prostate, originating from rectal gas.

otherwise, optimized in an iterative way using the training data. For an overview of the model workflow, see Fig. 3. To evaluate the performance, the model was applied to a second dataset, referred to as validation data. A human observatory study was also conducted on the second dataset to investigate the performance of manual GFM identification.

### 2.A.1. Patient preparation and data acquisition

The study was approved by the regional ethics board “Regionala Etikprövningsnämnden in Lund” with diary

number 2013/742 and 2016/801. For the training dataset, 20 consecutive prostate cancer patients without hip prosthesis undergoing primary EBRT were included in the study. Mean weight for the training dataset ( $n = 20$ ) was  $82.2 \pm 12.0$  kg [64–108 kg], mean age was  $72.1 \pm 5.5$  yr [60–81 yr].

In the validation dataset, 44 consecutive prostate cancer patients without hip prosthesis undergoing primary EBRT were included. Mean weight for the validation dataset ( $n = 44$ ) was  $86.6 \pm 13.3$  kg [62–128 kg], mean age was  $71.2 \pm 5.3$  yr [57–81 yr].

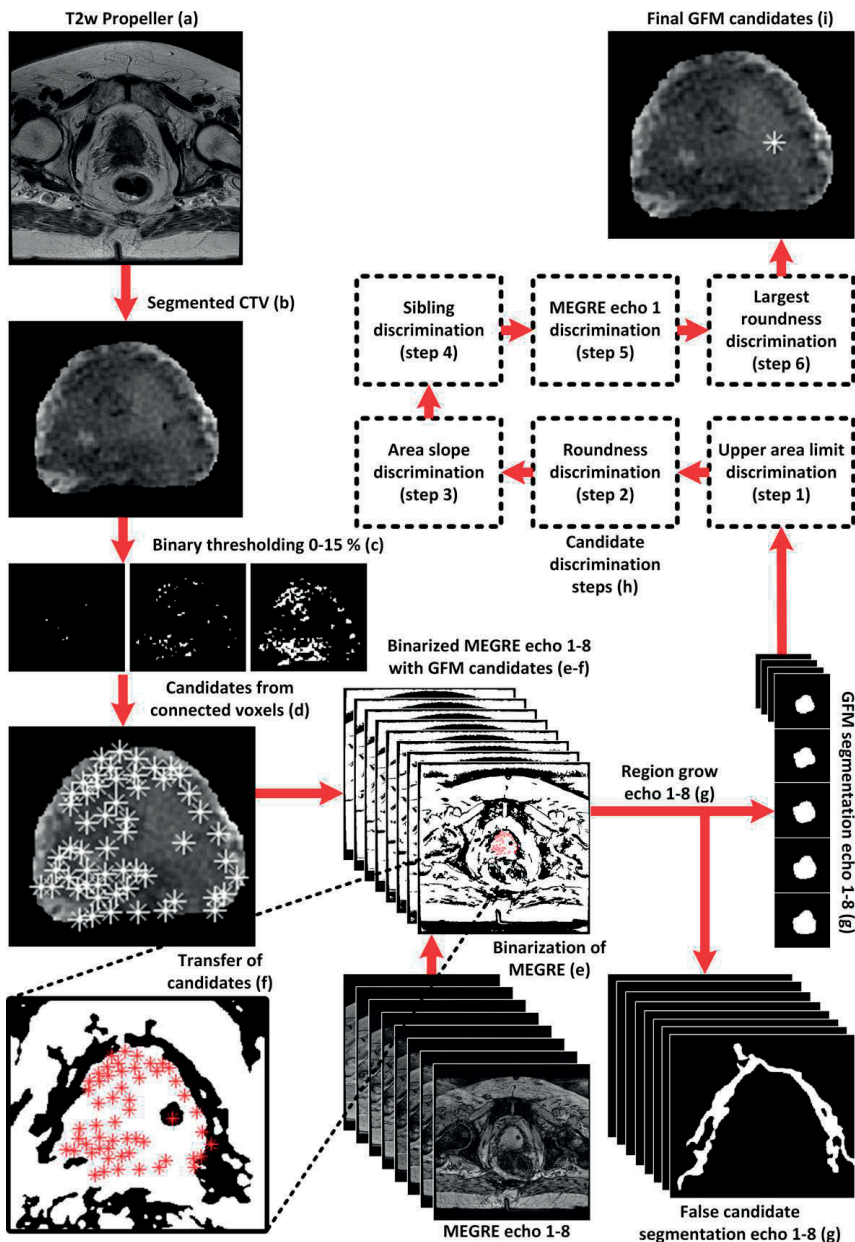


FIG. 3. An overview of the model workflow. The T2w propeller data (a) were segmented using the clinical target volume (CTV) (b) and were binarized for multiple thresholds (c). Gold fiducial marker (GFM) candidates were determined from the connected binary voxels (d). The multiecho gradient echo (MEGRE) data were binarized (e) and the GFM markers were transferred (f). The positions of the GFM candidates in the binarized MEGRE images individually defined starting points for a region grow segmentation, performed for all TEs (g). Candidate discrimination criteria were applied in a given order (h, step 1–6) to determine the final GFM candidates (i). [Color figure can be viewed at [wileyonlinelibrary.com](http://wileyonlinelibrary.com)]

Each patient in the training and validation data was subject to the insertion of three inferior–superior long axis-oriented cylinder-shaped intraprostatic GFMs (length 5.0 mm and diameter 1.0 mm). The GFMs were inserted transrectally or perineally using a clinical routine by an oncologist 2 weeks prior to image acquisition. Vi-siblin<sup>®</sup> was administered once daily during 14 days prior to CT. Microlax<sup>®</sup> was administered 1 hour prior to CT. The CT and MRI examinations were performed by a predefined acquisition protocol and in direct connection to each other.

Three patients in the validation dataset had, due to GFM migration, only two GFMs remaining in the prostate at the time of image acquisition. Four patients were excluded from the validation data set due to major imaging artifacts stemming from large amount of rectum gas (Fig. 2).

All MRI examinations were performed using a 3T wide bore 70 cm MRI system (Discovery 750W, Software DV25.0R02-1549b, General Electric Healthcare, Milwaukee, WI, USA) equipped with a flat table top. The MRI system was continuously being subject to monthly quality control using vendor-specific coil tests and a third party commercial phantom for assessing geometric accuracy for large field of views (Spectronic Medical AB, Helsingborg, Sweden). A GE GEM Anterior Array 16 channel receiver array coil was placed over the pelvic area of the patients using stiff coil bridges.

The clinical MRI sequence used for target delineation was a FSE-based T2w transversal MRI sequence, referred to as the target delineation sequence. The MRI sequence used for GFM identification was referred to as the MEGRE sequence. This multiecho sequence acquired gradient echo images for multiple slices for multiple TEs simultaneously. In this sequence, the shape from the signal void from the GFM was round, and the area increased with increasing TE. The artifact size was usually larger than the physical dimensions of the GFM and spanned through multiple slices. The image dataset was referred to as MEGRE data. To minimize motion between the sequences, the MEGRE sequence was executed either immediately before or after the target delineation sequence. All image data had automatic vendor-based image homogenization applied to it. Parameters for MRI sequences are displayed in Table I.

All CT examinations were acquired with a Siemens Somatom Definition AS+ (Siemens Healthcare, Forchheim, Germany, slice thickness 3 mm, reconstructed diameter 500 mm and reconstructed in-plane resolution 0.98 mm × 0.98 mm).

### 2.A.2. GFM candidate detection in the T2w image

Using the automated software for GFM identification, a set of potential GFMs, referred to as GFM candidates, were detected in the T2w target delineation sequence. The GFMs did not generate any MR signal and was visualized as signal void voxels. Other objects in the prostate, such as intraprostatic calcifications or post biopsy hemorrhage had similar signal behavior and could not be differentiated from each other. All of these objects were therefore identified as GFM candidates.

TABLE I. MRI acquisition parameters for the target delineation and the MEGRE sequences referred to in this study.

| Parameter                                     | Target delineation sequence | MEGRE sequence      |
|---|-----------------------------|---------------------|
| Sequence type                                 | FSE <sup>a</sup>            | GRE <sup>b</sup>    |
| 2D/3D   | 2D                          | 2D                  |
| Scan plane                                    | Axial                       | Axial               |
| Frequency field of view                       | 220 mm <sup>c</sup>         | 240 mm <sup>d</sup> |
| Phase field of view                           | 220 mm                      | 240 mm <sup>c</sup> |
| Scan matrix size (frequency × phase)          | 352 × 352                   | 164 × 164           |
| Reconstructed matrix size (frequency × phase) | 512 × 512                   | 512 × 512           |
| Repetition time                               | 9151 ms                     | 1000 ms             |
| Echo time                                     | 96 ms                       | 2.38–23.6 ms        |
| Inter echo time                               | -                           | 3.03 ms             |
| Slice thickness                               | 2.8 mm                      | 2.8 mm              |
| Slice spacing                                 | 0.0 mm                      | 0.0 mm              |
| Number of slices                              | 32                          | 34                  |
| Number of echoes                              | 1                           | 8                   |
| Number of averages                            | 2.1                         | 2                   |
| 3D geometry correction                        | Off (not available)         | On                  |
| Bandwidth/pixel                               | 473 Hz                      | 508 Hz              |
| Image homogenization                          | Yes (SCIC)                  | Yes (SCIC)          |
| Shimming method                               | Auto (first order)          | Auto (first order)  |
| RF transmit mode                              | Multitransmit               | Multitransmit       |
| Acquisition time                              | 5 min                       | 5 min               |

<sup>a</sup>Vendor-specific name of the sequence used was PROPELLER (periodically rotated overlapping parallel lines with enhanced reconstruction).

<sup>b</sup>Vendor-specific name of the sequence used was a multiecho FGRE.

<sup>c</sup>Right–left direction.

<sup>d</sup>Anterior–posterior direction.

The clinical target volume (CTV) from the treatment plan of the patient was used as a rough mask to limit the number of candidates detected in the automated software. The segmented T2w image was normalized to the maximum signal value and in a loop binarized using threshold values of 0% to 15% (step size of 1%) of the maximum signal value. In each step, the 3D connected components with a value of 1 and a connectivity of at least 6 voxels were identified and the coordinates for the center of mass (COM) of the 3D connected components were determined. If the coordinates for COM of a current candidate were within a radius of 2 mm of a previous detected candidate, the current candidate was discarded. This implicated that candidates detected for lower threshold values (therefore lower signal) were prioritized over candidates detected for higher threshold values.

A set of reference GFMs coordinates were defined manually as a data preparation step by an experienced physicist using all the available image information from MRI and CT. One fake GFM candidate in each patient was automatically inserted in the software to assess the performance of discriminating true negative candidates. The fake GFM candidate was assigned coordinates that equaled the average position of the specific patient reference GFMs coordinates.

### 2.A.3. GFM identification and image processing in the MEGRE images

Image information from the MEGRE sequence was used to determine which of the GFM candidates corresponded to the true GFMs. The MEGRE data volume was interpolated in all spatial directions with a factor of 2 (to  $1024 \times 1024 \times 64$ ) and every slice for each echo was binarized using a locally 2D adaptive threshold method.<sup>41</sup> Zero-valued pixel clusters of  $< 150$  pixels in the binarized MEGRE slices were replaced with the value 1. The coordinates for the COM of the GFM candidates in the T2w images were converted to the corresponding coordinates in the binarized MEGRE data, using the DICOM MRI coordinate system. A GFM candidate was classified as potentially true if its position in the binarized MEGRE data correlated to a round area of zero-valued pixels and the round area was increasing with increasing TE.

### 2.A.4. GFM candidate discrimination

The GFM candidates in the binarized MEGRE data were defined as the starting points for separate region grow segmentations. The region grow segmentation was done independently for each echo in the binarized MEGRE data. A collection of discrimination criteria were applied in a given order to determine which GFM candidates corresponded to the true GFMs (Fig. 3).

Region grow segmentations which produced an area larger than 1/30 of the largest prostate slice CTV segmentation was discarded to avoid over segmentations. This was referred to as step 1 discrimination. The area and roundness for each region grow segmentation for each TE after segmentation area discrimination were calculated. The roundness was defined as

$$R = 4\pi S_A / S_P^2 \quad (1)$$

where  $R$  was a measure for roundness ranging from 0 to 1 where 1 equaled a perfect circle,  $S_A$  being the area of the region grow segmentation and  $S_P$  being the perimeter of the region grow segmentation. The mean value for the roundness, calculated using all echoes, was used in the automated software as the measure for roundness.

The magnetic susceptibility difference between the GFM and the surrounding tissues created inhomogeneities and micro-gradients in the static magnetic field. Due to the absence of a spin refocusing pulse in the MEGRE sequence, the origin of the artifact was dominated by the effect of intravoxel spin dephasing. The phase change within a voxel can be described as

$$\Delta\phi = \gamma G_i \Delta r TE \quad (2)$$

where  $\gamma$  is the gyromagnetic ratio,  $G_i$  is the internal magnetic field micro-gradient,  $\Delta r$  is the voxel size and  $TE$  is the echo time.<sup>42</sup> The intravoxel phase change increases with increasing echo time, resulting in an echo time-dependent decreasing MRI signal which created the signal voids.

The GFM was assumed to have the largest magnitude of susceptibility for all available tissues in the prostate.<sup>17</sup> The change in the region grow segmentation area with respect to the TE was assumed to be linear and dependent on the susceptibility.<sup>18,43</sup> The linear change was referred to as the area slope and was calculated in the automated software by fitting a first-degree polynomial to the area and TE data.

The lower limits of roundness and area slope were applied in the respective order to the GFM candidates with a value of 0.67 and 10 pixels/ms (in interpolated binarized MEGRE data). This was respectively referred to as step 2 and step 3 discrimination. The lower limit of roundness was chosen to allow for a nonperfect round shape, allowing inclusion of tilted GFMs. The lower limit of area slope was chosen to allow for nonperfect segmentation of each individual TE.

Multiple GFM candidates corresponding to the same signal void and within a radius of 6 mm in the binarized MEGRE echo 6 data were referred to as sibling candidates. All GFM sibling candidates except the sibling candidate closest to the COM of the signal void was discriminated. This was referred to as step 4 discrimination. Further discrimination was performed by excluding the candidates that did not have a signal void for the lowest TE in the MEGRE images, referred to as step 5 discrimination.

If more than three candidates remained, the three GFM candidates with the largest roundness were considered to be the final GFM candidates, referred to as step 6 discrimination. The final GFM candidates that were within a radius of 7.5 mm to the reference GFMs coordinates in the T2w image were considered the true GFMs. The value of 7.5 mm was selected to encompass the length of the cylinder-shaped GFM (5.0 mm), taking into account the potential partial volume artifact in slice direction and to allow for a minor positioning error when defining the reference GFMs coordinates.

## 2.B. Analysis of the detection performance of the model

The detection performance of the developed model was assessed using the common detection performance metrics sensitivity =  $TP/(TP + FN)$ , specificity =  $TN/(TN + FP)$ , accuracy =  $(TN + TP)/(TN + TP + FN + FP)$  where TP, true-positive GFM candidate; TN, true-negative GFM candidate; FP, false-positive GFM candidate; FN, false-negative GFM candidate. For comparison with previous studies, the true-positive rate (TPR) was defined as  $TP/(\text{total of all GFM in the study})$  which is equal to the sensitivity metric.

## 2.C. Analysis of the GFM spatial position

The true gold maker fiducial positions were determined in the CT using an automatic method. The CT volume was segmented using the CTV as a segmentation mask, normalized and then binarized using Otsu's segmentation method.<sup>44</sup> The 3D connected components with a value of 1 and a connectivity of 26 voxels were identified and the coordinates for the

COM of these 3D connected components were determined. The COM of the 3D connected components was checked for validity and considered to be the true GFM positions. The spatial position of the final GFM candidates in the MR images of the target delineation sequence remaining after the discrimination steps were compared with the true GFM positions defined in the CT images. The most caudal true GFM and final GFM candidate was defined as  $M_1$ . The most cranial one was defined  $M_3$  and the intermediate was defined  $M_2$ . The internal distances between all the true-positive GFM candidates detected in the MRI and true GFMs in the CT was calculated using the respective distances  $M_2 - M_1$ ,  $M_3 - M_1$ , and  $M_3 - M_2$ . The difference in the GFM internal distances between CT and MRI were calculated by

$$|(M_2 - M_1)_{MR}| - |(M_2 - M_1)_{CT}| \quad (3)$$

$$|(M_3 - M_1)_{MR}| - |(M_3 - M_1)_{CT}| \quad (4)$$

$$|(M_3 - M_2)_{MR}| - |(M_3 - M_2)_{CT}| \quad (5)$$

## 2.D. Human observatory study of GFM detectability

A manual human observatory study was conducted to compare the performance of the automatic method against the performance of five human observers. Three medical physicists and two MRI technologists were asked to delineate the GFMs in the T2w images. One of the medical physicists had seen the patient material 6 months prior to the observatory study. One of the MRI technologists did not comply with given instructions and was excluded. The observers were presented with the T2w and the MEGRE images simultaneously in an in-house developed MATLAB graphical user interface. The detection performance and analysis of the GFM spatial position was assessed using the same criterions as in the automatic method. To enable the comparison, a value for true-negative GFM was set to 1 for each patient.

## 3. RESULTS

The number of true GFMs, detection of calcification, and number of GFM candidates remaining after each discrimination step together with the detection performance of the model for each patient in the validation data are displayed in Table II. Ten out of the 20, and 29 out of the 40 patients had intraprostatic calcifications  $\geq 2$  mm (FWHM) visible in the CT images for the training- and validation data, respectively.

Ninety eight GFMs out of 117 true GFMs were correctly identified and considered true positive. This corresponded to a TPR of 84%. The missing 19 GFMs were considered false negative. Fourteen GFMs were falsely identified as true GFMs and considered false positive. The fake candidate inserted for each patient were successfully discriminated yielding a total true negative of 40 GFMs. Using TP = 98, FN = 19, FP = 14, and TN = 40 yielded sensitivity = 84%, specificity = 74%, and accuracy = 81%.

All true GFMs were correctly identified in 24/40 patients (=60%). Out of those 24 patients, two patients had only two

GFMs left in the prostate due to GFM migration and 15 patients had detected calcifications  $\geq 2$  mm (FWHM).

Thirteen out of the 14 false-positive GFMs candidates were due to calcifications mistaken for GFMs. One out of 14 false-positive was due to a signal void in the MEGRE of unknown origin. Two out of the 19 false-negative GFMs candidates were due to the absence of a GFM candidate, 3 out of the 19 did not have a roundness above the lower limit, and 6 out of the 19 did not have an area slope above the lower limit or had an incorrectly calculated area slope due to a failed segmentations. Eight out of 19 was excluded in discrimination step 6.

The mean, standard deviation, minimum and maximum absolute difference in the internal distances of the true-positive GFM candidates between CT and MRI for the 40 included patients is displayed in Table III.

The mean detection performance for the manual observatory study was  $98 \pm 1$  [97 100]%,  $94 \pm 4$  [92 100]%,  $97 \pm 2$  [96 100]% for sensitivity, specificity, and accuracy, respectively. The mean TPR was determined to be  $98 \pm 1$  [97 100]%. The mean number of patients with all GFMs correctly identified was 41.5 out of 44. The mean absolute difference in the internal distances between the true-positive GFM candidates and true GFMs in the CT, measured for all true-positive candidates in all patients and all observers, was  $1.14 \pm 1.06$  [0.01 6.26 mm].

## 4. DISCUSSION

This study developed a method for automatic detection of intraprostate GFMs in T2w target delineation MR images. The method relied on transformation of image information from MEGRE images acquired at multiple TEs to the T2w images without any need for image registration. The T2w images presented the GFMs as small signal voids. The proposed method increased the signal void volume of the GFMs with respect to TE to separate the GFMs from other potential signal voids in prostate.

The method was validated for 40 prostate cancer patients. The sensitivity, specificity, and accuracy of the automatic GFM detection were 84%, 74%, and 81%, respectively. The mean absolute difference in the GFM internal distances between CT and MRI was shown to be  $1.28 \pm 1.25$  mm. The same patient image material was used for the manual human observatory study with four observers where the sensitivity, specificity, and accuracy was determined to be 98%, 94%, and 97%, respectively. The mean absolute difference in the GFM internal distances between CT and MRI was shown to be  $1.14 \pm 1.06$  mm.

The experiments suggest that acquiring MEGRE images could be a valid approach in identifying GFMs, both for automatic and manual detection methods. In analogy to the calculated area slope and roundness in the automatic method, these image features can easily be recognized by a human eye and thereby enable identification and discrimination of GFMs.

Previous studies regarding automatic identification of GFMs have used image registration for GFM detection and calculation of model accuracy.<sup>37,40</sup> One of these studies used



TABLE II. Number of GFM candidates left after each discrimination step and the detection performance of the model for all patients in the study. Detected calcifications  $\geq 2$  mm (FWHM) and number of true GFMs in the CT for each patient in the study are shown. Patient 6, 20, 22, and 30 were excluded from the study due to major imaging artifacts stemming from large amount of rectum gas.

| Patient | # of true GFMs | Calcifications detected in CT | Detected candidates | Step 1 | Step 2 | Step 3 | Step 4 | Step 5 | Step 6 | TP | TN | FP | FN |
|---------|----------------|-------------------------------|---------------------|--------|--------|--------|--------|--------|--------|----|----|----|----|
| 1       | 3              | No                            | 726                 | 67     | 16     | 10     | 5      | 3      | 3      | 3  | 1  | 0  | 0  |
| 2       | 3              | Yes                           | 608                 | 74     | 6      | 5      | 3      | 3      | 3      | 3  | 1  | 0  | 0  |
| 3       | 3              | Yes                           | 346                 | 21     | 7      | 6      | 3      | 3      | 3      | 3  | 1  | 0  | 0  |
| 4       | 2              | Yes                           | 842                 | 80     | 17     | 10     | 2      | 2      | 2      | 2  | 1  | 0  | 0  |
| 5       | 3              | Yes                           | 1193                | 78     | 14     | 12     | 3      | 2      | 2      | 2  | 1  | 0  | 1  |
| 6       | 3              | No                            | 802                 | 59     | 8      | 2      | 1      | 1      | 1      | 1  | 1  | 0  | 2  |
| 7       | 3              | Yes                           | 939                 | 76     | 14     | 6      | 2      | 2      | 2      | 2  | 1  | 0  | 1  |
| 8       | 3              | Yes                           | 423                 | 28     | 12     | 6      | 3      | 3      | 3      | 1  | 1  | 2  | 2  |
| 9       | 3              | No                            | 552                 | 58     | 10     | 7      | 4      | 2      | 2      | 2  | 1  | 0  | 1  |
| 10      | 2              | Yes                           | 533                 | 36     | 11     | 7      | 3      | 3      | 3      | 2  | 1  | 1  | 0  |
| 11      | 3              | No                            | 305                 | 40     | 9      | 8      | 4      | 4      | 3      | 3  | 1  | 0  | 0  |
| 12      | 3              | Yes                           | 806                 | 133    | 13     | 8      | 3      | 3      | 3      | 3  | 1  | 0  | 0  |
| 13      | 3              | Yes                           | 695                 | 84     | 10     | 6      | 3      | 3      | 3      | 3  | 1  | 0  | 0  |
| 14      | 3              | Yes                           | 370                 | 47     | 13     | 7      | 3      | 3      | 3      | 2  | 1  | 1  | 1  |
| 15      | 3              | Yes                           | 345                 | 40     | 10     | 9      | 7      | 7      | 3      | 2  | 1  | 1  | 1  |
| 16      | 3              | No                            | 508                 | 36     | 11     | 6      | 3      | 3      | 3      | 3  | 1  | 0  | 0  |
| 17      | 3              | Yes                           | 869                 | 67     | 16     | 12     | 3      | 3      | 3      | 2  | 1  | 1  | 1  |
| 18      | 3              | Yes                           | 742                 | 72     | 14     | 9      | 3      | 3      | 3      | 3  | 1  | 0  | 0  |
| 19      | 3              | No                            | 555                 | 39     | 8      | 5      | 2      | 2      | 2      | 2  | 1  | 0  | 1  |
| 20      | 3              | Yes                           | 1168                | 99     | 15     | 4      | 3      | 1      | 1      | 1  | 1  | 0  | 2  |
| 21      | 3              | Yes                           | 690                 | 114    | 18     | 11     | 6      | 5      | 3      | 2  | 1  | 1  | 1  |
| 22      | 3              | No                            | 502                 | 25     | 5      | 0      | 0      | 0      | 0      | 0  | 1  | 0  | 3  |
| 23      | 3              | Yes                           | 267                 | 30     | 7      | 4      | 3      | 2      | 2      | 2  | 1  | 0  | 1  |
| 24      | 3              | Yes                           | 558                 | 67     | 28     | 19     | 7      | 4      | 3      | 3  | 1  | 0  | 0  |
| 25      | 3              | No                            | 184                 | 13     | 7      | 5      | 3      | 3      | 3      | 3  | 1  | 0  | 0  |
| 26      | 3              | Yes                           | 729                 | 62     | 12     | 11     | 5      | 4      | 3      | 3  | 1  | 0  | 0  |
| 27      | 3              | Yes                           | 649                 | 73     | 10     | 5      | 3      | 3      | 3      | 3  | 1  | 0  | 0  |
| 28      | 3              | Yes                           | 721                 | 51     | 5      | 4      | 3      | 3      | 3      | 3  | 1  | 0  | 0  |
| 29      | 3              | Yes                           | 441                 | 50     | 12     | 9      | 3      | 3      | 3      | 3  | 1  | 0  | 0  |
| 30      | 3              | Yes                           | 683                 | 49     | 10     | 6      | 3      | 2      | 2      | 2  | 1  | 0  | 1  |
| 31      | 3              | Yes                           | 522                 | 24     | 4      | 3      | 2      | 2      | 2      | 2  | 1  | 0  | 1  |
| 32      | 3              | Yes                           | 1125                | 142    | 16     | 10     | 3      | 3      | 3      | 3  | 1  | 0  | 0  |
| 33      | 3              | No                            | 407                 | 33     | 12     | 11     | 3      | 3      | 3      | 3  | 1  | 0  | 0  |
| 34      | 3              | Yes                           | 812                 | 93     | 30     | 20     | 5      | 5      | 3      | 0  | 1  | 3  | 3  |
| 35      | 3              | Yes                           | 1082                | 100    | 27     | 18     | 6      | 4      | 3      | 2  | 1  | 1  | 1  |
| 36      | 3              | No                            | 773                 | 42     | 17     | 11     | 5      | 3      | 3      | 3  | 1  | 0  | 0  |
| 37      | 3              | Yes                           | 958                 | 169    | 31     | 22     | 8      | 7      | 3      | 1  | 1  | 2  | 2  |
| 38      | 3              | Yes                           | 468                 | 56     | 20     | 15     | 5      | 4      | 3      | 2  | 1  | 1  | 1  |
| 39      | 3              | No                            | 394                 | 29     | 8      | 8      | 3      | 3      | 3      | 3  | 1  | 0  | 0  |
| 40      | 3              | Yes                           | 605                 | 47     | 16     | 11     | 4      | 4      | 3      | 3  | 1  | 0  | 0  |
| 41      | 3              | No                            | 317                 | 38     | 9      | 6      | 4      | 3      | 3      | 3  | 1  | 0  | 0  |
| 42      | 3              | Yes                           | 1073                | 148    | 15     | 9      | 4      | 3      | 3      | 3  | 1  | 0  | 0  |
| 43      | 2              | No                            | 768                 | 50     | 14     | 6      | 2      | 2      | 2      | 2  | 1  | 0  | 0  |
| 44      | 3              | Yes                           | 442                 | 45     | 5      | 5      | 4      | 4      | 3      | 3  | 1  | 0  | 0  |

GRE-based MRI sequences to produce T1- and T2\*-weighted images. The sensitivity, specificity, and accuracy for the T1-weighted images were 0.84, 1, and 0.88 and for the T2\*-weighted images, it were 0.55, 0.86, and 0.63. The model accuracy was determined to be  $0.5 \pm 0.5$  mm for both image types.<sup>37</sup>

Another study using multiparametric MRI information yielded a TPR of 0.95. The balanced steady-state free precession sequence (bTFE) was recommended to improve the GFM detection and performed alone a TPR of 0.77. The model accuracy was respectively determined to be 1.6 mm and 1.7 mm for multiparametric and bTFE MRI information.<sup>40</sup>

TABLE III. The mean, standard deviation (SD), minimum (Min), and maximum (Max) absolute difference in the internal distances of the true-positive GFM candidates between CT and MRI. Number of measured distances (n) was dependent on the total amount of true-positive GFM candidates determined in total.

| Distance                                  | Mean (mm) | SD (mm) | Min (mm) | Max (mm) | n  |
|---|-----------|---------|----------|----------|----|
| $ (M_2 - M_1)_{MR}  -  (M_2 - M_1)_{CT} $ | 1.27      | 1.25    | 0.10     | 5.91     | 29 |
| $ (M_3 - M_1)_{MR}  -  (M_3 - M_1)_{CT} $ | 1.74      | 1.53    | 0.04     | 5.99     | 26 |
| $ (M_3 - M_2)_{MR}  -  (M_3 - M_2)_{CT} $ | 0.83      | 0.68    | 0.12     | 2.68     | 26 |
| All of the above distances                | 1.28      | 1.25    | 0.04     | 5.99     | 81 |

However, due to the possibility of prostate motion between MRI and CT, image registration was avoided in our study. To assess the model accuracy, the mean absolute difference in the internal distances of the true-positive GFMs between CT and MRI was calculated. With respect to the difference in slice thickness used for the image acquisition in previous studies, our results for the GFMs spatial position were similar.<sup>37,40</sup> The TPR of our method was determined to be 84% which was larger than the TPR for the bTFE alone but smaller than the TPR determined for multiparametric MRI.<sup>40</sup>

The detection performance results from the human observational study showed that MEGRE images could be a valid approach for identifying GFMs. The mean absolute difference in the internal distances of the true-positive GFMs between CT and MRI determined in the observational study was similar to the results of previous manual detection studies reporting  $0.6 \pm 0.4$  and  $0.6 \pm 0.6$  mm.<sup>25,37</sup>

Multiecho gradient echo with sum of squares echo combination for echo averaging has previously been shown to enhance detection of I25-Iodine seeds and GFM. It was concluded that multiple echoes for GRE provided better detection performance than both conventional FSE and single echo GRE.<sup>22</sup> In our study MEGRE was used without echo combination. Previous study states that the presence of air pockets such as rectal gas could obstruct the GFM detection using bTFE.<sup>40</sup> The use of image data acquired at multiple TEs for manual GFM detection can be beneficial for patients with rectal gas induced artifacts as these artifacts are mitigated for lower TEs (Fig. 2). By the same principle this could benefit patients with metallic hip prosthesis. Furthermore, by not doing echo averaging the image features, such as area increase with increasing TE, can remain unimpaired and recognized by a human eye.

The increasing area of the GFM signal void with respect to increasing TE in our work was due to the large difference in magnetic susceptibility between the GFM and surrounding tissue combined with a larger effect from T2\* relaxation for larger TEs.

Due to the remaining variety of image contrast, noise and artifacts among the patient data after MRI vendor-based image homogenization (SCIC, Table I), the use of an adaptive segmentation method<sup>41</sup> was crucial. For the purpose of this work, the adaptive segmentation method was superior compared to a global thresholding method.<sup>44</sup> An accurate automatic segmentation of the signal void area was crucial

for calculating a representative area slope and roundness. The actions above were not always sufficient to accomplish this for all echoes. This contributed to an error in the calculation of roundness and area slope, leading to an increase in false-negative candidate count.

If the long axis of the GFM marker is parallel with the B0 field and orthogonal with respect to the imaging plane, the signal void artifact in the MEGRE images would be round in its shape. A scenario with deviations from these prerequisites would lead to a change in artifact shape.<sup>17</sup> Exclusions due to such a scenario was avoided by setting the lower limit for roundness to no more than 0.67. In three cases, the GFM candidate was not classified as round enough. This was most probable due to incorrect segmentation of the signal void.

The fractions of patients with intraprostatic calcifications  $\geq 2$  mm (FWHM) in the training and validation data were 10/20 and 29/40, respectively. This is larger than the fraction of one-third previously reported for intraprostatic calcifications  $> 2$  mm in diameter.<sup>36</sup> To reduce the number of false-positive GFM candidates, the existence of a signal void in the first echo of the MEGRE images, originating from the GFM candidate, was required (discrimination step 5). This was analogous to prioritizing objects with the largest magnetic susceptibility, i.e., the GFM.

The differentiation between GFM and other objects, such as intraprostatic calcification, relied on the assumption that the magnetic susceptibility, the area slope, and roundness were larger for GFMs. Previous studies support this assumption.<sup>17,18,43</sup> The pixelated nature of a digital image could affect the roundness calculation. The interpolation to  $1024 \times 1024$  pixels in-plane was performed to reduce such potential calculation errors.

The developed method provided a way to identify the GFM without the use of image registration. The consecutive order of the target delineation and MEGRE sequence was of importance to avoid a large patient displacement between the scans. The assumption of an unchanged frame of reference, i.e., patient or prostate displacement between the scans, might not always be true, but due to the larger extent of the signal voids in the MEGRE data for higher TEs, the method provided an intrinsic tolerance for some patient and prostate displacements. No cases of patient or prostate displacement were reported as an origin of failure in the method.

The exclusion of study patients due to large amounts of rectal gas could in the future be resolved by asking the patients to use a bowel relaxant agent prior to the examination to reduce bowel peristalsis.<sup>45</sup> Other means of mitigating the artifacts could be to increase the receiver bandwidth or change the direction of frequency encoding.

One of the motivations for developing an automatic method for GFM detection is the elimination of manual labor. The detection performance for the developed method, in terms of accuracy, did not reach 100%. The method could still provide valuable input in the prostate treatment planning process as it eliminates the need for image registration but at this stage visual inspection of the results is needed before proceeding to treatment.

With the prerequisite of signal voids from the GFM the proposed method could also be applied to large FOV images dedicated for synthetic CT generation. This is presently being used in an ongoing clinical study called MR-PROTECT (MR-Prostate Radiotherapy Excluding CT) for MRI only radiotherapy for prostate at our clinic. If FSE technique has been used for acquiring large FOV images, it is of importance to notice that a longer echo train will give rise to increased image blurring, potentially concealing the small signal voids.<sup>46</sup> Partial volume effects can also conceal the small signal voids and care must therefore be taken when choosing the acquisition voxel size and the length of the echo train.

The number of false-positive GFM candidates in the target delineation images could be reduced by implementing a prior knowledge model of the GFM volume. The use of such a model has been demonstrated in a previous automatic method.<sup>37</sup> Other means of improving the detection accuracy of GFM could be by magnetic susceptibility mapping or by providing positive contrast in the vicinity of the marker using off-resonance signals.<sup>29–32,47</sup> As MEGRE is a generic and available sequence on multiple vendor platforms this should be further explored for both automatic and manual GFM identification.

## 5. CONCLUSIONS

This study developed an automatic method for identifying gold fiducial markers in an MRI target delineation image, without the need for image registration. The differentiation and identification of gold fiducial markers was based on a multi-echo gradient echo MRI sequence which also showed good performance in a human observatory study. By using an automatic method, the manual workload can be reduced and several operator related sources of uncertainties can be eliminated or mitigated. For clinical practice, visual inspection of the results from the automatic method is needed at the current stage.

## ACKNOWLEDGMENTS

This work was partially funded by Vinnova, Sweden's innovation agency, through the national project Gentle Radiotherapy with grant number 2016-03847 and "Allmänna sjukhusets i Malmö Stiftelse för bekämpande av cancer". The authors also acknowledge the support given by the MRI technologists Senada Kapetanovic and Sveinung Groven throughout the study.

## CONFLICTS OF INTEREST

The authors have no relevant conflicts of interest to disclose.

<sup>a)</sup>Author to whom correspondence should be addressed. Electronic mail: christian.k.gustafsson@skane.se.

## REFERENCES

- Blomqvist L, Bäck A, Ceberg C, et al. MR in radiotherapy – An important step towards personalized treatment? Report from the SSM's scientific council on ionizing radiation within oncology. *SSM*;2013. 51; 2014. ISSN 2000-0456.
- Karlsson M, Karlsson MG, Nyholm T, Amies C, Zackrisson B. Dedicated magnetic resonance imaging in the radiotherapy clinic. *Int J Radiat Oncol Biol Phys*. 2009;74:644–651.
- Debois M, Oyen R, Maes F, et al. The contribution of magnetic resonance imaging to the three-dimensional treatment planning of localized prostate cancer. *Int J Radiat Oncol Biol Phys*. 1999;45:857–865.
- Jackson AS, Reinsberg SA, Sohaib SA, et al. Distortion-corrected T2 weighted MRI: a novel approach to prostate radiotherapy planning. *Br J Radiol*. 2007;80:926–933.
- Nyholm T, Nyberg M, Karlsson MG, Karlsson M. Systematisation of spatial uncertainties for comparison between a MR and a CT-based radiotherapy workflow for prostate treatments. *Radiat Oncol*. 2009;4:54.
- Dowling JA, Lambert J, Parker J, et al. An atlas-based electron density mapping method for magnetic resonance imaging (MRI)-alone treatment planning and adaptive MRI-based prostate radiation therapy. *Int J Radiat Oncol Biol Phys*. 2012;83:e5–e11.
- Korhonen J, Kapanen M, Keyrilainen J, Seppala T, Tenhunen M. A dual model HU conversion from MRI intensity values within and outside of bone segment for MRI-based radiotherapy treatment planning of prostate cancer. *Med Phys*. 2014;41:011704.
- Lambert J, Greer PB, Menk F, et al. MRI-guided prostate radiation therapy planning: investigation of dosimetric accuracy of MRI-based dose planning. *Radiother Oncol*. 2011;98:330–334.
- Siverson C, Nordstrom F, Nilsson T, et al. Technical note: MRI only prostate radiotherapy planning using the statistical decomposition algorithm. *Med Phys*. 2015;42:6090–6097.
- Edmund JM, Nyholm T. A review of substitute CT generation for MRI-only radiation therapy. *Radiat Oncol*. 2017;12:28.
- Kim J, Garbarino K, Schultz L, et al. Dosimetric evaluation of synthetic CT relative to bulk density assignment-based magnetic resonance-only approaches for prostate radiotherapy. *Radiat Oncol*. 2015;10:239.
- Tyagi N, Fontenla S, Zhang J, et al. Dosimetric and workflow evaluation of first commercial synthetic CT software for clinical use in pelvis. *Phys Med Biol*. 2017;62:2961–2975.
- Persson E, Gustafsson C, Nordström F, et al. MR-OPERA – A multi-center/multi-vendor validation of MRI-only prostate treatment planning using synthetic CT images. *Int J Radiat Oncol*. 2017. In press. <https://doi.org/10.1016/j.ijrobp.2017.06.006>.
- Korhonen J, Kapanen M, Sonke JJ, et al. Feasibility of MRI-based reference images for image-guided radiotherapy of the pelvis with either cone-beam computed tomography or planar localization images. *Acta Oncol*. 2015;54:889–895.
- Korhonen J. Magnetic resonance imaging -based radiation therapy – Methods enabling the radiation therapy treatment planning workflow for prostate cancer patients by relying solely on MRI-based images throughout the process [Doctoral dissertation 35/2015]. <http://urn.fi/URN:ISBN:978-952-60-6124-5>. Aalto University, Helsinki, Finland; 2015.
- Zangger K, Armitage LM. Silver and gold NMR. *Met Based Drugs*. 1999;6:239–245.
- Schenck JF. The role of magnetic susceptibility in magnetic resonance imaging: MRI magnetic compatibility of the first and second kinds. *Med Phys*. 1996;23:815–850.
- Port JD, Pomper MG. Quantification and minimization of magnetic susceptibility artifacts on GRE images. *J Comput Assist Tomogr*. 2000;24:958–964.
- Jonsson JH, Garpebring A, Karlsson MG, Nyholm T. Internal fiducial markers and susceptibility effects in MRI-simulation and measurement of spatial accuracy. *Int J Radiat Oncol Biol Phys*. 2012;82:1612–1618.
- Bowes D, Crook JM, Rajapakshe R, Araujo C, Parker B. Defining a magnetic resonance scan sequence for permanent seed prostate brachytherapy postimplant assessment. *Brachytherapy*. 2013;12:25–29.
- Kapur T, Egger J, Damato A, Schmidt EJ, Viswanathan AN. 3-T MR-guided brachytherapy for gynecologic malignancies. *Magn Reson Imaging*. 2012;30:1279–1290.
- Schieda N, Avruch L, Shabana WM, Malone SC. Multi-echo gradient recalled echo imaging of the pelvis for improved depiction of brachytherapy seeds and fiducial markers facilitating radiotherapy

- planning and treatment of prostatic carcinoma. *J Magn Reson Imaging*. 2015;41:715–720.
23. Vidakovic S, Jans HS, Alexander A, Sloboda RS. Post-implant computed tomography-magnetic resonance prostate image registration using feature line parallelization and normalized mutual information. *J Appl Clin Med Phys*. 2006;8:21–32.
  24. Bloch BN, Lenkinski RE, Helbich TH, et al. Prostate postbrachytherapy seed distribution: comparison of high-resolution, contrast-enhanced, T1- and T2-weighted endorectal magnetic resonance imaging versus computed tomography: initial experience. *Int J Radiat Oncol Biol Phys*. 2007;69:70–78.
  25. Kapanen M, Collan J, Beule A, Seppala T, Saarilahti K, Tenhunen M. Commissioning of MRI-only based treatment planning procedure for external beam radiotherapy of prostate. *Magn Reson Med*. 2013;70:127–135.
  26. Tanaka O, Komeda H, Iida T, et al. Fiducial marker for prostate radiotherapy: comparison of 0.35- and 0.5-mm-diameter computed tomography and magnetic resonance images. *Radiol Med*. 2017;122:204–207.
  27. Katayama N, Takemoto M, Yoshio K, et al. T2\*-weighted image/T2-weighted image fusion in postimplant dosimetry of prostate brachytherapy. *J Radiat Res*. 2011;52:680–684.
  28. Ohashi T, Momma T, Yamashita S, et al. Impact of MRI-based postimplant dosimetric assessment in prostate brachytherapy using contrast-enhanced T1-weighted images. *Brachytherapy*. 2012;11:468–475.
  29. de Leeuw H, Seevinck PR, Bakker CJ. Center-out radial sampling with off-resonant reconstruction for efficient and accurate localization of punctate and elongated paramagnetic structures. *Magn Reson Med*. 2013;69:1611–1622.
  30. Dong Y, Chang Z, Xie G, Whitehead G, Ji JX. Susceptibility-based positive contrast MRI of brachytherapy seeds. *Magn Reson Med*. 2015;74:716–726.
  31. Kuo N, Lee J, Tempny C, Stuber M, Prince J. MRI-based prostate brachytherapy seed localization. *Proc IEEE Int Symp Biomed Imaging*. 2010;2010:1397–1400.
  32. Seevinck PR, de Leeuw H, Bos C, Bakker CJ. Highly localized positive contrast of small paramagnetic objects using 3D center-out radial with off-resonance reception. *Magn Reson Med*. 2011;65:146–156.
  33. Dowling JA, Sun J, Pichler P, et al. Automatic substitute computed tomography generation and contouring for magnetic resonance imaging (MRI)-alone external beam radiation therapy from standard MRI sequences. *Int J Radiat Oncol Biol Phys*. 2015;93:1144–1153.
  34. Greer PB, Dowling JA, Lambert JA, et al. A magnetic resonance imaging-based workflow for planning radiation therapy for prostate cancer. *The Medical Journal of Australia*. 2011;194:S24–S27.
  35. Barentsz JO, Richenberg J, Clements R, et al. ESUR prostate MR guidelines 2012. *Eur Radiol*. 2012;22:746–757.
  36. Zeng GG, McGowan TS, Larsen TM, et al. Calcifications are potential surrogates for prostate localization in image-guided radiotherapy. *Int J Radiat Oncol Biol Phys*. 2008;72:963–966.
  37. Ghose S, Mitra J, Rivest-Henault D, et al. MRI-alone radiation therapy planning for prostate cancer: automatic fiducial marker detection. *Med Phys*. 2016;43:2218.
  38. Fernandes CD, Dinh C, Ter Beek LC, et al. OC-0157: prostate fiducial markers detection with the use of multiparametric-MRI. *Radiother Oncol*. 2016;119:S72–S73.
  39. Murphy G, Haider M, Ghai S, Sreeharsha B. The expanding role of MRI in prostate cancer. *AJR Am J Roentgenol*. 2013;201:1229–1238.
  40. Dinis Fernandes C, Dinh CV, Steggerda MJ, et al. Prostate fiducial marker detection with the use of multi-parametric magnetic resonance imaging. *Phys Imaging Radiat Oncol*. 2017;1:14–20.
  41. Bradley D, Roth G. Adaptive thresholding using the integral image. *Journal of Graphics, GPU, and Game Tools*. 2007;12:13–21.
  42. McRobbie DW. *MRI from Picture To Proton*, 2nd ed. Cambridge; New York, NY: Cambridge University Press; 2007.
  43. Olsrud J, Latt J, Brockstedt S, Romner B, Bjorkman-Burtscher IM. Magnetic resonance imaging artifacts caused by aneurysm clips and shunt valves: dependence on field strength (1.5 and 3 T) and imaging parameters. *J Magn Reson Imaging*. 2005;22:433–437.
  44. Otsu N. A threshold selection method from gray-level histograms. *IEEE Trans Syst Man Cybern*. 1979;9:62–66.
  45. Rosenkrantz AB, Taneja SS. Radiologist, be aware: ten pitfalls that confound the interpretation of multiparametric prostate MRI. *AJR Am J Roentgenol*. 2014;202:109–120.
  46. Mugler JP 3rd. Optimized three-dimensional fast-spin-echo MRI. *J Magn Reson Imaging*. 2014;39:745–767.
  47. Schmidt MA, Payne GS. Radiotherapy planning using MRI. *Phys Med Biol*. 2015;60:R323–R361.

Paper IV





# Using C-Arm X-ray images from marker insertion to confirm the gold fiducial marker identification in an MRI-only prostate radiotherapy workflow

Christian Gustafsson<sup>1,2</sup> | Emilia Persson<sup>1,2</sup> | Adalsteinn Gunnlaugsson<sup>1</sup> | Lars E. Olsson<sup>1,2</sup>

<sup>1</sup>Department of Hematology, Oncology and Radiation Physics, Skåne University Hospital, Lund, Sweden

<sup>2</sup>Department of Translational Medicine, Medical Radiation Physics, Lund University, Malmö, Sweden

Author to whom correspondence should be addressed. Christian Gustafsson  
E-mail: christian.k.gustafsson@skane.se

#### Funding information

VINNOVA Gentle Radiotherapy, Grant/Award Number: 2016-03847, 2016-02529

#### Abstract

Prostate cancer radiotherapy workflows, solely based on magnetic resonance imaging (MRI), are now in clinical use. In these workflows, intraprostatic gold fiducial markers (GFM) show similar signal behavior as calcifications and bleeding in T2-weighted MRI-images. Accurate GFM identification in MRI-only radiotherapy workflows is therefore a major challenge. C-arm X-ray images (CkV-images), acquired at GFM implantation, could provide GFM position information and be used to confirm correct identification in T2-weighted MRI-images. This would require negligible GFM migration between implantation and MRI-imaging. Marker migration was therefore investigated. The aim of this study was to show the feasibility of using CkV-images to confirm GFM identification in an MRI-only prostate radiotherapy workflow. An anterior-posterior digitally reconstructed radiograph (DRR)-image and a mirrored posterior-anterior CkV-image were acquired two weeks apart for 16 patients in an MRI-only radiotherapy workflow. The DRR-image originated from synthetic CT-images (created from MRI-images). A common image geometry was defined between the DRR- and CkV-image for each patient. A rigid registration between the GFM center of mass (CoM) coordinates was performed and the distance between each of the GFM in the DRR- and registered CkV-image was calculated. The same methodology was used to assess GFM migration for 31 patients in a CT-based radiotherapy workflow. The distance calculated was considered a measure of GFM migration. A statistical test was performed to assess any difference between the cohorts. The mean absolute distance difference for the GFM CoM between the DRR- and CkV-image in the MRI-only cohort was  $1.7 \pm 1.4$  mm. The mean GFM migration was  $1.2 \pm 0.7$  mm. No significant difference between the measured total distances of the two cohorts could be detected ( $P = 0.37$ ). This demonstrated that, a C-Arm X-ray image acquired from the GFM implantation procedure could be used to confirm GFM identification from MRI-images. GFM migration was present but did not constitute a problem.

PACS  
87.55.Qr

This is an open access article under the terms of the Creative Commons Attribution License, which permits use, distribution and reproduction in any medium, provided the original work is properly cited.

© 2018 The Authors. *Journal of Applied Clinical Medical Physics* published by Wiley Periodicals, Inc. on behalf of American Association of Physicists in Medicine.

## KEY WORDS

gold fiducial markers, MRI-only prostate, MRI-only radiotherapy, synthetic CT

## 1 | INTRODUCTION

The use of magnetic resonance imaging (MRI) for target delineation in prostate cancer radiotherapy is widespread due to the superior soft tissue contrast of MRI compared to computed tomography (CT). In a conventional radiotherapy workflow for prostate, CT, and MRI are used in combination by registering the images into a common frame of reference.

Prostate external beam radiotherapy workflows where CT is excluded and solely based on MRI, referred to as an MRI-only radiotherapy workflow, have now been introduced into the clinic.<sup>1,2</sup> Systematic uncertainties such as image registration errors between CT and MRI could thereby be eliminated.<sup>3,4</sup> The impact on target and organ at risk delineation due to anatomical changes between CT and MRI examination, such as bladder and rectum filling, could also be avoided.

The Hounsfield units of the tissues in an MRI-only radiotherapy workflow are calculated from the MRI-images and the resulting images are referred to as a synthetic CT (sCT). Currently, two commercial solutions for prostate sCT generation exist, Philips MRCAT and Spectronic MRIPlanner.<sup>5,6</sup> Both solutions have been independently validated and have been or are being used in clinical studies.<sup>1,7,8</sup> Multiple other solutions for generating a sCT have been presented and were recently reviewed.<sup>9</sup>

An MRI-only radiotherapy workflow introduces several challenges. One, which will be investigated in this paper, is identification of gold fiducial markers (GFM), inserted into the prostate for target positioning. The GFM has high electron density and will exhibit increased X-ray attenuation, generating streak artefacts in the CT-images, mainly caused by inaccurate beam-hardening correction in the CT-image reconstruction.<sup>10</sup> The identification of GFM in CT-images, in which they cannot be mistaken for calcifications or bleeding, is therefore a straightforward process.<sup>11</sup>

In T2-weighted (T2w) MRI-images, GFM, calcifications and bleeding will have similar signal behavior and be depicted as signal voids.<sup>11–15</sup> This makes differentiating between these objects a challenging task using solely MRI-images in an MRI-only radiotherapy workflow.

A common method for identifying GFM using MRI-images alone is to exploit the difference in magnetic susceptibility between the surrounding tissue and GFM.<sup>5,11,12,14–16</sup> An increased sensitivity to susceptibility effects can be achieved by using gradient echo based MRI sequences.<sup>17</sup> The resulting shape and size of the signal void from the GFM will not only be dependent on the nature of the MRI sequence and acquisition parameters, but also on the shape and orientation of the GFM.<sup>16,18</sup>

In the previous study, the use of magnetic resonance multi-echo gradient echo images for GFM identification was suggested.

In a human observation study with four observers and 40 patients the sensitivity, specificity, and accuracy of GFM identification in T2w target delineation MRI-images were determined to be 98%, 94%, and 97%, respectively.<sup>11</sup> This is similar to human observation studies using other MRI acquisition techniques, which had a detection accuracy between 93% and 98%.<sup>2,12,14,15,19</sup> For a safe and reliable clinical implementation of an MRI-only radiotherapy workflow, the GFM identification method should ideally have a detection accuracy of 100%. None of the human observation studies for GFM identification available in the literature have, to the best of our knowledge, reached this detection accuracy. In previous studies, describing clinical workflows for MRI-only radiotherapy of the prostate, CT was still used for identifying GFM or to differentiate permanent brachytherapy seeds from GFM.<sup>1,2</sup> Several ways to increase the redundancy of the GFM identification procedure, thereby increasing the identification accuracy, were recently proposed.<sup>19</sup> The need for improved and cost-effective GFM identification methods therefore seems evident.

While awaiting improved MR-based methods for GFM identification when CT is not available, a complementary method to confirm correct MRI-based identification of GFM could be used. C-arm X-ray imaging is often used in the clinic, including ours, to validate a successful GFM implantation. We suggest that the GFM position information from the X-ray images could be used to differentiate GFM from other objects in the MRI-images. No additional imaging or changes to the workflow would then be required to validate the GFM identification.

The usefulness of this information relies on the assumption of negligible GFM migration between GFM insertion and imaging of the patient for prostate radiotherapy treatment planning purposes. Mean marker migration has previously been reported to be 0.8 (daily)–1.2 mm (over the entire treatment course).<sup>20,21</sup>

The aim of this work was to show the feasibility of using C-Arm X-ray images from the GFM implantation procedures to confirm the GFM identification performed using MRI-images in an MRI-only prostate radiotherapy workflow.

## 2 | METHODS

### 2.A | Patient selection and gold fiducial marker implantation

The first 16 patients in an ongoing MRI-only prostate radiotherapy study named MR-PROTECT (MR-only Prostate RadioTherapy Excluding CT), representing all data available at the time, were selected for investigation. The patients were prescribed 39 fractions of 2 Gy over 8 weeks. Mean weight ( $n = 16$ ) was  $85.1 \pm 10.5$  kg [ $62.0$ – $106.0$  kg] and mean age  $71.1 \pm 5.0$  yr [ $60.0$ – $81.0$  yr]. Ten



patients underwent ultrasound guided transperineal prostatic implantation of GFM, performed by three different oncologists. Six patients underwent ultrasound guided transrectal implantation, performed by one oncologist. The same type of GFM was used for both implantation methods. One objective, during GFM implantation, was to place the GFM in different areas of the prostate. This could help avoid GFM overlap on orthogonal kilovoltage (kV)-images, used for patient positioning. This configuration created internal GFM distances of around 2–3 cm, depending on the size of the prostate. No CT data from these patients were used in this study.

As negligible GFM migration was a crucial assumption for the method to work it was of importance to study the migration of the specific GFM type used. To assess the possible impact of GFM migration, a different patient cohort from a conventional CT-based prostate radiotherapy workflow was selected for investigation. This patient cohort consisted of 33 patients who all underwent ultrasound guided transperineal prostatic implantation of GFM, performed by two different oncologists. One patient was excluded due to loss of GFM and one patient was excluded due to two GFM being inserted too close to each other. Mean weight ( $n = 31$ ) was  $84.9 \pm 10.9$  kg [62.0–108.0 kg] and mean age  $72.9 \pm 4.8$  yr [60.0–81.0 yr]. No MRI or sCT data from these patients were used in this study.

The GFM consisted of three in-house produced inferior–superior long axis-oriented cylinder-shaped gold objects (length 5.0 mm and diameter 1.0 mm) and were implanted 2 weeks prior to MRI- or CT-imaging. Choice of GFM type was according to the clinic's standard. The study was approved by the regional ethics board with diary number 2013/742, complemented by diary number 2016/801.

## 2.B | Imaging and identification of gold fiducial markers

In connection to the GFM implantation procedure, one posterior-anterior (PA) X-ray image was acquired from a portable Ziehm Vision FD Vario 3D C-Arm X-Ray system (Ziehm Imaging, ZiehmNetPort, Nuremberg, Germany, software version 5.22) with peak kilovoltage output 60–110 kVp, tube current 6–16 mA, rectangular FOV-, and 5 mm aluminum filter setting). The PA X-ray image was, after image acquisition, oriented by the X-ray system as an AP-image by left-right mirroring. All patients undergoing transperineal implantation were imaged in a lithotomy position with the legs placed in a leg support (Fig. 1). For transrectal implantation, the patients were positioned on their side during the implantation and imaged in a supine position with their legs stretched out. The C-Arm rotation was manually adjusted to a zero degree angle with respect to the patient table, indicated by an analogue protractor scale on the C-arm (Fig. 1). The actual C-arm angle used was recorded in the image DICOM header. The C-arm X-ray image is hereby referred to as the CkV-image. The GFM were visualized as low signal intensity objects in the image (Fig. 2[b]).

The transversal sCT-images used in the MR-PROTECT study were created from large field of view turbo spin echo T2w MRI-

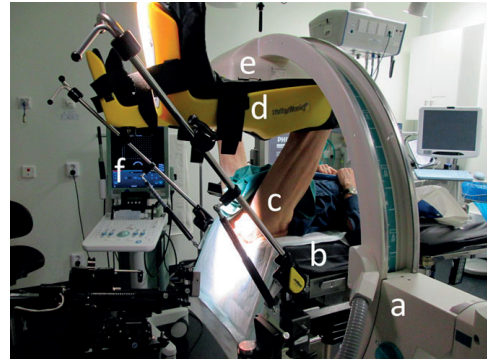


**Fig. 1.** C-arm X-ray patient positioning. The patient (c) was placed in a lithotomy position during the transperineal ultrasound (f) guided implantation of the GFM. The legs were fixated using a leg support (d). The C-Arm X-ray system (a), with the X-ray detector (e), was placed in a zero degree angle with respect to the patient table (b) to acquire a posterior-anterior X-ray for a successful GFM implantation verification.

images with a scan slice thickness of 2.5 mm and  $0.7 \text{ mm} \times 0.6 \text{ mm}$  in-plane scan resolution using the conversion software Spectronic MriPlanner version 1.1.2 (Spectronic Medical, Helsingborg, Sweden). The software and the MRI imaging protocol were recently validated against CT.<sup>22,23</sup> In the MR-PROTECT study, the center of mass (CoM), for each GFM in each patient, was manually identified in the sCT geometry using Eclipse Treatment Planning system version 13.6 (Varian Medical Systems, Palo Alto, CA, USA). The identification of GFM in the T2w MRI-images, i.e., sCT geometry, was aided by multi-echo gradient echo MRI-images.<sup>11</sup> The determined GFM CoM coordinates were used by Spectronic MriPlanner to burn in synthetic markers onto the sCT-images (slice thickness 2.5 mm,  $0.4 \text{ mm} \times 0.3 \text{ mm}$  in-plane resolution). The synthetic markers were depicted as round 2-D high intensity objects, defined in one slice each, with a diameter of 4 mm. Correct positioning of the synthetic markers in the sCT-images, created in the MR-PROTECT study, was verified prior to the treatment.

CT-images were, for the patients in the conventional CT-based prostate radiotherapy workflow (to assess GFM migration), acquired with a Siemens Somatom Definition AS+ (Siemens Healthcare, Forchheim, Germany), slice thickness 3 mm, reconstructed diameter 500 mm, reconstructed in plane resolution  $0.98 \text{ mm} \times 0.98 \text{ mm}$ , peak kilovoltage output 120 kVp, exposure time 500 ms and tube current 213–660 mA using CareDose.

Anterior-posterior (AP) oriented digitally reconstructed radio-graphs (DRR) with isotropic pixel resolution using a  $512 \times 512$  matrix were created from CT and sCT at a gantry angle of 0 degrees using the Eclipse Treatment Planning System. The DRR from the CT and sCT is hereby referred to as CTDRR and sCTDRR, respectively.

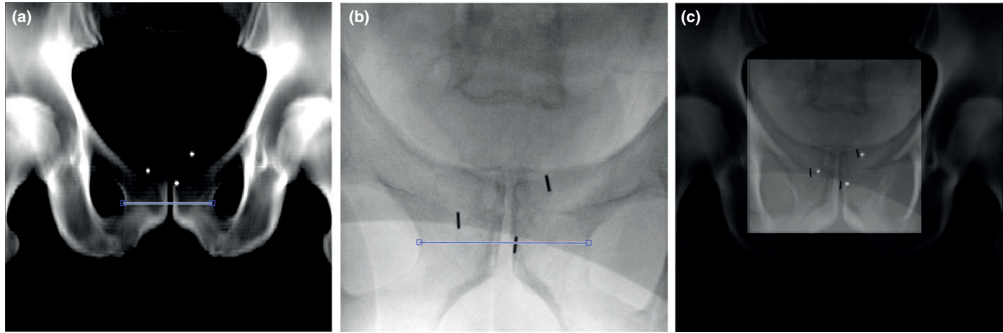


**FIG. 2.** DRR- and CkV-image. Anterior-posterior DRR-image generated from sCT with burned in synthetic markers (a), mirrored posterior-anterior CkV-image acquired in connection to GFM implantation (b). The CkV-image scaling was performed by measuring a horizontal distance from left to right over the pubic symphysis in the DRR- and CkV-image (line in a and b). After the CkV-image was rescaled to the geometry of the DRR, it was manually registered (translation only) using the GFM as a visual aid and overlaid (c).

## 2.C | Image processing and analysis

Image processing and analysis were performed using an in-house developed MATLAB program with a graphical user interface (version R2017a, Mathworks Inc., Natick, MA, USA). The steps described below were applied to both sCTDRR, CTDRR, and the corresponding CkV-image (Figs. 2 and 3).

Generation of a common geometric frame of reference between the DRR and CkV-images was necessary due to the different image modality origin. The DICOM information from the CkV-image did not contain information about the spatial resolution of the image. For each patient, the CkV-image was scaled to the image resolution of the DRR with an in-house developed method. The scaling was performed by measuring a horizontal distance from left to right over the pubic symphysis in the DRR with start and stop points defined in the left-right interface between the obturator foramen and the body of pubic bone (Fig. 2). The corresponding distance in the CkV-image was identified and image rescaling was performed using bicubic interpolation.<sup>24</sup> To quantify the uncertainty in the determination of the image scale factor, horizontal distance measurements in the DRR- and CkV-image were, by one user, repeated 15 times each for three random patients, selected from the sCTDRR cohort. The largest coefficient of variation (CV) in the image scale factor among the three patients was considered to be a measure of scale factor uncertainty. All distance measurements were performed with a resolution superior to the inherent image resolution.

The rescaled CkV-image was visually overlaid onto the DRR-image using a translational manual registration using the GFM as visual guidance. This was performed in order to supply the point cloud registration (see later steps) with information on point-coupling for the three GFM in the DRR- and CkV-image.

The GFM was automatically identified in the DRR-image by first masking a rectangular area positioned around the central part of the

pelvis containing the GFM. The masked DRR-image was binarized using a threshold chosen to suppress non-GFM objects. The 2-D connected components with a connectivity of at least eight pixels were identified. A discrimination of the identified connected components using prior knowledge of the upper and lower GFM object size in the image was performed and the CoM of the GFM was determined (Fig. 3).

The GFM was automatically identified in the scaled CkV-image by first masking the image using the previously defined DRR-mask (expecting similar image geometry). The masked scaled CkV-image was normalized, inverted, and binarized using Otsu's segmentation method.<sup>25</sup> The selection of GFM and the determination of the CoM were performed using the same techniques as for the DRR-image described above. (Fig. 3).

For each DRR- and CkV-image, a point cloud was defined from the GFM CoM coordinates. A point cloud is a set of data points containing spatial coordinates. Each point cloud in this study had three data points containing the three GFM CoM 2-D coordinates. A rigid transformation between the two point clouds was calculated using an iterative closest point algorithm.<sup>26</sup> The transformation was applied to the GFM CoM coordinates for the CkV-image. Visual inspection of the GFM CoM point-clouds was performed after the point-cloud transformation (Fig. 3).

The absolute total difference in CoM between each of the GFM in the DRR-image and the rigidly transformed GFM CoM coordinates for the scaled CkV-image was calculated as a total distance and a distance in the directions left-right and inferior-superior. The absolute total distances calculated for patients in the conventional CT-based prostate radiotherapy workflow was considered to be a measure of GFM migration.

To assess if there was a difference in the measured absolute total distance between the GFM in the sCTDRR and CkV compared to CTDRR and CkV, a nonparametric two-sided independent Mann-Whitney U-test<sup>27</sup> with a 5% significance level was used.

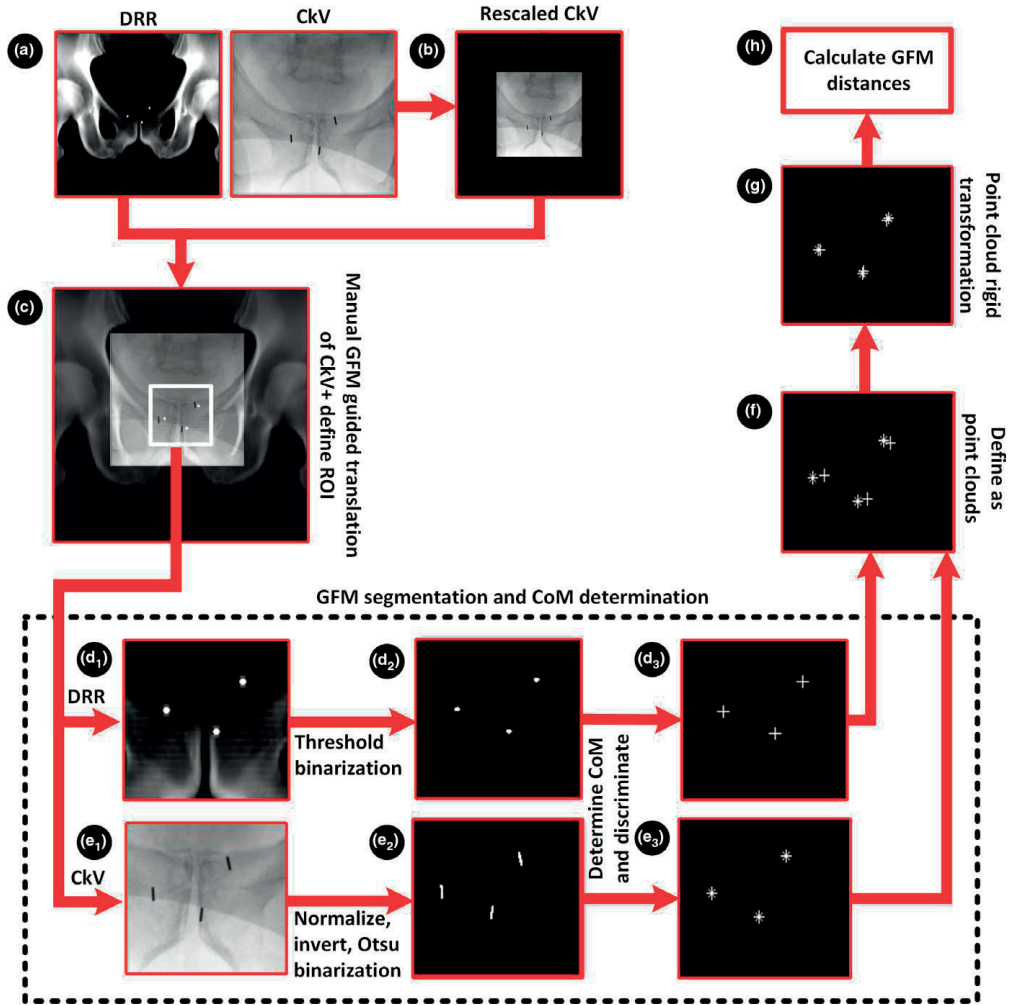


**FIG. 3.** Workflow for the proposed method (a) sCTDRR- and CkV-image was acquired, (b) the CkV-image was rescaled to the image resolution of the sCTDRR-image, (c) the rescaled CkV-image was visually and manually overlaid onto the sCTDRR-image and a rectangular ROI around the GFM was defined and used as an image mask, (d<sub>1-2</sub>) the masked sCTDRR-image was binarized using a threshold chosen to suppress non-GFM objects, (e<sub>1-2</sub>) the masked scaled CkV-image was normalized, inverted and binarized using Otsu's segmentation method,<sup>25</sup> (d<sub>2</sub>) and (e<sub>2</sub>) the 2-D connected components in the binarized sCTDRR- and CkV-image were identified, a discrimination of the identified connected components was performed and the CoM of the GFM was determined, (f) the GFM CoM coordinates in the sCTDRR- and CkV-image defined two point clouds, (g) a rigid transformation between the point clouds was calculated, (h) the distances between each GFM in the registered point clouds were calculated. The same workflow (a-h) was applied to CTDRR to assess GFM migration.

### 3 | RESULTS

Using the proposed method together with visual inspection, all GFM in the sCTDRR cohort were confirmed to have been previously correctly identified. The mean absolute total difference in CoM

displacement between the GFM for sCTDRR- and CkV-image was 1.7 mm (1 SD = ±1.4 mm) (Table 1). Patient 11 in the sCTDRR cohort had the largest absolute distance difference, observed in one of the GFM, located in the inferior-superior direction (6.3 mm). This distance difference was larger than three standard deviations from

**TABLE 1** Mean absolute difference in CoM between the GFM in the DRR-image and the rigidly registered scaled CkV-image. Data are presented for patients in an MRI-only prostate radiotherapy workflow (sCTDRR vs CkV). GFM migration data are presented for patients in a conventional CT-based prostate radiotherapy workflow (CTDRR vs CkV). The absolute difference in the directions left-right, inferior-superior, and in total is denoted by  $\Delta X$ ,  $\Delta Y$ , and  $\Delta Total$ .

|                        | Mean (mm) | SD (mm) | Median (mm) | Minimum (mm) | Maximum (mm) |
|------------------------|-----------|---------|-------------|--------------|--------------|
| CTDRR vs CkV (n = 31)  |           |         |             |              |              |
| $\Delta X$             | 0.9       | 0.7     | 0.8         | 0.0          | 3.2          |
| $\Delta Y$             | 0.6       | 0.5     | 0.4         | 0.0          | 2.1          |
| $\Delta Total$         | 1.2       | 0.7     | 1.1         | 0.0          | 3.2          |
| sCTDRR vs CkV (n = 16) |           |         |             |              |              |
| $\Delta X$             | 0.8       | 0.7     | 0.7         | 0.0          | 2.8          |
| $\Delta Y$             | 1.3       | 1.4     | 0.7         | 0.0          | 6.3          |
| $\Delta Total$         | 1.7       | 1.4     | 1.2         | 0.1          | 6.3          |

the mean of 1.7 mm. This raised a concern regarding a potential erroneous identification of one GFM and the cause of this outlier was investigated. It could, without any additional imaging, be concluded that it was due to the large marker migration (see Section 4).

The mean GFM migration was determined from the CTDRR cohort as the mean absolute total distance difference between the CTDRR and CkV image (1.2 mm (1SD =  $\pm 0.7$  mm)). The mean and standard deviation for the absolute total distance difference were smaller for the CTDRR cohort compared to the sCTDRR cohort (Table 1).

The mean image scale factor with one SD and CV for the three random patients, randomly selected from the sCTDRR cohort, was  $4.35 \pm 0.043$  [4.28–4.42] CV = 1.0% (n = 15),  $3.56 \pm 0.024$  [3.52–3.60] CV = 0.7% (n = 15), and  $3.66 \pm 0.032$  [3.62–3.72] CV = 0.9% (n = 15). The uncertainty determination for the image scale factor was therefore estimated to be 1%.

No statistically significant difference in the measured total distances of the GFM in the sCTDRR and CkV compared to CTDRR and CkV could be detected ( $P = 0.37$ ). The mean absolute total distance in the sCTDRR cohort (1.7 mm) could therefore not be separated from possible GFM migration effects. The distance of 1.7 mm was therefore considered as a small and acceptable distance in the proposed method.

Three patients in the sCTDRR cohort had deviations of one, three, and five degrees, respectively, from the desired C-Arm zero degree angle setting, which led to non-perfect PA imaging projections. For the CTDRR cohort, four patients had a deviation of one degree. The angle deviations from zero degrees were believed to be the cause of human error.

## 4 | DISCUSSION

The developed method demonstrated the feasibility of using a single CkV-image from the fiducial implantation procedure to confirm the GFM identification performed in an MRI-only prostate radiotherapy

workflow. The method was dependent on calculating and evaluating the distance between each of the GFM in the CkV-image and a DRR-image created from sCT-images in the MRI-only radiotherapy workflow.

The spatial accuracy for manual and automatic GFM identification methods, solely using MRI-images, has previously been reported to be sufficient but, due to prostatic calcifications and bleeding, the detection accuracy has been insufficient.<sup>1,11–15,19</sup> From the results of this study and with discussed uncertainties in mind, our proposed method can detect if errors in the GFM identification process have occurred. This routine could be applied to both manual and automatic GFM identification frameworks.

To assess the impact of GFM migration, specific to the GFM type and imaging schedule used in our clinic, the method was applied to DRR- and CkV-images for 31 patients, included in a conventional CT-based prostate radiotherapy workflow. A statistical difference between the accuracy with respect to GFM displacement in the MRI-only workflow and conventional CT-based workflow could not be detected. The mean absolute total distance in the sCTDRR cohort (1.7 mm) could therefore not be separated from possible GFM migration effects.

GFM migration effects could explain a major part of the mean absolute total distance difference measured in the sCTDRR cohort (1.7 mm). Further, it has been shown that the mean geometric accuracy to which 3–5 mm cylindrical GFM (oriented parallel to the magnetic field) can be identified in spin echo based target delineation MRI-images is around 1 mm (1 SD = 1 mm).<sup>11,18</sup> As the sCT-images inherit the geometry from the full field of view T2w MRI-images, the same geometric accuracy can be expected for the synthetic markers in the sCT-images. The synthetic markers in the sCTDRR-images, created from the sCT-images, will therefore also be affected. With these discussion points in mind and a GFM inter-distance of about 2–3 cm, a mean absolute total distance of 1.7 mm between the sCTDRR- and CkV-image could be regarded as small enough for the method to be used as a QA tool for GFM identification.

The measured mean absolute total distance difference in the CTDRR cohort for marker migration assessment is believed to consist of GFM migration in combination with inherent uncertainties in the current evaluation method. These uncertainties could arise due to measurement errors in the image scaling involving manual selection of start and stop points, the elevated patient leg position for CkV-imaging or a non-perfect CkV-image PA projection of the patient anatomy (three patients deviated from a zero degree C-arm angle setting). The same inherent uncertainties were assumed to exist in the sCTDRR cohort. Measured distances from the CTDRR cohort were, however, similar compared to previously reported mean values of 0.8–1.2 mm GFM migration.<sup>20,21</sup> This suggests that the inherent uncertainties in the proposed evaluation method could be considered minor and the dominating effect in the measurements of the CTDRR cohort was due to GFM migration.

Implantation of the GFM for the patients in the sCTDRR cohort was performed using both transrectal and transperineal procedures while patients in the CTDRR cohort was only subjected to transperineal based implantation procedure. The difference in the

implantation procedures is not expected to affect GFM migration<sup>28,29</sup> and therefore not the results in this study either.

The rescaling of the CkV-image to the geometry of the sCTDRR cohort depended on defining a distance within a bone structure (Fig. 2). A sCT-image might not depict those bones with the same amount of details and geometric fidelity as a CT-image. The scaling of the CkV-image in the sCTDRR cohort would then be affected. The uncertainty for the image scale factor was measured and estimated to be as small as 1%. Further, the creation of sCTDRR was not optimized as the default clinic DRR creation settings for CT was used (not sCT adapted). It is possible that these factors have contributed to the measurement of absolute total difference in GFM distances for the sCTDRR cohort. These contributions are, however, considered minor.

Recently, CT was still used for identification of GFM in clinical workflows for MRI-only radiotherapy of the prostate.<sup>1,2</sup> With the method proposed in our study, the use of CT would not be necessary. The proposed method could potentially also be used to mitigate the recently suggested need for redundant processes in GFM identification.<sup>19</sup>

If the assumption of negligible GFM migration between GFM insertion and MRI imaging of the patient was not fulfilled, the spatial GFM position correlation for a GFM, imaged at different time points with different modalities, would be weaker. This would make it harder to detect an incorrectly identified GFM using the proposed method. Patient 11 in the sCTDRR cohort had a large (6.3 mm) absolute distance difference for one of the GFM. Through review of the previously acquired multi-echo gradient echo MRI-images<sup>11</sup> or using RT kV-images from the first treatment fraction, it could be concluded that the deviation was due to an actual GFM migration in the inferior-superior direction. The large migration was believed to be a result of a complication during the implantation procedure.

Another situation with imperfect GFM implant geometry could occur if multiple GFM overlap in the projection image. One of the objectives during GFM implantation is to avoid such a scenario. Unfortunately, one patient in the CTDRR-cohort was excluded due to inability to separate overlapping GFM. This limitation can be resolved with a lateral CkV-image.

The rigid point cloud registration used in this method depended on an iterative closest point (ICP) algorithm which used minimization of the mean squared distance as optimization metric. If all GFM migrated the same distance in the same direction, the algorithm would be unable to differentiate between GFM migration and prostate movement. Migration would then not be detected. The algorithm also assumes no GFM to be stationary in its position. This implies that if only one GFM migrated and the others did not, the migration distance would be underestimated. These scenarios are, however, not considered likely to occur and are not regarded as potential issues.

The rigid point cloud registration accounted for in-plane prostate rotation but the image information in the single PA CkV-image limited the ability to detect and correct arbitrary prostate rotation between GFM implantation and MRI-imaging. This did, however, not seem to constitute a notable problem for the proposed method.

The measured absolute difference in GFM CoM between the DRR- and CkV-image for the two cohorts was similar in the left-right component. The largest directional difference and variation were found in the inferior-superior component for the sCTDRR cohort (Table 1). The dominating factor for this is believed to be an effect of the prior manual identification of the GFM CoM in the transversal large field of view T2w MRI-image (originating from the MR-PROTECT study) — as the GFM CoM was forced to be positioned in an existing transversal slice (not in between any slices). This limited the spatial resolution in determining the CoM in slice direction (patient inferior-superior). This limitation propagated to an uncertainty of the GFM CoM in the inferior-superior direction of the AP sCTDRR. A reduced slice thickness of the T2w MRI-image (assuming unchanged image quality) would yield an improved spatial accuracy for the manual GFM identification.

The determination of the CoM of the GFM in the CTDRR used image interpolation between the image slices, was not dependent on any prior manual identification steps, and was not subjected to the above problem with limited spatial resolution (other than slice thickness). It is believed that this effect largely contributed to the numerical difference in the measured mean absolute total difference and uncertainties for the two cohorts.

The mean absolute distance difference between the GFM for sCTDRR- and CkV-image was 1.7 mm (1 SD =  $\pm 1.4$  mm). The mean value with additional two standard deviations adds up to 4.5 mm. Given the experimental conditions discussed and the results of this study, the authors therefore suggest that a non-acceptable distance difference between the GFM in the sCTDRR- and CkV-image for the proposed method is greater than 5 mm.

In the event of detecting a non-acceptable distance difference between the sCTDRR- and CkV-image the user should reevaluate the MRI-images to see if any calcifications or other similar objects exist in the vicinity of the determined GFM signal void. If not, actual GFM migration can be concluded. A multi-echo gradient echo MRI acquisition technique can facilitate this task<sup>11</sup> and this approach proved to be successful for the assessment of the large migration in one of the GFM for patient 11 in the sCTDRR cohort.

The image information from a PA CkV-image did not enable a full 3-D verification of the GFM positions and this constituted a limitation in the proposed method. However, in our suggested prostate MRI-only radiotherapy workflow, a last verification step is performed at the first radiotherapy fraction where orthogonal kV-images are acquired. Future improvements would be to use a radiopaque ruler placed on the patient during CkV imaging — this could eliminate the need for anatomy based image scaling. A lateral CkV-image should also be added to the implantation procedure CkV-image acquisition. The additional patient anatomy information would then enable a full 3-D verification of the GFM positions.

## 5 | CONCLUSIONS

To confirm GFM identification in MRI-images, performed in an MRI-only prostate radiotherapy workflow, a C-arm X-ray image acquired

from the GFM implantation procedure could be used. GFM migration is present but does not constitute a problem for the proposed method. The method can therefore be considered suitable for the task.

## ACKNOWLEDGMENTS

This work was supported by Gentle Radiotherapy (2016-03847 and 2016-02529) the Swedish Agency for Innovation Systems (VINNOVA), by "Allmänna sjukhusets i Malmö Stiftelse för bekämpande av cancer", SUS foundations, Region Skåne, and by "Onkologiska kliniken Stiftelse för bekämpande av cancer". The authors would like to acknowledge the valuable scientific input given by Jonas Scherman, PhD.

## CONFLICTS OF INTEREST

The authors declare no conflict of interest.

## REFERENCES

- Tyagi N, Fontenla S, Zelefsky M, et al. Clinical workflow for MR-only simulation and planning in prostate. *Radiat Oncol*. 2017;12:119.
- Tenhunen M, Korhonen J, Kapanen M, et al. MRI-only based radiation therapy of prostate cancer: workflow and early clinical experience. *Acta Oncol*. 2018;57:902–907.
- Roberson PL, McLaughlin PW, Narayana V, Troyer S, Hixson GV, Kessler ML. Use and uncertainties of mutual information for computed tomography/magnetic resonance (CT/MR) registration post permanent implant of the prostate. *Med Phys*. 2005;32:473–482.
- Nyholm T, Nyberg M, Karlsson MG, Karlsson M. Systematisation of spatial uncertainties for comparison between a MR and a CT-based radiotherapy workflow for prostate treatments. *Radiat Oncol*. 2009;4:54.
- Köhler M, Vaara T, Van Grootel M, Hoogeven R, Kempainen R, Renisch S. *MR-Only Simulation for Radiotherapy Planning Treatment Planning*. White paper: Philips MRCAT for prostate dose calculations using only MRI data; 2015:1–16. www.philips.se.
- Siverson C, Nordstrom F, Nilsson T, et al. Technical Note: MRI only prostate radiotherapy planning using the statistical decomposition algorithm. *Med Phys*. 2015;42:6090–6097.
- Persson E, Gustafsson C, Nordstrom F, et al. MR-OPERA: a multicenter/multivendor validation of magnetic resonance imaging-only prostate treatment planning using synthetic computed tomography images. *Int J Radiat Oncol Biol Phys*. 2017;99:692–700.
- Tyagi N, Fontenla S, Zhang J, et al. Dosimetric and workflow evaluation of first commercial synthetic CT software for clinical use in pelvis. *Phys Med Biol*. 2017;62:2961–2975.
- Edmund JM, Nyholm T. A review of substitute CT generation for MRI-only radiation therapy. *Radiat Oncol*. 2017;12:28.
- Kassim I, Joosten H, Barnhoorn JC, Heijnen BJ, Dirckx ML. Implications of artefacts reduction in the planning CT originating from implanted fiducial markers. *Med Dosim*. 2011;36:119–125.
- Gustafsson C, Korhonen J, Persson E, Gunnlaugsson A, Nyholm T, Olsson LE. Registration free automatic identification of gold fiducial markers in MRI target delineation images for prostate radiotherapy. *Med Phys*. 2017;44:5563–5574.
- Kapanen M, Collan J, Beule A, Seppala T, Saarihahti K, Tenhunen M. Commissioning of MRI-only based treatment planning procedure for external beam radiotherapy of prostate. *Magn Reson Med*. 2013;70:127–135.
- Dinis Fernandes C, Dinh CV, Steggerda MJ, et al. Prostate fiducial marker detection with the use of multi-parametric magnetic resonance imaging. *Phys Imaging Radiat Oncol*. 2017;1:14–20.
- Ghose S, Mitra J, Rivest-Henault D, et al. MRI-alone radiation therapy planning for prostate cancer: automatic fiducial marker detection. *Med Phys*. 2016;43:2218.
- Maspero M, van den Berg CAT, Zijlstra F, et al. Evaluation of an automatic MR-based gold fiducial marker localisation method for MR-only prostate radiotherapy. *Phys Med Biol*. 2017;62:7981–8002.
- Schenck JF. The role of magnetic susceptibility in magnetic resonance imaging: MRI magnetic compatibility of the first and second kinds. *Med Phys*. 1996;23:815–850.
- Port JD, Pomper MG. Quantification and minimization of magnetic susceptibility artifacts on GRE images. *J Comput Assist Tomogr*. 2000;24:958–964.
- Jonsson JH, Garpebring A, Karlsson MG, Nyholm T. Internal fiducial markers and susceptibility effects in MRI-simulation and measurement of spatial accuracy. *Int J Radiat Oncol Biol Phys*. 2012;82:1612–1618.
- Maspero M, Seevinck PR, Willems NJW, et al. Evaluation of gold fiducial marker manual localisation for magnetic resonance-only prostate radiotherapy. *Radiat Oncol*. 2018;13:105.
- Ng M, Brown E, Williams A, Chao M, Lawrentschuk N, Chee R. Fiducial markers and spacers in prostate radiotherapy: current applications. *BJU Int*. 2014;113(Suppl 2):13–20.
- O'Neill AG, Jain S, Hounsell AR, O'Sullivan JM. Fiducial marker guided prostate radiotherapy: a review. *Br J Radiol*. 2016;89:20160296.
- Gustafsson C, Nordstrom F, Persson E, Brynolfsson J, Olsson LE. Assessment of dosimetric impact of system specific geometric distortion in an MRI only based radiotherapy workflow for prostate. *Phys Med Biol*. 2017;62:2976–2989.
- Persson E, Gustafsson C, Nordstrom F, et al. MR-OPERA: a multicenter/multivendor validation of magnetic resonance imaging-only prostate treatment planning using synthetic computed tomography images. *Int J Radiat Oncol Biol Phys*. 2017;99:692–700.
- Pratt WK. *Digital Image Processing*, 3rd ed., New York, NY: John Wiley & Sons, Inc.; 2001.
- Otsu N. A threshold selection method from gray-level histograms. *IEEE Trans Syst Man Cybern*. 1979;9:62–66.
- Besl PJ, McKay ND. A method for registration of 3-D shapes. *IEEE Trans Pattern Anal Mach Intell*. 1992;14:239–256.
- Mann HB, Whitney DR. On a test of whether one of two random variables is stochastically larger than the other. *Ann Math Stat*. 1947;18:50–60.
- Kumar KA, Wu T, Tonlaar N, Stepaniak C, Yenice KM, Liauw SL. Image-guided radiation therapy for prostate cancer: A computed tomography-based assessment of fiducial marker migration between placement and 7 days. *Pract Radiat Oncol*. 2015;5:241–247.
- Moman MR, van der Heide UA, Kotte AN, et al. Long-term experience with transrectal and transperineal implantations of fiducial gold markers in the prostate for position verification in external beam radiotherapy; feasibility, toxicity and quality of life. *Radiother Oncol*. 2010;96:38–42.







# MRI-Only Radiotherapy of Prostate Cancer

## DEVELOPMENT AND EVALUATION OF METHODS TO ASSESS FIDUCIAL MARKER DETECTION, GEOMETRIC ACCURACY AND DOSIMETRIC INTEGRITY

In a workflow for prostate radiotherapy, based solely on MRI images, there is no need for CT imaging or CT/MRI image registration. MRI data can be converted into synthetic CT images required for absorbed dose calculations. This is referred to as an MRI-only radiotherapy workflow.

In the research described in this thesis, potential problems resulting from synthetic CT generation and geometric distortion in MRI images were investigated and solved. Geometric distortion was found not to constitute a problem. Synthetic CT generation using commercial software was found to be robust in a variety of clinical settings. Accurate and reliable procedures for the detection and verification of gold fiducial markers in an MRI-only radiotherapy workflow were also developed and evaluated. The fiducials could be detected with a degree of certainty not previously achieved, and could easily be verified using an MRI-independent method.

The methods presented here can facilitate a clinically feasible and safe implementation of an MRI-only prostate radiotherapy workflow.

Christian Jamtheim Gustafsson was awarded an M.Sc. in Medical Physics in 2010, and is a licensed medical physicist. He has since then been working on the application of MRI and the implementation of MRI into the radiotherapy workflow at several teaching hospitals.

